Transition Region Blinkers

Danielle Bewsher

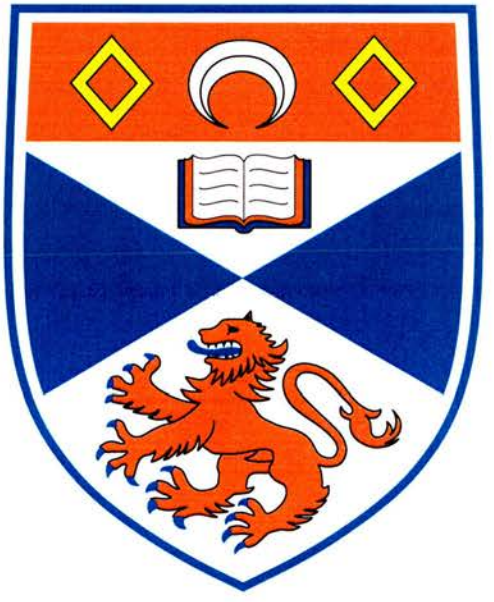

Thesis submitted for the degree of Doctor of Philosophy of the University of St Andrews

Abstract

Blinkers are small intensity enhancements seen in the transition region of the solar atmosphere. They are important because they give us a unique insight into the transition region which until recently, has not been studied in much detail. An automated method of identifying blinkers is presented and used to identify blinkers in the quiet Sun and active regions from SOHO/CDS O V data. The general properties of the blinkers are discussed. They have typical areas of 3×10^7 km^2 and lifetimes of 16 minutes. Their typical global frequency and intensity enhancement factors in the quiet Sun are 7 s^{-1} and 1.8, respectively, whereas these values increase in active regions to 13 s^{-1} and 2.4. Blinkers are best seen in the O V (629Å) transition-region line, but they also have strong signatures in O IV (554Å), and the chromospheric line, He I (584Å). The strongest O V blinkers can also be identified in O III (599Å). No significant signatures are found in the coronal lines Mg IX (368Å) and Mg X (624Å) for quiet Sun blinkers, but some increases can be seen in active-region blinkers. The ratios of the oxygen lines in blinkers were found to be flat confirming the result that blinkers are not temperature events, but are either density enhancements or increases in filling factor. Blinkers appear to occur preferentially over regions of enhanced chromospheric, transition region or coronal emission such as network boundaries.

The plasma velocities of the O V blinkers and the chromosphere below have been studied. The Doppler and non-thermal velocities found are preferentially more red-shifted and greater than the normal chromospheric and transition region plasma, respectively. The ranges of these enhanced velocities, however, are no larger than the typical spread of Doppler and non-thermal velocities in these regions.

Analysis of the magnetic field below blinkers shows that blinkers preferentially occur above regions of large or strong magnetic fragments with 55% of quiet Sun and 50% of active-region blinkers occurring in regions where one polarity dominates. Active-region blinkers are found above both active-region (plage) magnetic fields, as well as above the umbra and penumbra of sunspots. There appears to be no correlation between the strength of these single polarity magnetic fields or the ratio of mixed magnetic fields beneath blinkers and blinker characteristics.

Furthermore, following a comparison of explosive events and blinkers, only one case is found where the two phenomena are coincident. Initial probability analysis suggests that the hypothesis that explosive events occur independently of blinkers cannot be ruled out.

Declaration

(i) I, Danielle Bewsher, hereby certify that this thesis, which is approximately 37 500 words in length, has been written by me, that it is the record of work carried out by me and that it has not been submitted in any previous application for a higher degree.

date 27/9/02 ..... signature of candidate .....

(ii) I was admitted as a research student in September 1999 and as a candidate for the degree of PhD in September 2000; the higher study for which this is a record was carried out in the University of St Andrews between 1999 and 2002.

date 27/9/02 ..... signature of candidate ...

(iii) I hereby certify that the candidate has fulfilled the conditions of the Resolution and Regulations appropriate for the degree of PhD in the University of St Andrews and that the candidate is qualified to submit this thesis in application for that degree.

date 27/9/02 ..... signature of supervisor .....

(iv) In submitting this thesis to the University of St Andrews I understand that I am giving permission for it to be made available for use in accordance with the regulations of the University Library for the time being in force, subject to any copyright vested in the work not being affected thereby. I also understand that the title and abstract will be published, and that a copy of the work may be made and supplied to any bona fide library or research worker.

date 27/9/02 ..... signature of candidate

Acknowledgements

I would like to thank the following:

my supervisors, Clare Parnell and Alan Hood, for their encouragement and patience,

the 'Rutherford boys', especially Richard Harrison and Dave Pike, for supplying me with CDS data, answering all my questions and allowing me to push CDS to its limit continuously,

Davina Innes, for supplying me with the SUMER data used in this thesis, and for her patience,

Daniel Brown, for cheering me up when the Sun is not shining, and for all his technical/emotional and every other type of support,

Keith Bennett, for his ('geeky') computing support,

the Particle Physics and Astronomy Research Council for financial support,

and finally, my family and friends for their encouragement, faith that everything will be okay in the end and when all else fails, coffee and cake!

Here comes the Sun.

Here comes the Sun and I say

Its alright.

Little darling, its been a long, cold, lonely winter.

Little darling it feels like years since its been here.

Here comes the Sun. Here comes the Sun and I say

Its alright.

Little darling, the smiles returning to their faces.

Little darling it seems like years since its been here.

Here comes the Sun. Here comes the Sun and I say

Its alright.

Sun, Sun, Sun, here it comes.

Sun, Sun, Sun, here it comes.

Sun, Sun, Sun, here it comes.

Sun, Sun, Sun, here it comes.

Sun, Sun, Sun, here it comes.

Little darling, I feel that ice is slowly melting.

Little darling it seems like years since its been clear.

Here comes the Sun. Here comes the Sun and I say

Its alright.

Here comes the Sun

Here comes the Sun

Its alright

Its alright.

George Harrison

Contents

Chapter 1

Introduction

1.1 The Sun

The Sun is a typical G2 V star, but its proximity to Earth makes it unique and of great interest. It is a massive ball of plasma that is 4.5×10^9 years old, has a mass of 1.99×10^{30} kg and a radius of 6.96×10^5 km. It consists of approximately 90% hydrogen, $\leq$ 10% helium and 0.1% other elements.

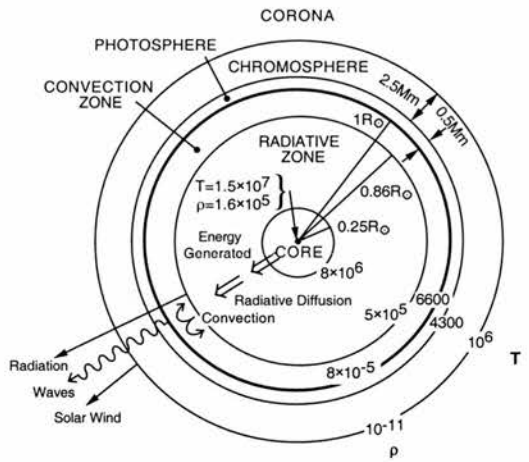

Figure 1.1: The structure of the Sun. New research suggests that the convection zone starts at 0.7 $R_\odot$.

The interior of the Sun consists of a core, a radiative zone and a convection zone. The pressure (1.6×10^5 kg m^{-3}) in the core drives thermonuclear fusion resulting in a super hot (1.5×10^7 K)

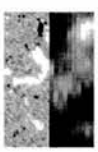

plasma where hydrogen is fusing to form helium with energy released as photons and neutrinos.

Energy escapes through radiation, the most efficient process at the local densities and pressures, i.e a radiation zone exists. Because it is so hot, the atoms are totally stripped of electrons and exist as ions. The radiation zone is a place where the photons (packets) of energy are absorbed and re-emitted many times and energy transfer through this region can take up to 170 000 years, but it is still the most efficient energy transport process. The temperature and density of the interior decreases through the radiation zone and there is a place where ions begin to recombine with electrons. This produces a barrier to radiation and from this point, convection becomes more efficient, i.e. a convection zone exists. Energy wells up to the surface in huge convection cells with length scales of the order of $1-2''$ (700 - 1 450 km) and $18-25''$ (13 000 - 18 000 km).

Since we have plasma motion in the body of the Sun, magnetic fields are induced which rise to the solar surface due to magnetic buoyancy. As the density and temperature falls within the outer layers of the solar interior, a level is reached where radiation can dominate again from a region with a very narrow optical depth, the photosphere, the visible surface of the Sun. It is a sharply defined layer of the Sun, but one which produces most of the visible radiation that we receive. The magnetic field emerges through the photosphere into the atmosphere where it is responsible for most solar complexities and activity.

One might expect the density and the temperature to continue to decrease with altitude above the photosphere, defining a well behaved solar atmosphere. It does this initially in a region called the chromosphere, but the atmosphere is not as one would expect. Somehow energy is dumped into the upper atmosphere resulting in a region we call the corona, which is two orders of magnitude hotter than the photosphere. Between the chromosphere and corona there is a thin layer we call the transition region in which there is a step rise in temperature.

In the atmosphere, the magnetic field is described as being 'frozen in' to the plasma. This occurs when the convective motions of the plasma dominate the diffusion of the magnetic field.

In this thesis, we investigate the solar atmosphere, and hence we discuss the different layers in further detail. Before we can describe the observations of these regions, however, we must describe how we observe the Sun. As already mentioned, the majority of the Sun's visible radiation is emitted by the photosphere, but the chromosphere, transition region and corona all emit radiation at a variety of wavelengths from the radio through to X-rays. In this thesis, we observe

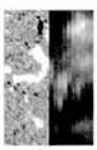

the Sun's atmosphere by looking at emission lines of atoms that are emitted at wavelengths and temperatures that are characteristic of the Sun's atmosphere.

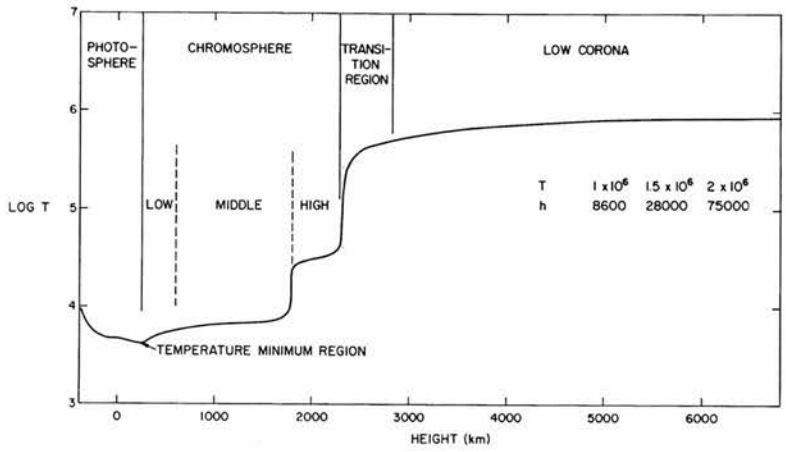

Figure 1.2: Variation of temperature with height in a simple 1D solar atmosphere (Athay, 1976)

1.1.1 Photosphere

The photosphere is the visible surface of the Sun and has a temperature of 6 600 K. Turbulent motions in the convection zone below give rise to many of the photosphere's observable features such as granulation and supergranulation.

Granules are the observable top of small convective cells, cover the whole of the Sun's surface and there are approximately a million present at any one time on the solar surface (Priest, 1982). The centre of the granules appear brighter, since they are the hotter, rising material and the boundary of the granules appear darker as they are comprised of the cooler, draining material. The typical diameter of these cells lies in the range $1'' - 2''$ (700 - 1 400 km) with a distance of approximately $2.5''$ (1 800 km) between cell centres. The lifetime of granules can be up to 15 minutes but on average they last approximately 8 minutes.

In addition there is also supergranulation, which comprises the tops of much larger convection cells. The material in these cells rises with a velocity of 0.1 km s^{-1}, moves horizontally with a velocity of 0.3 - 0.4 km s^{-1} and then falls with a velocity of 0.1 - 0.2 km s^{-1} (Priest, 1982). Supergranules are irregular in shape, but they have diameters that range from 13 000 to 18 000 km ($18''$ to $25''$; Hagenaar, 2001). Supergranules can last for 1 - 2 days. The boundaries of these supergranule cells are very prominent in the chromosphere and make up the so-called network.

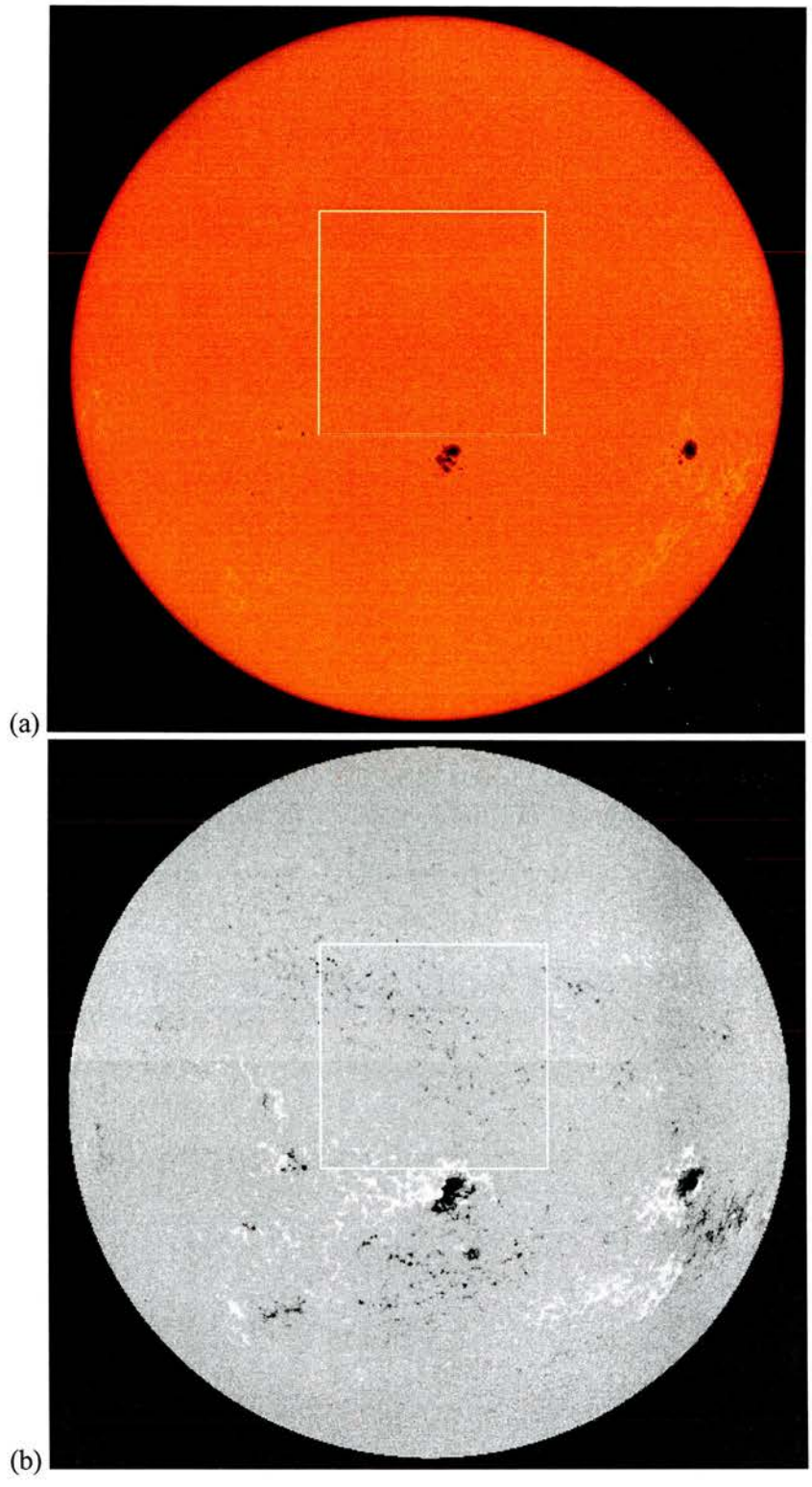

Figure 1.3: The Sun seen in (a) white light and (b) a photospheric magnetogram. The white boxes indicate the MDI high resolution field of view. Images courtesy of SOHO/MDI.

Figures 1.3, 1.4 and 1.5 show images of the different atmospheric layers of the Sun taken on the same day and many features can be seen throughout the solar atmosphere. Figure 1.3 (a) shows a white light image of the photosphere. The positions of strong concentrations of magnetic field, sunspots, can be clearly seen as dark spots in the centre and to the right of the image. Figure 1.3 (b) shows a photospheric magnetogram, where the black and white areas are negative and positive polarity magnetic field, respectively. Both positive and negative polarity field can be seen within one sunspot region eventhough these sunspots have negative polarity. Active regions, which are described later in Section 1.1.6, have been traditionally thought of as regions of complex magnetic field and are clearly visible as the areas with large concentrations of magnetic field in the centre and to the right of the image, where both sunspots and the surrounding plage (bright enhanced emission) are observed. Outside of the active regions, the quiet Sun, discussed later in Section 1.1.5, is a region that is less magnetically complex and is observed as the small speckled concentrations of opposite magnetic polarity as seen inside the white box in Figure 1.3 (b).

1.1.2 Chromosphere

Immediately above the photosphere lies the chromosphere. The temperature drops to a minimum value of 4 400 K and then rises slowly to a temperature of 10 000 K at the top of the chromosphere. It is about 10 000 km thick and highly non-uniform due to the presence of the magnetic field (Priest, 1982).

Hα emission, Figure 1.4 (a), is radiated at chromospheric temperatures and reveals the structure of the chromosphere. The sunspots can be seen as the dark spots and the bright region surrounding the sunspots is called plage. Filaments are long dark absorption features observed on the disk, which are called prominences when observed on the limb as bright structures in chromospheric lines. These are cool (7 000 K), dense features where plasma at chromospheric temperatures is trapped in arcades of magnetic loops, that can last for many months. At the end of their lifetime they can erupt outwards from the Sun at hundreds of km s^{-1}. They always lie above a magnetic neutral line, that separates regions of opposite magnetic polarity in the photosphere beneath. An example of a filament can be seen as the dark structure at the top right corner of Figure 1.4 (a) and (b).

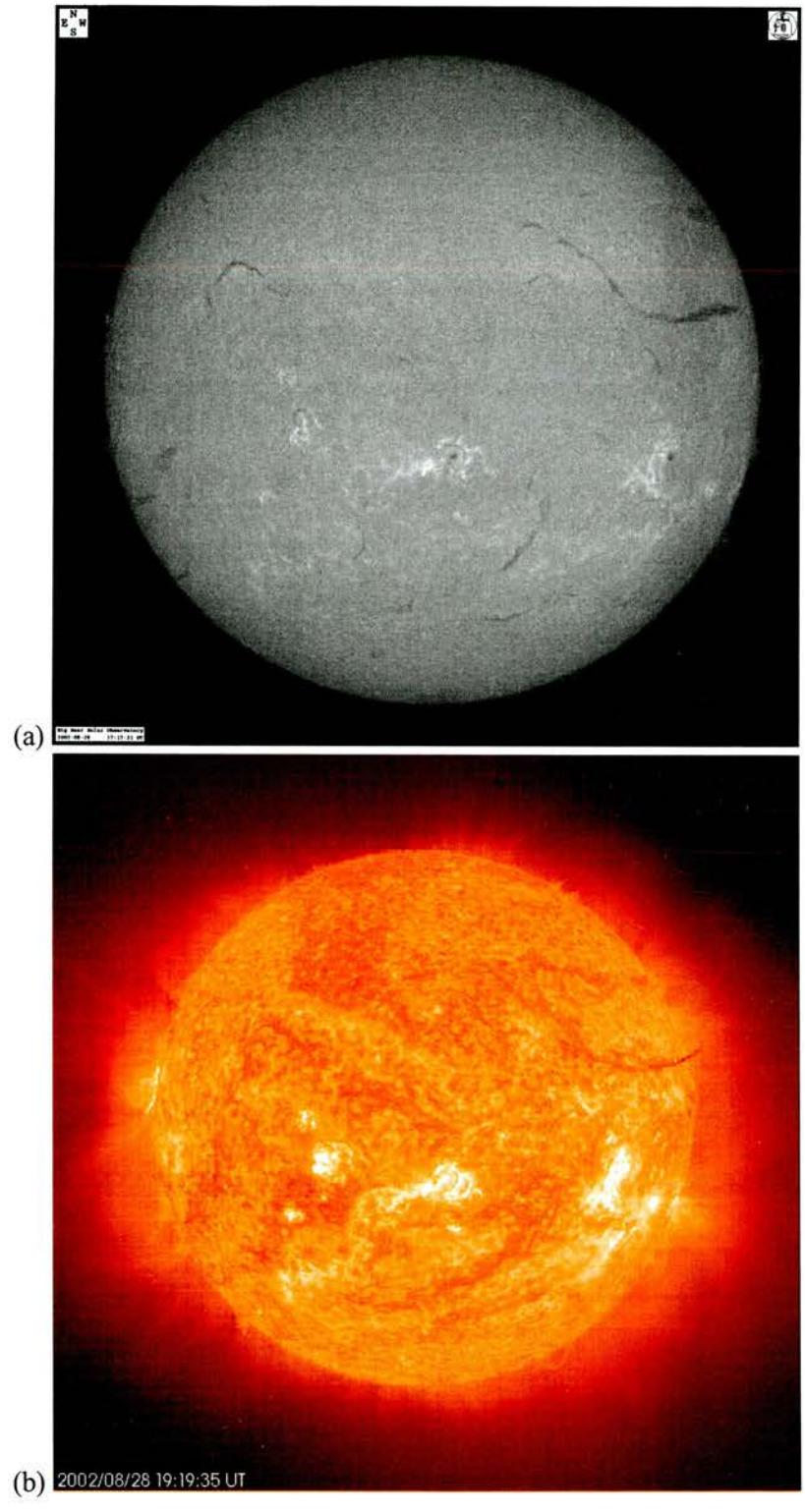

Figure 1.4: The chromosphere seen in (a) Hα and (b) in the He II emission line formed at a temperature of 8×10^4 K. Images courtesy of Big Bear Observatory and SOHO/EIT.

The network of supergranule cells caused by convective motions below the photosphere can also be seen in the chromosphere. The ultraviolet image in Figure 1.4 (b) clearly shows the bright centre and dark boundaries of the supergranule cells which give the speckled appearance in this Figure. At the limb of the Sun, small finger-like structures can be seen, these are spicules and we will discuss them later in Section 1.4.3 The physical characteristics and velocity of the plasma in the chromosphere will be discussed throughout this thesis.

1.1.3 Transition region

A sharp rise in temperature occurs between the chromosphere and the corona. The thin layer where this large temperature gradient is located is called the transition region. The thickness of the transition region is estimated to be 30 km between the temperature of 3×10^4 to 3×10^5 K and 2 500 km between 2×10^5 and 10^6 K. There are many small-scale phenomena, including blinkers, the topic of this thesis, that have been identified in the transition region. In Section 1.3 and 1.4 we discuss blinkers and other transition region phenomena including explosive events, active transition-region brightenings, SUMER unit brightenings and UV bursts. All of these phenomena are observed in the extreme ultraviolet (EUV) wavelengths of the transition region. Little is known about the structure and dynamics of this region and research in this area is essential if we are to understand the coupling of the whole of the solar atmosphere. We will discuss the properties of the transition region and blinkers throughout this thesis.

1.1.4 Corona

The corona is the outermost and hottest (1 - 10 million K) part of the solar atmosphere. The high temperature of the corona is still a mystery over 100 years after its discovery (see Phillips, 1992, for a discussion). Figure 1.5 shows two UV images of the corona. The brightest regions are active regions with their complex magnetic loop structures, and the darkest regions are called coronal holes. Outside of these regions is the quiet Sun. We will discuss both the quiet Sun and active regions in Sections 1.1.5 and 1.1.6, respectively.

White-light coronal radiation is caused by the scattering of photospheric light off particles (K-corona) and dust (F-corona). The corona is observed in the full range of wavelengths from the visible through the ultra violet and into X-rays (Phillips, 1992). From the Earth, the corona

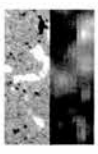

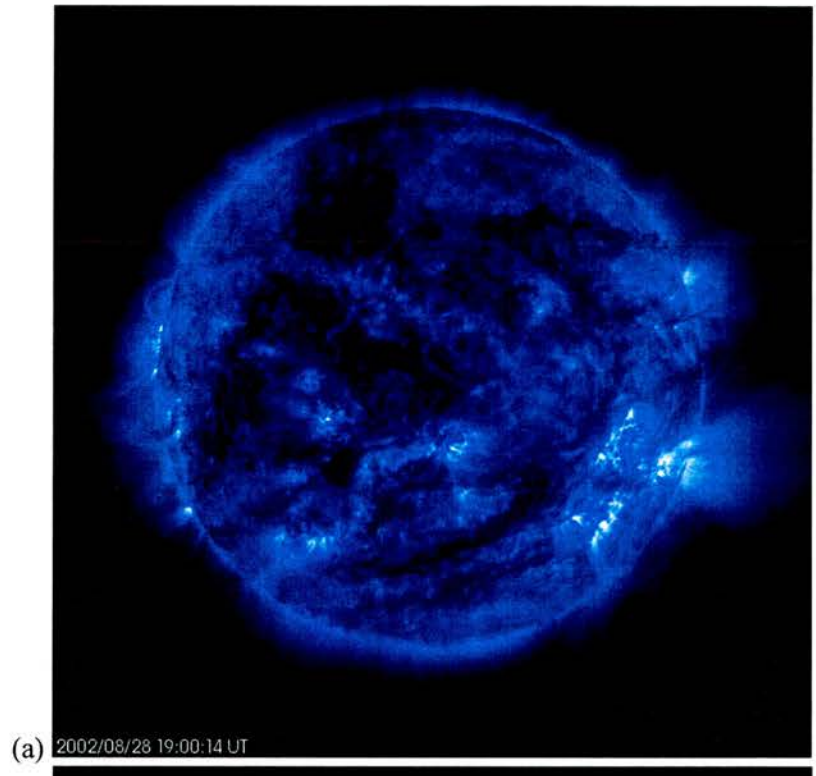

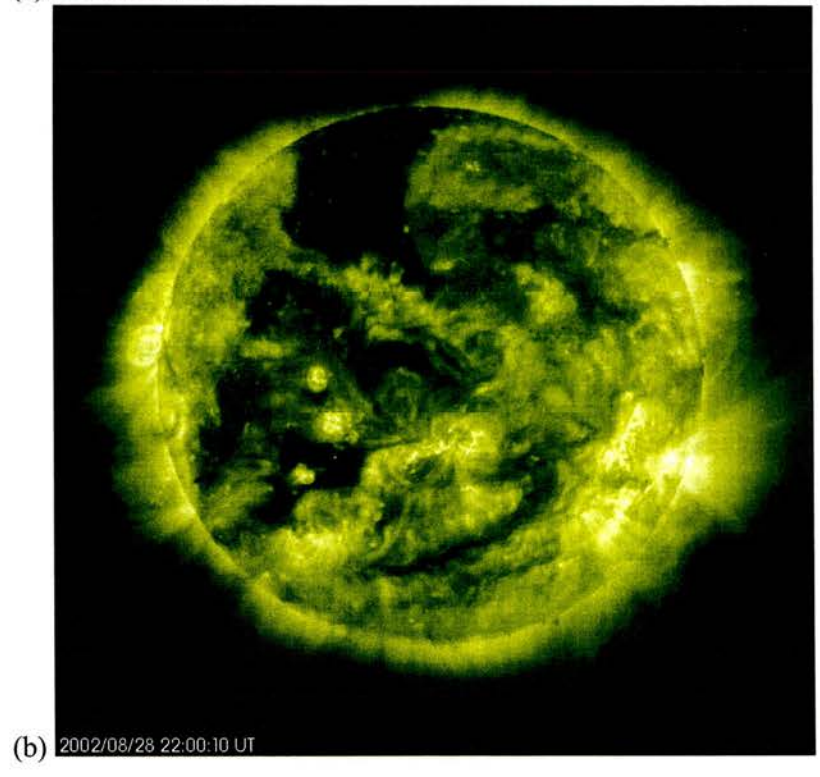

Figure 1.5: The corona seen with (a) the Fe IX - X and (b) the Fe XII lines formed at a temperature of 1.3×10^6 K and 1.6×10^6 K , respectively. Images courtesy of SOHO/EIT.

can be observed during eclipses as a faint halo around the Sun. The extent of the visible corona varies with the solar cycle. This is the variation of the number of sunspots on the Sun, and it follows an approximate 11 year cycle. At solar maximum, when there are the most sunspots, the corona extends out in all directions. At solar minimum, however, the corona extends mainly in the equatorial regions.

Throughout this thesis, we will be discussing small-scale events (Sections 1.3 and 1.4). The Sun also has large-scale activity, the largest of which are flares and coronal mass ejections (CME's). Flares are large, highly dynamic and energetic events which can be observed in a range of wavelengths from microwaves, through the ultraviolet spectrum to X-rays. A flare is an explosion, where energy is dumped into the atmosphere after the stressed magnetic field releases its energy.

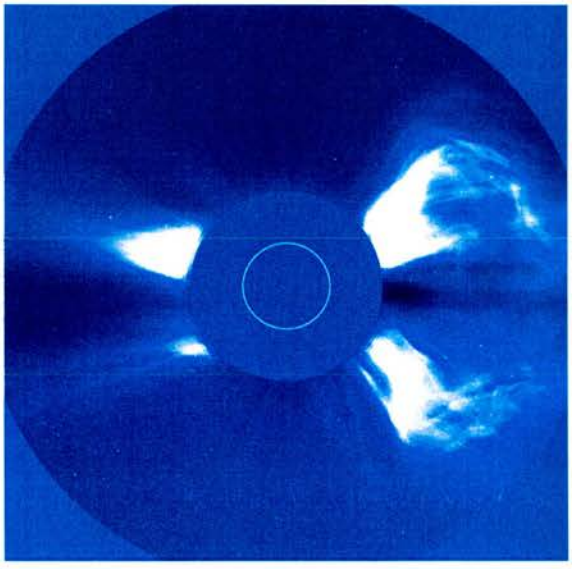

Figure 1.6: Large coronal mass ejection, the white circle represents the solar surface. Image courtesy of SOHO/LASCO.

As described previously, prominences can erupt from the solar surface. These eruptions can lead to a CME, when approximately 10^{13} kg of plasma are expelled from the Sun within a few hours at a velocity that ranges from 10 - 1 000 km s^{-1}. Figure 1.6 shows a large coronal mass ejection with plasma ballooning out to the right of the Sun. The rates of occurrence of both flares and CME's vary with the solar cycle, at solar maximum the rate of occurrence is highest and at solar minimum it is lowest.

1.1.5 Quiet Sun

Traditionally, the quiet Sun has been thought of as the most 'basic' region of the Sun, but the quiet Sun is far from quiet and is highly dynamic. The quiet Sun, as seen from photospheric magnetograms, is speckled with both positive and negative polarity field which tends to be concentrated around the edges of supergranule cells. These magnetic fields can be divided into three groups, intranetwork, network fields and ephemeral regions (Priest, 1982). Intranetwork fields are bipoles and exist in the centres of supergranule cells where there are upflows. They are swept to the supergranule boundaries by the convective motions below, where they interact with network fields, which exist around the boundaries and are trapped in the downflow regions. These network fields are made up of intranetwork fields and also decayed ephemeral and active regions. We discuss ephemeral regions in Section 1.4.1. There are many phenomena, including blinkers, that occur in the quiet Sun above the photosphere. Many of these are described and discussed in Sections 1.3 and 1.4.

1.1.6 Active regions

Active regions have enhanced emission over a broad spectral range and have distinctive appearances in the photosphere, chromosphere, transition region and corona. Compared to the quiet Sun, active regions are more active on larger spatial scales and contain more complex magnetic field.

As mentioned previously, active regions can consist of plage and sunspots. Sunspots are cooler (3 700 K as opposed to 6 600 K in the photosphere) than their surroundings and are regions of exceptionally strong and concentrated magnetic field. Most sunspots have a lifetime of a few days, but some can last for a few months. The central part of the sunspot is called the umbra and has a typically diameter of 10 000 - 20 000 km. Inside the umbra, the temperature (about 4 000 K) and magnetic field strength (the order of a few thousand Gauss), is fairly uniform with the magnetic field being nearly vertical.

Umbral dots, patches of brightness within an umbra, can be observed. They have diameters of 100 - 200 km, lifetimes of 25 minutes and temperatures of approximately 5 000 K (Priest, 1982). The magnetic field within umbral dots is the same as that in the surrounding umbra. Towards the edge of the umbra, the magnetic field strength decreases, and in the surrounding penumbra, the

magnetic field strength is typically 1 000 Gauss. The penumbra consists of light and dark radial filaments, which are 95% and 60% of the intensity of the surrounding photosphere, respectively.

A large sunspot, can have a light-bridge, that is a ridge of bright material that crosses the umbra. They can sometimes be associated with the division of a large sunspot.

Plage is the part of the active region outside sunspots and has a mean magnetic field strength of a few hundred Gauss.

1.2 Solar and Heliospheric Observatory (SOHO)

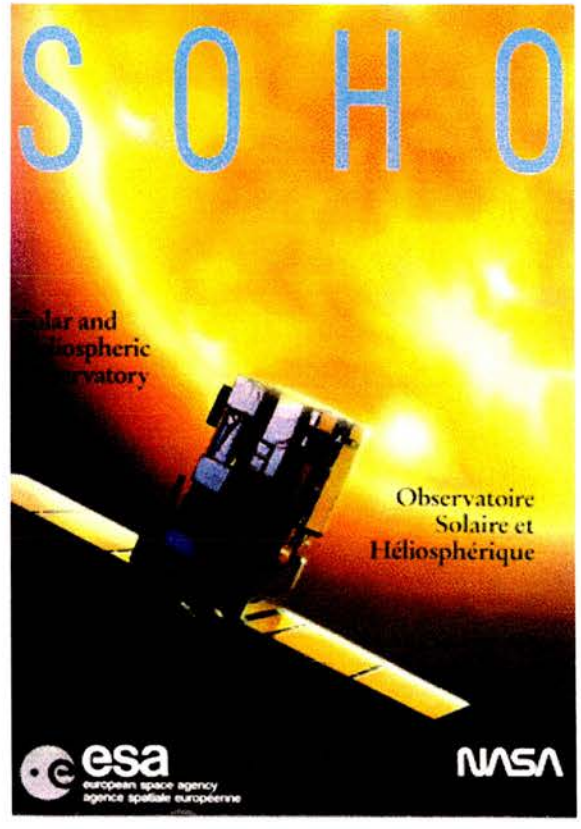

Figure 1.7: Artists impression of SOHO in orbit around the Sun. Courtesy of SOHO

In this thesis, we use data from the Solar and Heliospheric Observatory (SOHO). SOHO is a joint mission run by the European Space Agency (ESA) and the National Aeronautics and Space Administration (NASA). It observes the Sun continuously from a 180-day period halo orbit about the Sun-Earth L1 Lagrangian point, which is about 1.5×10^6 km sunward of the Earth

and is the location where the gravitational pull and centrifugal force of the Earth and the Sun form a balance. Its three main objectives are (i) to study the solar interior using helioseismology, (ii) study the heating mechanisms of the solar corona and (iii) investigate the solar wind and its acceleration processes (Domingo et al., 1995). SOHO was launched from an Atlas II-AS rocket on 2nd December 1995 and operations started during April 1996.

There are twelve instruments on board SOHO. GOLF (Global Oscillations at Low Frequencies), VIRGO (Variability of solar IRradiance and Gravity Oscillations) and MDI (Michelson Doppler Imager) study helioseismology (MDI also produces magnetograms). They study the vibrations of the Sun's surface and infer the structure of the Sun from these measurements. COSTEP (COmprehensive SupraThermal and Energetic Particle analyser), CELIAS (Charge, Element and Isotope Analysis System) and ERNE (Energetic and Relativistic Nuclei and Electron experiment) study the solar wind by insitu particle measurements and sampling. SWAN (Solar Wind ANisotropies) also studies the solar wind, but is a wide angle imager of the heliosphere. EIT (Extreme ultra-violet Imaging Telescope), UVCS (Ultra-Violet Coronagraph and Spectrometer), LASCO (white Light And Spectrometric COronagraph), SUMER (Solar Ultraviolet Measurement of Emitted Radiation) and CDS (Coronal Diagnostic Spectrometer) all study the solar atmosphere by remote sensing. In this thesis, we use data from CDS, MDI and SUMER only.

1.2.1 Coronal Diagnostic Spectrometer (CDS)

CDS focuses on two of SOHO's objectives, namely, how the corona is heated and how the solar wind is accelerated. Critical to answering these questions is the determination of plasma characteristics e.g. velocity, temperature, density and abundances. CDS is designed to determine such information through the study of emission lines in the extreme ultraviolet (EUV) wavelengths (Harrison et al., 1995).

Figure 1.8 shows the optical layout of the CDS instrument. It consists of a Wolter II grazing incidence telescope which simultaneously feeds a normal incidence spectrometer (NIS) and a grazing incidence spectrometer (GIS) which share a common slit. The telescope beam is split in to two portions, one for each spectrometer. The GIS portion of the beam hits a grating in grazing incidence and the spectrum is dispersed on to four 1-D detectors placed around a Rowland circle

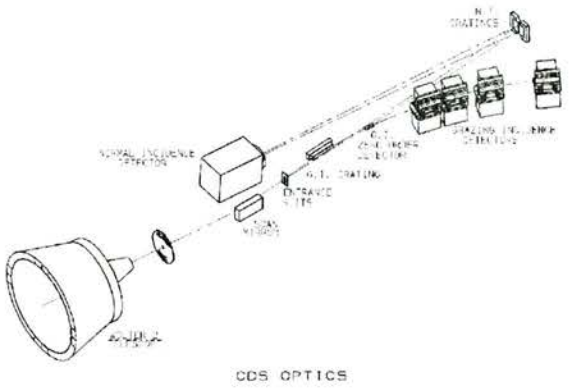

Figure 1.8: CDS optical layout. Courtesy of SOHO/CDS.

where the focus is located. The NIS portion of the beam is fed through a twin grating in normal incidence and the resulting spectrum is viewed by a 2-D detector system.

The GIS is a spherical grating and hence the system is astigmatic, i.e there is no spatial focus, images are built up by rastering in two directions. Rastering is performed by rotating the scan mirror and by scanning the slit. The NIS gratings are torodial, resulting in a stigmatic system. Images of the slit are dispersed on the NIS detector producing an image focused on the detector. Rastered images are created by rotating the scan mirror. Since the NIS spectrum is dispersed by two gratings, two spectral ranges are viewed by the one 2-D detector. Because of the nature of the observations that we want to analyse in this thesis, we use NIS data only. Figure 1.9 shows an example of the two NIS spectra. The first NIS spectrum, NIS1 has a wavelength range of 308-381 Å, and the second, NIS2 has a wavelength range of 513-633 Å. These ranges were selected to observe emission lines from particular ions within the solar atmosphere.

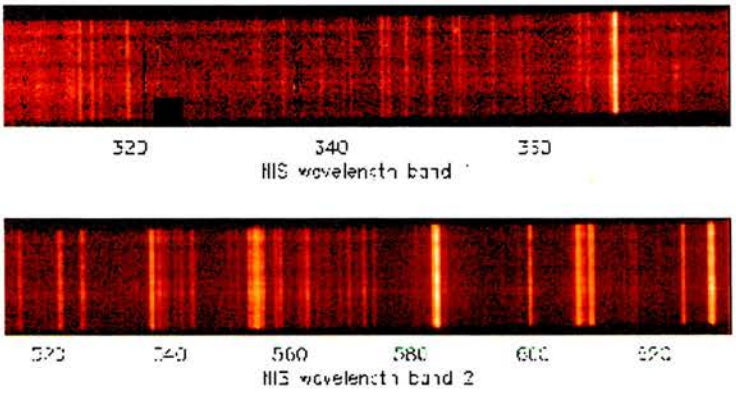

Figure 1.9: Quiet Sun spectra in the two NIS spectral bands. Courtesy of SOHO/CDS.

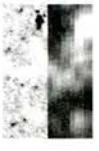

1.2.2 Michelson Doppler Imager (MDI)

MDI is part of the Solar Oscillations Investigation (SOI) which probes the interior of the Sun by measuring the photospheric manifestations of solar oscillations. In addition, it provides photospheric observations of the solar magnetic field and the surface motions of the magnetic field. In this thesis, we use only the photospheric magnetic field images that MDI produces. A line-of-sight magnetogram is constructed by measuring the Doppler shift of the Ni I 6 768 Å line in both right and left polarised light. The difference between these two is a measure of the Zeeman splitting and is roughly proportional to the magnetic flux density, which is the line-of-sight component of the magnetic field averaged over the resolution element (Scherrer et al., 1995).

1.2.3 Solar Ultraviolet Measurements of Emitted Radiation (SUMER)

The Solar Ultraviolet Measurements of Emitted Radiation (SUMER; Wilhelm et al., 1995) is designed to study both structures and dynamical processes occurring in the solar atmosphere. The temperature coverage of the instrument (10^4 to 2×10^6 K) allows investigation of the chromosphere, transition region and corona. Spectroscopic studies of plasma densities and temperatures provide an unique insight to many physical processes. These include flows and turbulence, both of which are associated with magnetic activity and atmospheric heating. SUMER measures EUV line profiles in the 500 - 1 610 Å wavelength range and determines Doppler shifts and line broadening with high accuracy and provides stigmatic images of the Sun. SUMER is a spectrometer and its optical layout is based upon two parabolic mirrors, a plane mirror and a spherical concave grating.

1.3 Blinkers

Transition region blinkers are small-scale bright intensity enhancements and were first observed by Harrison (1997) using CDS (Harrison et al., 1995) which is on-board the SOHO. They are most easily identified in the 629Å emission line from O V, but are also found in other extreme UV (EUV) lines emitted from O III (599Å), O IV (554Å), He I (584Å) and He II (304Å) (Harrison, 1997; Harrison et al., 1999; Berghmans et al., 1998). These lines are representative of plasma temperatures of 2.5 $\times 10^5$ K, 1.0 $\times 10^5$ K, 1.6 $\times 10^5$ K, 2.0 $\times 10^4$ K and 5.0 $\times 10^4$ K,

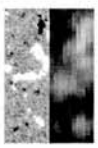

respectively. The properties of blinkers located in the quiet Sun were investigated by Harrison (1997) and Harrison et al. (1999) who found that they (i) typically last between 1 and 40 minutes (average 17 minutes), (ii) have areas between 2 - 5 $\times 10^7$ km^2 and (iii) have intensity enhancement factors of 1.5 for the O V and O IV lines and 1.3 for O III. Ratios of the O V, O IV and O III intensity light curves of blinkers were studied to determine whether blinkers are density enhancements or temperature dependent features. These ratios were found to be flat. Hence, blinker intensity enhancements were interpreted as being due to density or filling factor increases rather than a temperature increase. Harrison et al. (1999) studied just 97 events, which were identified by eye from movies and intensity profiles, and found the global birth rate of blinkers to be just 1.2 s^{-1}.

Blinkers have also been identified using He II images taken from EIT/SOHO (Berghmans et al., 1998). They found the variation in properties of the events was larger with lifetimes, areas and intensity enhancement factors found between $2 - 60$ minutes , $4 - 40 \times 10^7$ km^2 and $1.1 - 2.7$, respectively. They also found the global birth rate of He II blinkers to be between $0.3 - 20$ s^{-1} depending on the significance of the event peaks, although they suggest it might possibly be as high as 40 s^{-1}.

More recently, Brković et al. (2001) have analysed quiet-Sun network and intranetwork region movies taken by CDS in the He I, O V and Mg IX lines. From their results the typical area of a transition-region brightening is 2.4×10^7 km^2 and the typical lifetime is 16 minutes. Like Berghmans et al. (1998) they also find a larger global frequency of 22 s^{-1}.

Gallagher et al. (1999), using CDS, noted some evidence for periodic behaviour of transient brightenings in the quiet-Sun network. They concluded that these brightenings were produced by the rapid compression of the transition region plasma.

Blinkers have, until recently, been considered a quiet-Sun phenomena, however, there is evidence that blinkers occur in active regions too. Walsh et al. (1997) studied a set of high cadence (14 seconds) CDS data including the He I (584 Å) chromospheric line, the O V (629 Å) transition region line and the Mg IX (368 Å) and Fe XVI (360 Å) coronal lines. They identified two events that seemed to fit the description of a blinker, and, hence, named them 'active-region blinkers' (AR blinkers). These events showed signatures at all four wavelengths. They had length scales of 14 and 18 Mm, lifetimes of 10 and 16.5 minutes and intensity enhancements of 2.5 and 4. Due

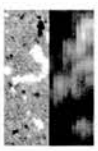

to the high cadence of their data, Walsh et al. (1997) were able to determine that the signatures in O V occurred before the start of the events in He I and the events in both Mg IX and Fe XVI. This result suggests that these events are neither heating nor cooling and is consistent with the findings for QS blinkers which are believed not to be temperature events. Doppler velocities of between 30 and 70 km s^{-1} were observed and a positive correlation between the line width and Doppler velocity were also found suggesting that they are not uni-directional. The location of the events above the magnetic field was discussed, with one event found above a region of positive magnetic field whilst the other appeared over negative magnetic field.

These observational results are highly suggestive that blinkers may also occur in active regions. Furthermore, there does not appear to be any physical reasons why blinkers could not occur there.

1.4 The solar zoo

There are lots of reports of different transient events observed in the solar atmosphere. Many are observed using different instruments and different observing techniques. Some may be the same phenomena seen in different ways. There is a need to determine which, if any, are the same and simplify the current complex zoo of phenomena. We will mention many of the phenomena throughout this thesis and compare them to blinkers and so we describe each of the events and their properties here.

1.4.1 Ephemeral regions

Ephemeral (short-lived) regions are small-scale bipolar regions of magnetic field that emerge all over the photosphere and have an average lifetime (time during which they can be identified as a bipolar structure) of 4.4 hrs (Harvey, 1993). Their lifetime is much less than that of an active region, which can last for several weeks. They emerge preferentially near the boundaries of supergranule cells (Wang, 1989; Harvey, 1993) and break up into smaller concentrations which are dispersed around the supergranule boundary. The flux in the ephemeral regions soon merges in with the network flux and can cancel with other opposite polarity network field (Harvey et al., 1999). The rate of emergence of ephemeral regions has recently been revised by Hagenaar (2001)

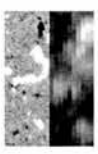

and is now about 8.4×10^{-24} cm^{-2} s^{-1} or in other words, just less than one per supergranule (radius: 7 000 km, geometry: hexagonal, area: $3\sqrt{3}r^2/2 \approx 1.3 \times 10^8$ km^2) per day.

1.4.2 Cancelling magnetic features

Cancelling magnetic features are also frequently seen at the edges of photospheric supergranule cells. These are concentrations of opposite polarity magnetic flux that occur in the magnetic carpet (small-scale magnetic fragments) which mutually lose flux or cancel. The rate of cancellation can be estimated from the recent magnetic carpet model by Parnell (2001) who found that around 3 to 5 times as many cancellation events occur as emergence events, hence, a reasonable estimate at the rate of cancellation is $3 - 5$ per supergranule per day.

1.4.3 Spicules

Spicules are ejections of plasma that can be observed on the limb of the Sun in chromospheric lines. These ejections of material have velocities of 20 - 30 km s^{-1} and can reach as high as 11 000 km before falling back down. Spicules have a lifetime of less than 15 minutes, a diameter of several hundred km to 1.5 Mm and a length of approximately 10 000 km. They have a temperature of between 1 and 2×10^4 K, but can also be seen in transition regions lines formed around 10^5 K. The birthrate of spicules is estimated to be 2×10^{-5} Mm^{-2} s^{-1} (Wilhelm, 2000).

1.4.4 Explosive events

There is no precise definition of an explosive event, but they are characterised by the large Doppler velocities that are associated with them. They were first observed using the High Resolution Telescope and Spectrograph by Brueckner and Bartoe (1983) as high energy turbulent events and jets. They have a typical size of $2'' - 4''$ and have an average lifetime of 60 seconds. Line profiles of explosive events show strong non-Gaussian enhancements of both wings of the profile and the velocities associated with them range from ± 50 to ± 250 km s^{-1}. Their strongest appearance is in transition regions lines formed around 10^5 K but they are also seen in the chromosphere (Madjarska and Doyle, 2002) and rarely in the corona (Dere, 1994). Explosive events have been observed in both quiet Sun, active regions and coronal holes. Recent studies have

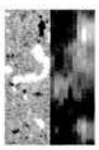

suggested that explosive events are found above complex weak magnetic fields or on the edge of unipolar fields (Porter and Dere, 1991). Magnetic reconnection has been suggested as a possible energy source for these events (Innes et al., 1997), but the location of the reconnection between the chromosphere and the corona is still not understood.

1.4.5 SUMER unit brightenings

Chae et al. (2000) observed many small-scale 'unit-brightening events' in the quiet-Sun transition region with SUMER data. They have a size of a few arcsecs and a lifetime of a few minutes and appear to have a blinker-like behaviour. They report that these events are unlike explosive events since their UV line profile is not as broad, but they do still have significantly enhanced wings.

Teriaca et al. (2001) also used SUMER to investigate the characteristics of such unit-brightening events in the quiet-Sun transition region. They found that unit-brightenings have a duration of just 200 s ($<$ 4 minutes), their line profile has a slight broadening and a 5 km s^{-1} blue shift. These events were also found to have no substantial variation in density about 10^{10} cm^{-3} in the O IV line. Hence, they suggest that an increase in filling factor is the most likely cause of the intensity enhancement.

1.4.6 Network and cell brightenings

Harra et al. (2000) used single slit CDS O V and He I data to identify network and cell brightenings. They found that network brightenings are larger than cell brightenings and have a mean duration of 150 seconds and an energy of $10^{26.9}$ ergs, whereas cell brightenings have a mean duration of 96 seconds and an energy of $10^{25.8}$ ergs. The size of the brightenings range from 1 to 5 CDS pixels and the occurrence of cell and network brightenings is approximately the same.

1.4.7 Active transition-region brightenings

Active transition-region brightenings were described by Mason et al. (1997) as events observed in the Mg V (353 Å) and Mg VI (349 Å) emission lines formed at the transition region temperatures 3×10^5 K and 4×10^5 K, respectively and showed no significant enhancement in the hotter

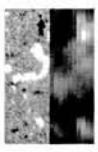

Mg IX and Mg X coronal lines.

Fludra et al. (1997) also observed bright compact sources in transition region lines using CDS. They found events with a lifetime of at least 12 hours near regions of strong magnetic flux, such as near a sunspot and overlying the penumbra or the umbra.

1.4.8 UV 'bursts'

Using the Harvard EUV Spectrometer on Skylab, Withbroe et al. (1985) report that frequent localized short-term fluctuations were observed in the chromosphere, transition region and the corona above active regions. Approximately 20% of the $5'' \times 5''$ pixels had intensity variations exceeding a factor of 1.3 for the H I Lα (1216 Å) which has a formation temperature of $\approx 2 \times 10^4$ K, a factor of 1.5 for the C III (977 Å), O IV (554 Å) and O VI (1032 Å) lines which are formed at mean temperatures of 10^5, 2×10^5 and 3×10^5 K and a factor of 1.4 for the Mg X (625 Å) line which is formed at about 2×10^6 K. The pixels on the Skylab Spectrograph are a factor 3.5 times larger than those on SOHO/CDS and the cadence of the data used by Withbroe et al. (1985) was just 5.5 minutes. They find, however, that significant variations in these EUV lines occur over temporal intervals of 5 to 15 minutes and with spatial scales of $5'' - 15''$. A number of other authors (cf. Lites and Hansen, 1977; Bruner and Lites, 1979; Athay et al., 1980; Dere et al., 1981; Athay, 1984; Porter et al., 1984; Habbal et al., 1985) report observations of UV 'bursts' or impulsive variations in emission from spectral lines formed in the lower transition region (T $\approx 10^5$ K) in active regions using data from OSO-8, HRTS and SMM and the Harvard Spectrograph on Skylab. The 'bursts' were found to be a common, nearly continuous phenomena, in active regions.

1.4.9 Nanoflares/microflares

Nanoflares (Parker, 1988) and microflares (Porter et al., 1987) are names given to localised impulsive heating events. These coronal events have energies that range between 10^{24} - 10^{27} ergs. They have lifetimes that vary from seconds to tens of minutes and even hours, and are preferentially located above the magnetic network in both the quiet Sun and active regions.

1.4.10 Active-region transient brightenings

Active-region transient brightenings (ARTBs) have been observed with Yohkoh/SXT and were first described by Shimizu et al. (1994). ARTBs are observed to have temperatures of between $4 - 8$ MK, with durations of $2 - 7$ minutes (Shimizu, 1995). The lengths and widths of the events are given as $5 \times 10^3 - 4 \times 10^4$ km and $2 \times 10^3 - 7 \times 10^3$ km, respectively, giving a range of areas between $1 \times 10^7 - 2.8 \times 10^8$ km^2. The energy released from these events was estimated by Shimizu et al. (1994) to be approximately 10^{29} ergs, suggesting that ARTBs are at the low end of the sub-flare energy range, but larger than microflares. The global frequency of these events was found to be approximately 3 per minute in *active* active regions and 1 per hour in *quiet* active regions (Shimizu et al., 1994). Furthermore, Berghmans and Clette (1999) claim to have detected the 'cooler and weaker EUV counterparts' of the ARTBs described by Shimizu (1995) using EIT/SOHO Fe XII (formed at 1.6×10^6 K) data. These events have durations of between $1.5 - 10$ minutes, and areas between $1.5 - 10 \times 10^7$ km^2. They suggest that the elongated nature of these events means that they may be related to compact loops. They also suggest that the average intensity enhancement of 100% (i.e. a factor of 2) is quite exceptional.

More recently, Berghmans et al. (2001) analysed SXT, EIT and TRACE data for ARTBs. They find that the stronger ARTBs (found using SXT) correspond to several EUV brightenings, but the weaker events have no EUV counterpart at all. Similarly the weaker EUV events have no soft X-ray counterpart.

1.4.11 Network flares

Network flares are described by Krucker et al. (1997) as brightenings occurring in the quiet Sun corona above the magnetic network. They have average lifetimes of 10 minutes, are an order of magnitude smaller than ARTB's and occur every 3 seconds on the Sun. Krucker et al. (1997) observed these network flares using Yohkoh SXT data and calculated that each event has an energy of 10^{25} ergs and a temperature up to 1.8×10^6 K. They suggest that the variations in temperature and emission measure of network flares is consistent with the evaporation of cooler chromospheric and transition region plasma. Also, the ratio of total energies radiated in the soft X-rays and in radio frequencies is similar to that of flares, hence their name, network flares.

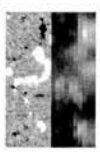

1.4.12 Summary

Table 1.1 shows a summary of the solar zoo phenomena and their properties. There are some gaps in the table where some properties have not been calculated in the analysis of the phenomena.

1.5 BLinker Identification Program (BLIP)

All the initial results of blinkers (Harrison, 1997; Harrison et al., 1999) were carried out using manual detection and analysis techniques. We use a more robust detection method in the hope of finding more events, as the results of Berghmans et al. (1998) and Brković et al. (2001) seem to suggest there should be.

In order to objectively detect blinkers, we have designed a BLinker Identification Program (BLIP) which is an automated method of finding blinkers from a series of CDS rastered, feature tracking data. The algorithm finds groups of pixels that have 'significant' simultaneous peaks.

In order to determine if a peak is significant we first calculate the statistical error of each pixel using the method described in Thompson (1998), where the statistical noise is given by,

$$f_N = \sqrt{\frac{2}{N}} \tag{1.1}$$

where N is the number of photons/pixel. The noise must be calculated in this way because the 4 dimensional CDS data has been reduced to 3 dimensions by simply summing up the spectral data in each pixel rather than fitting a line to it. For each data series and each particular wavelength an error threshold (λ) is then determined; λ is defined as the value below which 99% of the errors exist.

For each pixel in the data array all the local temporal maxima and minima (peaks and troughs) are identified. Clearly, not all peaks are going to be associated with a blinker. We only keep peaks that are larger than $n_\lambda \lambda$, where n_λ is a positive integer that is specified. To determine each pixel's significant temporal peaks, the largest peak in each pixel's time series is taken and the difference between it and the minimum trough both before and after is calculated. If the value of the intensity jump between the peaks and troughs is larger than the threshold, $n_\lambda \lambda$, then the peak

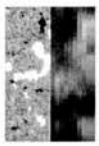

Phenomena	Atmospheric layer	Region	Temperature (K)	Area (km^2)	Lifetime (mins)	Global frequency (s^{-1})
Ephemeral regions	P	QS, AR, CH	-	10^3 km [1]	264	0.5
Cancelling magnetic features	P	QS, AR, CH	-	$< 10^3$ km [1]	60 - 1440	0.15 - 0.25
Spicules	Ch	QS, AR, CH	$1 - 2 \times 10^4$	$\approx 5 \times 10^6$	15	100-200
Blinkers	TR	QS, AR	2.5×10^5	3.0×10^7	17	7.5 (QS), 13.7 (AR)
SUMER 'unit' brightenings	TR	QS	7×10^4	$\approx 2 \times 10^3$	4	
Explosive Events	TR	QS, AR, CH	$\approx 10^5$	$1.5 - 3 \times 10^3$	1	≈ 600
Network and cell brightenings	Ch, TR	QS	1×10^4 - 2.5×10^5	$3.5 - 17.7 \times 10^6$	1.6	
Active TR brightenings	TR	AR	$3 - 4 \times 10^5$		> 720	
UV 'bursts'	Ch, TR, C	AR	$2 - 200 \times 10^4$	$3.6 - 10.8 \times 10^3$	10	
Nanoflares	C	QS, AR, CH	$1 - 3 \times 10^6$	10^7	10	140
AR transient brightenings	C	AR	$4 - 8 \times 10^6$	$1 - 28 \times 10^7$	5	3×10^{-4} (QS), 0.05 (AR)
Network flares	C	QS	1.4×10^6	$\approx 10^6$	10	10

[1] separation

Key: P - photosphere, Ch - Chromosphere, TR - transition region, C - corona, QS - quiet Sun, AR - active region, CH - coronal hole

Table 1.1: Properties of the solar zoo phenomena

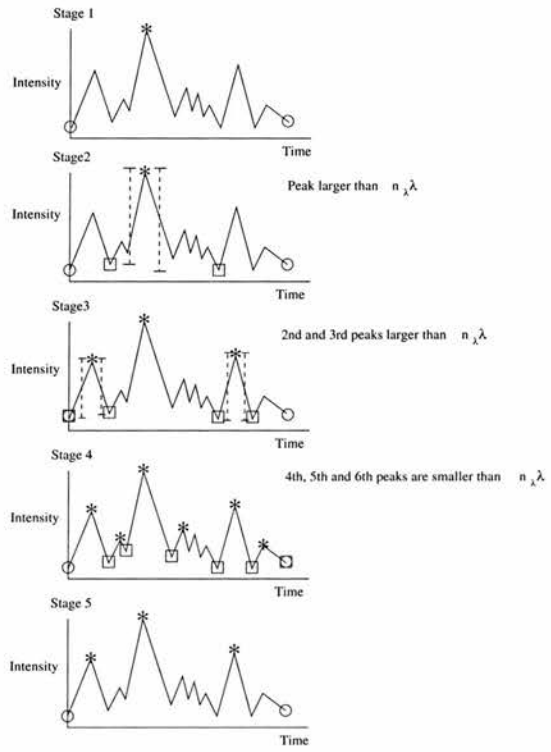

Figure 1.10: Illustration of how significant peaks are chosen in BLIP. The peaks investigated are denoted by an $*$ which remains if the peak is significant. The $\square$s denote the minimum troughs either side of the peaks investigated.

is kept and the process repeated for the time interval before and after the maximum peak. If the difference in intensity is less than $n_\lambda\lambda$, then the peak is neglected and that section of the time series is investigated no further. Figure 1.10 shows a schematic of how this procedure works. In the first graph, we identify the maximum peak in the time series. In the second graph, we identify the minimum trough on either side of the peak. The intensity jump between the peak and the troughs is found to be greater than $n_\lambda\lambda$, and so the peak is kept. In the third graph, we identify the largest peaks on either side of the first peak and the minimum troughs on either side of the peaks. Both of the intensity jumps are larger than $n_\lambda\lambda$ and so both peaks are kept. In the fourth graph, we identify the next largest peaks in the time series and their minimum troughs. None of the intensity jumps are greater than $n_\lambda\lambda$, so the peaks are neglected and the time series is investigated no further. We are left with three significant peaks for this time series.

Adjacent pixels that peak in the same image are grouped together to form an event. A pixel is said to be adjacent to another if it is one of the 8 surrounding pixels. A group must have at least

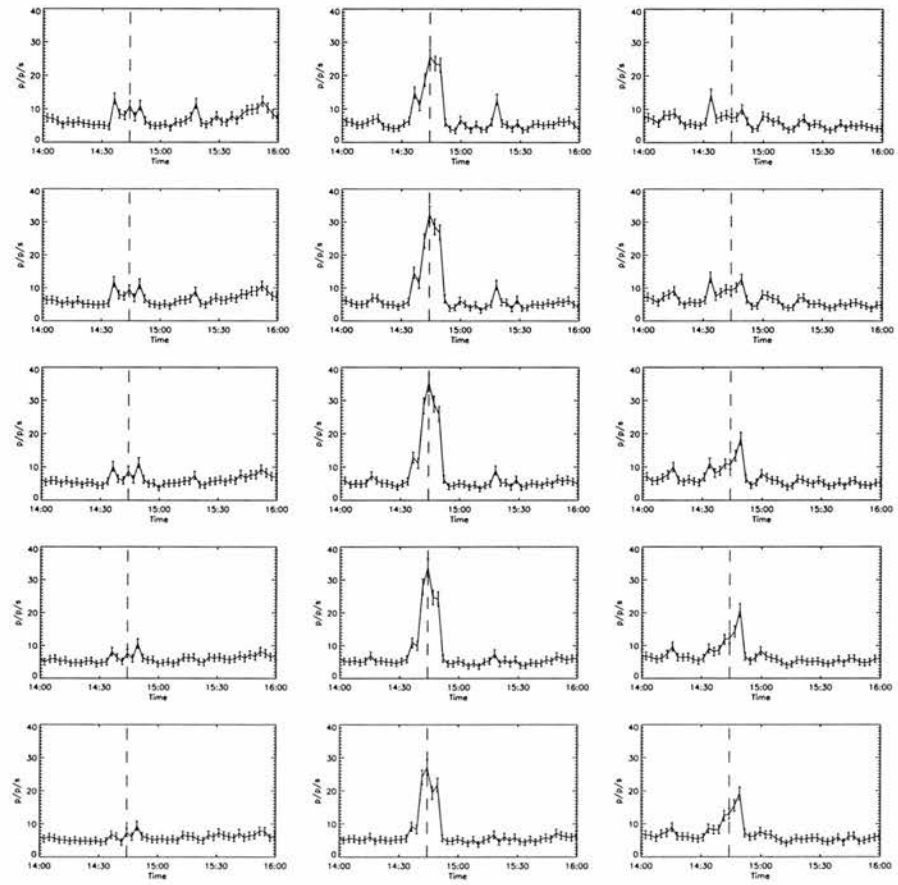

Figure 1.11: Intensity profiles of 15 pixels in an O V CDS raster. BLIP identified a blinker in the 5 pixels in the middle column. The *dashed* line marks the peak of the blinker.

n_p pixels to be counted as an event, where n_p is a positive-integer that is specified.

A check is then made to see if each event is actually a blinker by testing to see if it still meets the criteria for a blinker, i.e. its peaks and troughs are identified and compared in the same way as above. If a peak is identified in the group intensity profile at the same raster as the original peak used to group the pixels, and this peak is still greater than $n_\lambda \lambda$ above the troughs, then the group is counted as a blinker. This step is necessary because it is possible that the sum of the pixel intensities may smooth out any peak if some of the troughs about the peak are widely separated in the different pixels that make up the group.

Having found all the blinkers, their properties can be determined. Area, lifetime and intensity enhancement factor are all calculated from the intensity curves and the number of events and global frequency are determined. Full details of how BLIP works can be found in Appendix 1.

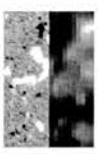

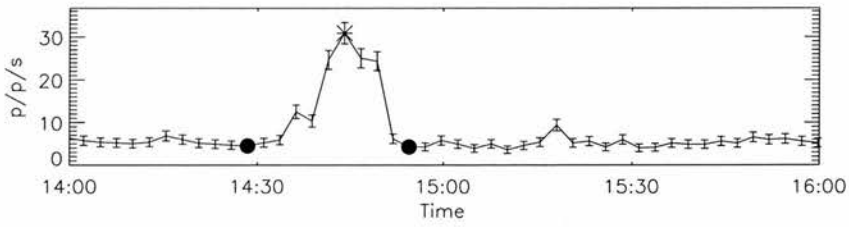

Figure 1.12: Intensity profile of the integrated blinker pixels shown in Figure 1.11. The $*$ marks the peak of the blinker and the $\bullet$'s mark the start and end of the blinker.

As an example, Figure 1.11 shows the lightcurves of 15 pixels from an O V CDS raster. The 5 pixels in the middle column all have an intensity jump that is greater than $n_\lambda \lambda$ (where $n_\lambda = 5$ and $\lambda = 3.64$) and all peak at the same time marked by the *dashed* line. These pixels are grouped together as a blinker, and the intensity integrated over these 5 pixels produces the blinker intensity profile shown in Figure 1.12. The peak of the blinker is shown with an $*$ and the start and end of the blinker are marked with $\bullet$.

1.6 Aims

In this thesis, we study the solar transition region by making a thorough investigation of one of the phenomena that occur in it, blinkers. We use an automated identification procedure to search for blinkers and determine their properties in both quiet Sun and active regions. As mentioned in Section 1.3, the general properties of blinkers, their size, lifetime, global frequency etc, have been determined by a number of authors. In this thesis, we develop an automated method of identifying blinkers, which is far less subjective than the methods used previously. We confirm a number of previous results using the blinkers identified with the automated algorithm and also complete the first thorough study of active-region blinkers. To enable us to suggest possible mechanisms that cause blinkers, we study both the velocity of plasma within blinkers and also investigate the photospheric magnetic field beneath them. These two pieces of information are essential if a model is to be developed to explain these transition region phenomena. We also compare blinkers with explosive events, another transition region phenomenon and try to determine the links between the two events. This thorough study will provide an unique insight into blinkers, the whole of the transition region and its links with the rest of the solar atmosphere.

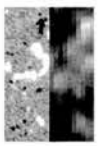

Chapter 2

Quiet-Sun Properties

In this Chapter, we investigate the general properties of quiet-Sun (QS) blinkers identified with BLIP in the CDS O V emission line. In Section 2.1, we describe the data used, then we compare the area, lifetime, intensity enhancement factor and global frequency of blinkers found using different n_p and n_λ parameter inputs to BLIP in Section 2.2. We examine blinker intensity profiles, and their shapes in Section 2.3. In Section 2.4, we look for any signature of the O V blinkers in the five other CDS wavelengths which range from the chromosphere through the transition region and into the corona. We investigate whether blinkers are a density or a temperature event using line ratios in Section 2.5 and in Section 2.6 we determine the relationship between blinkers and the quiet-Sun network. Finally, in Section 2.7 we make our concluding remarks. All discussion of the results are left until Chapter 7. Further properties of QS blinkers can be found in Chapters 4 and 5, where we examine the velocity and magnetic structure and Chapter 6 makes a comparison of blinkers and explosive events in a quiet-Sun region.

2.1 Data

In this chapter, we use data taken by the SOHO/CDS normal incidence spectrometer (NIS). The data sequence was taken using the $4'' \times 240''$ slit, but only the central $124''$ were telemetered, hence the slit rasters have an area of $40'' \times 124''$ (29 000 km $\times$ 90 000 km), which covers 0.04% of the solar surface. The exposure time at each slit location is 10 seconds and the entire raster has a duration of 151 seconds. Each pixel is $4''$ in the solar-x direction and $1.7''$ in the

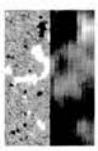

solar-y direction, producing rasters of size 10 × 73 pixels. The data contains 6 emission lines, He I 584Å, O III 599Å, O IV 554Å, O V 629Å, Mg IX 368Å and Mg X 624Å formed at temperatures of 2 $\times 10^4$ K, 1 $\times 10^5$ K, 1.6 $\times 10^5$ K, 2.5 $\times 10^5$ K, 1 $\times 10^6$ K and 1.2 $\times 10^6$ K, respectively.

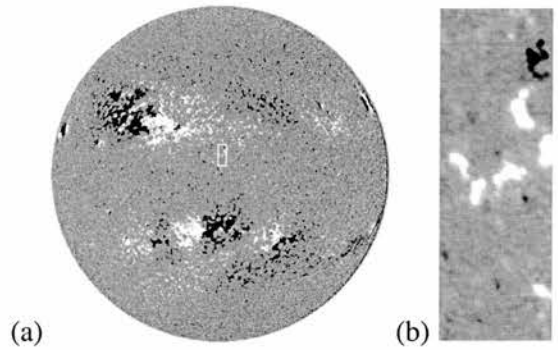

Figure 2.1: (a) Full disk MDI magnetogram taken on 29th November 1998 at 12:48 UT. The white box indicates the area covered by the CDS rasters investigated. (b) Partial frame high resolution MDI magnetogram showing the magnetic field below the CDS raster.

The data sequence analysed (S15251) was taken on 29th November 1998 and lies over a region of quiet sun as can be seen in Figure 2.1. The start of the observation run was 11:27 UT and it lasted almost 12 hours; there were 270 rasters. The coordinates of the centre of the first raster are 4.80″W and 111.50″N. The observations are feature tracked by the movement of the mirror until it has reached its maximum offset and then by the movement of the legs so the mirror can once more scan its full range.

The standard CDS software is used to correct the data for missing pixels, CCD readout bias and cosmic ray hits, flat fielding effects and finally a calibration is used to convert the data units to photons-events per pixel per second (p/p/s). The tilt between the NIS dispersion axis and the CCD detector is corrected for, however, the standard correction is not applied because it has been found that the tilt is dependent on time and mirror position (see Appendix B). The rotation effect of the Sun is removed from the data by using ROTXY from solarsoft (the publically available package of IDL analysis routines including Yohkoh, SOHO and TRACE tools). All images are rotated back to the first image which is used as a reference point. Since the CDS pixels are several arcsecs in the x-direction many of the images are rotated back by a fraction of a pixel. We use bicubic interpolation to achieve this sub pixel rotation.

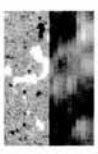

2.2 Properties of quiet-Sun blinkers

We use BLIP (see Section 1.5 and Appendix A) to investigate a series of different sizes of blinkers by varying the minimum size, n_p, and minimum intensity jump factor, n_λ, in each run of our algorithm. The following combinations of n_p and n_λ were considered: $n_p = 1, 2$ or 3 CDS pixels and $n_\lambda = 5$; and $n_p = 3$ and $n_\lambda = 3$ or 10. The error threshold, λ, for the O V data equals 3.64 p/p/s. Table 2.1 shows the numbers and properties of the QS blinkers identified.

Properties	n_λ	3	5	5	5	10
	n_p	3	1	2	3	3
No. of blinkers		356	214	171	136	17
Global frequency (s^{-1})		19.5	11.7	9.4	7.5	0.9
Mean intensity enhancement factor		1.7	1.7	1.8	1.8	2.1
Mean area ($\times 10^7$ km^2)		3.1	2.0	2.5	2.9	2.9
Mean lifetime (minutes)		16.4	16.4	16.4	16.4	21.0
Mean rise time (minutes)		8.1	8.3	8.2	8.2	10.6
Mean fall time (minutes)		8.3	8.2	8.2	8.2	10.3

Table 2.1: Properties of the quiet-sun blinkers identified using BLIP.

The mean areas and mean lifetimes determined for the QS blinkers are found to be comparable with those found by Harrison et al. (1999), Berghmans et al. (1998) and Brković et al. (2001). Furthermore, they do not vary greatly with a change in the parameters, n_λ and n_p. The maximum area of a QS blinker is found to be 5.5×10^8 km^2, and the minimum area is restricted by the choice of n_p and equals $3.6\ n_p \times 10^6$ km^2.

The mean lifetime of the QS blinkers identified with each criterion is about 16.5 minutes. The longest blinkers are identified with $n_\lambda = 3$ and $n_p = 3$ and have a lifetime of order 40 minutes. The shortest blinkers are identified with $n_\lambda = 3$ and $n_\lambda = 5$ and have lifetimes of the order of 6 minutes. This lower limit is instrumental and is simply the shortest observable blinker time with our data set.

The mean rise and fall times of the QS blinkers appears to be equal, however, on closer inspection, we see that this does not mean that in each blinker the rise time equals the fall time. In

all cases, except $n_\lambda = 10$ and $n_p = 3$, the numbers of blinkers with rise time greater than fall time, and fall time greater than rise time is approximately 40%. In just 20% of cases the rise and fall time are approximately equal. In the $n_\lambda = 10$ and $n_p = 3$ case we find that there are more blinkers (45%) with fall time greater than rise time, but still approximately 20% of cases have almost equal rise and fall time.

The intensity enhancement factors, which are defined as the peak intensity minus the mean of the start and end intensities divided by the mean of the start and end intensities, are higher than those observed by Harrison et al. (1999). The reason for this is not clear, although it may be due to a difference in the way the lower intensity bound is determined. We consider the change from the start and end troughs on either side whilst Harrison et al. (1999) estimate the change from the pre-event intensity. The intensity enhancement factors found are comparable with Brković et al. (2001) who found 1.6, and they lie within the range 1.1 to 2.7 found by Berghmans et al. (1998).

Not surprisingly, we find a much greater global frequency than Harrison et al. (1999); the global frequency is defined as the number of blinkers that occur on the whole sun per second assuming that our CDS field of view is representative of the whole sun. The global frequencies found here span the same range as Berghmans et al. (1998) and our highest global frequency is similar to that found by Brković et al. (2001) who also used an automated identification method. This confirms our hypothesis that Harrison's manual detection is a difficult and time consuming process and is rarely as successful as automated detection, especially for blinkers with small intensity enhancement factors and so is the reason why the global frequency found by Harrison et al. (1999) was so low.

In the case where n_λ is held fixed and n_p decreases from 3 to 2 and from 2 to 1, we see 25% more QS blinkers identified each time. Similarly, when n_p is held fixed at 3 and n_λ is decreased from 10 to 5 and from 5 to 3 we find 800% and 240% more QS blinkers, respectively. These increases are not too surprising since we are allowing smaller events to be counted as blinkers each time. We feel that an intensity jump factor around 3 or 5 is probably a reasonable value. Any lower value would involve many fluctuations due to noise being counted as blinkers. Similarly it is preferable to have a blinker detected in more than one pixel, however, we have to bear in mind that the CDS pixels are fairly large and so an instrument with higher spatial resolution would be desirable to reliably estimate the sizes and numbers of blinkers.

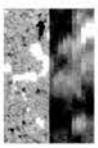

2.3 Intensity profiles

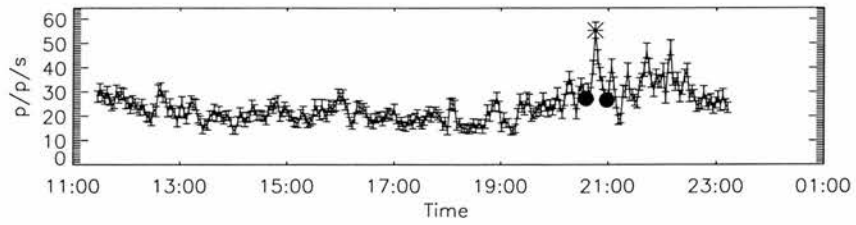

Figure 2.2: A typical O V QS blinker identified with $n_\lambda = 5$ and $n_p = 3$. The $*$ shows the peak, and the •s mark the start and end of the blinker.

In Figure 2.2, the intensity of a typical O V QS blinker is plotted against time. The peak of the blinker ($*$) and the beginning and end of the blinker (•s) are marked. The statistical error of the intensity calculated using Equation 1.1 is also plotted. Due to the large number of data points on this graph the profile of the blinker is hard to distinguish - Figure 2.3 shows a close up of the blinker.

Looking at all the blinker light curves we see that there appear to be two types of blinker activity. The first is repetitive in nature - the same group of pixels peak more than once during the observing period - and the second show no recurrence. Approximately 75% of QS blinkers studied display a repetitive nature, with just 25% of QS blinkers having one single peak during the observing period. The high percentage of repetitive brightening is suggestive that the mechanism that causes blinkers is not an irreversible process such as reconnection but rather a more subtle process that can switch off and on. Harrison et al. (1999) found that there is a 50% chance of a blinker onset on the same site within 3 000 s (50 mins). It is possible that there may be some sort of periodicity to the repetition of peaks in the blinker light curves. To test this hypothesis we analysed the blinker light curves using Fourier analysis. Our analysis revealed no sign of any periodicity or oscillatory behaviour. This may be because the recurrence rate of blinkers is on the order of several hours, rather than the hour suggested by Harrison et al. (1999) and our 12 hour data sets are not long enough to show these. We also attempted some wavelet analysis to see if the blinkers appeared in groups, but again, we saw no sign of any distinct wave packets.

2.4 Blinker signatures in other wavelengths

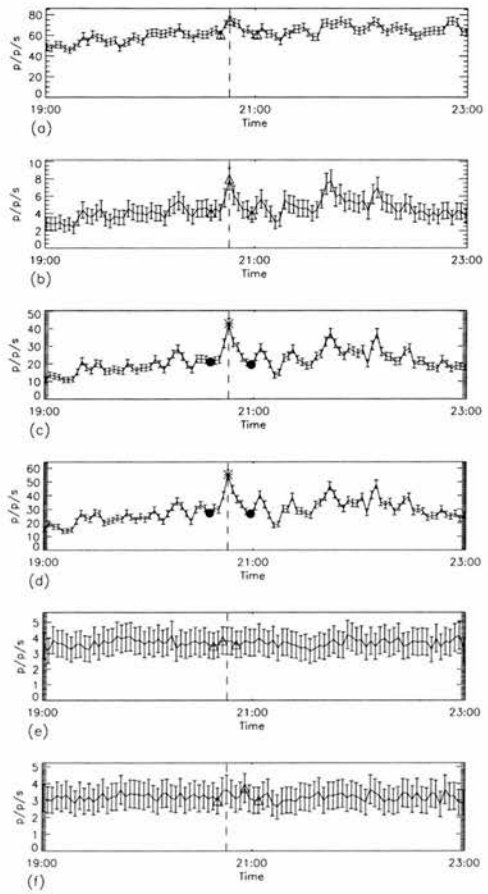

Figure 2.3: Comparison of intensity light curves for a QS blinker identified in O V seen in different wavelengths, (a) He I, (b) O III, (c) O IV, (d) O V, (e) Mg IX, and (f) Mg X. The $*$ mark the peaks of identified blinkers, and the $\bullet$s mark the starts and ends of the blinkers. The $\triangle$s mark the start, peak and end of all enhancements found by BLIP that are not large enough to be blinkers. The *dashed* line indicates the peak of the O V blinker.

In Figure 2.3, the light curves relating to the same group of pixels as shown in Figure 2.2 are plotted against time for He I, O III, O IV, O V, Mg IX and Mg X, (a) - (f), respectively). Each light curve is investigated to determine whether it has a peak at the right time that satisfies the criteria for a blinker. An enhancement in intensity can be seen in the He I, O III, O IV and O V lines. The only one of these events, however, apart from the O V, to meet the criteria for a blinker is the O IV peak.

The QS blinker identified in O IV starts, peaks and ends at the same time as the O V blinker.

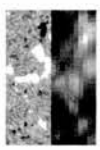

Even though a blinker is not registered in the O III line, there is a noticeable ($n_{\lambda \mathrm{OIII}} = 2.8$) increase in intensity which starts, peaks and ends at the same time as the other O line blinkers. There is also a notable ($n_{\lambda \mathrm{HeI}} = 2.6$) increase in intensity in the He I line. These are identified by $\triangle$s.

Wavelength	n_λ	3	5	5	5	10
	n_p	3	1	2	3	3
O V		356	214	171	136	17
He I/O V		104	58	46	37	1
O III/O V		23	3	3	2	0
O IV/O V		323	171	143	118	14
Mg IX/O V		0	0	0	0	0
Mg X/O V		0	0	0	0	0
He I/O IV/O V		99	50	40	34	1
He I/O III/O V		17	3	3	2	0
O III/O IV/O V		23	3	3	2	0
He I/O III/O IV/O V		17	3	3	2	0

Table 2.2: Number of events identified as QS blinkers in O V and other wavelengths.

The blinker picture in Figure 2.3 is similar to that seen in about 25% of the QS blinkers identified. Table 2.2 shows the numbers of blinkers observed first in O V and then in one, two or three other wavelengths. In all cases, 80-91% of the O V blinkers were also identified in the O IV line; this confirms the results by Harrison et al. (1999) that the blinkers are most evident in the O V and O IV transition region lines. The majority of these blinkers are also identified in He I. Indeed, in all cases, except one ($n_\lambda = 10$ and $n_p = 3$), 23-28% of blinkers identified in O V are also identified in the He I and O IV. In the $n_\lambda = 10$ and $n_p = 3$ case only 6% of blinkers are identified in these three wavelengths. In all cases, less than 6% of O V blinkers were seen in the O III line. These blinkers are generally the strong blinkers and are also visible in the O IV and He I. No QS blinkers were identified in either of the hotter coronal magnesium lines. The reason blinkers have not been identified in the O III and the coronal lines may be because these lines are weak in quiet regions or it may be because blinkers do not have coronal counterparts.

To establish the size of the intensity enhancements identified in the other wavelengths at the

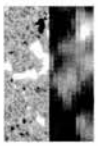

same time as the QS blinker in O V, we calculated the size of the peaks in the same way as we tested to see if the peaks were blinkers. Table 2.3 shows the range of the sizes of peaks in terms of their peak-size factors even if this factor is less than that required for a blinker. The results shown are only for the events associated with blinkers seen in O V and with $n_\lambda = 5$ and $n_p = 3$.

Wavelength	λ	Minimum peak factor	Maximum peak factor	% w. peak factor > 1	% w. peak factor > 3
He I	5.35	0.0	12.4	89.7	47.8
O III	1.40	0.3	5.4	94.1	21.3
O IV	3.16	2.3	13.1	100.0	99.3
O V	3.64	5.1	12.4	100.0	100.0
Mg IX	1.15	0.0	1.4	8.0	0.0
Mg X	1.05	0.0	1.8	13.2	0.0

Table 2.3: Range of peak-size factors for events in all wavelengths first identified as O V QS blinkers with $n_\lambda = 5$ and $n_p = 3$.

The results in this table show that the peaks identified in the coronal (magnesium) lines are much smaller than that required for a blinker, with just 8.0% and 13.2%, respectively, for the Mg IX and Mg X having peak factors greater than 1. The largest O III peak is only just significant enough to be counted as a blinker, with a peak factor of 5.4. In the other O lines (O IV and O V) and the He I line the majority (99%, 100% and 48%, respectively) of peak factors are above 3. The maximum peak factors of the blinkers in these wavelengths are not a lot bigger than 10, confirming our thoughts that $n_\lambda = 10$ just identifies the very large blinkers.

2.5 Line ratios

Figure 2.4 (a) shows the light curve seen in Figure 2.2 whilst Figures 2.4 (b)- (d) show its ratio with the He I, O III and O IV light curves, respectively. The *dashed* line marks the position of the peak of the O V blinker in all figures. The ratio of the oxygen lines show no significant temporal variations. This is similar to the result found by Harrison et al. (1999) and suggests that QS blinkers are not temperature enhancements but rather enhancements in density or filling factor.

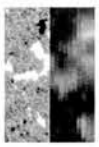

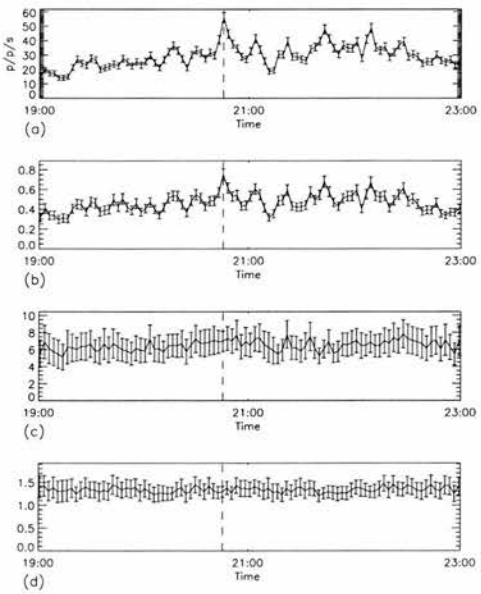

Figure 2.4: (a) Typical O V light curve, (b) Ratio of O V/He I, (c) O V/O III and (d) O V/O IV. The *dashed* line indicates the peak of the O V blinker.

We considered, for all our blinkers, the minimum, mean and maximum values of the line ratios of the light curves calculated between the start and end of the O V blinker, as well as for the entire ratio of the light curves (Table 2.4).

Wavelength	Minimum		Mean		Maximum	
	Entire	Blinker	Entire	Blinker	Entire	Blinker
He I	0.26	0.32	0.42	0.48	0.54	0.93
O III	3.93	4.77	6.26	6.38	7.22	7.74
O IV	1.14	0.99	1.32	1.29	1.59	1.57
Mg IX	3.14	3.36	7.79	8.18	15.72	16.96
Mg X	3.38	6.04	10.16	11.97	13.94	18.85

Table 2.4: Minimum, mean and maximum line ratio values for the entire light curve and for the blinker region only.

It appears in all cases as if the blinker part of the light curve ratio is slightly bigger than that normally observed, except for the ratio of O V/O IV where the blinker ratio is slightly lower than expected. If these deviations were real it would imply that the typical temperature of a blinker lay somewhere between 1.6×10^5 K and 2.5×10^5 K, however, the typical 1 σ error

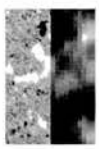

on these ratios is 1.32 and 0.17 for the O V/O III and O V/O IV ratios, respectively. Since the differences between the mean values of the blinker and entire light curves are always less than these errors it is unlikely that the differences are real, hence, we conclude that the ratios of the oxygen species are effectively flat and so agree with the results of Harrison et al. (1999).

2.6 Relationship to network

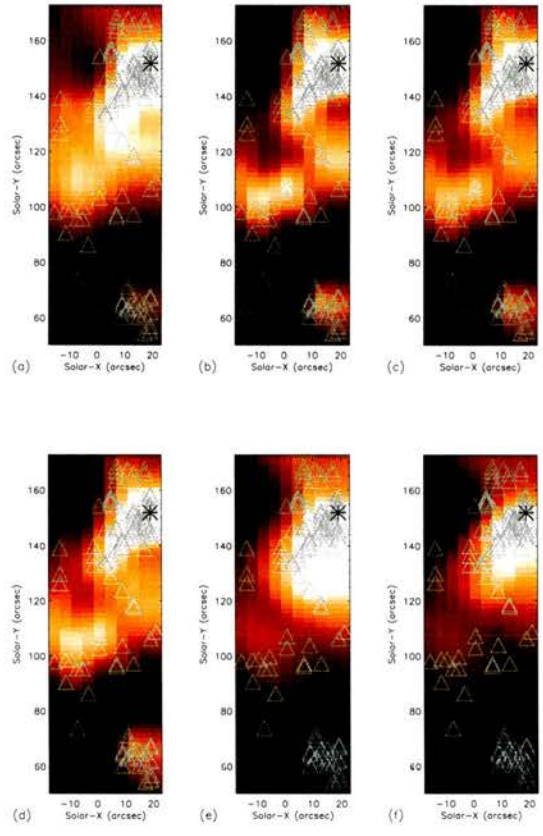

Figure 2.5: Comparison of the location of QS blinkers with the network. Time integrated emission of the derotated (a) He I, (b) O III, (c) O IV, (d) O V, (e) Mg IX and (f) Mg X rasters. Each △ represents a blinker and the ∗ refers to the QS blinker seen in Figure 2.2.

To compare the location of the QS blinkers with the network and the emission from other wavelengths, we plot the integrated emission over the entire observing sequence of the derotated He I, O III, O IV, O V, Mg IX and Mg X rasters, Figure 2.5 (a) - (f), respectively. The △'s represent the location of the midpoints of the blinkers, and the ∗ in the top right-hand corner shows the

midpoint of the blinker that has been discussed in detail.

Clearly the blinkers are not distributed uniformly over the field-of-view. Indeed, just the odd one or two blinkers seem to appear off the network boundary. To see if the blinkers are distributed uniformly with respect to intensity, which from the images they clearly appear not to be, we use a likelihood statistical test. First we determine the numbers of pixels with intensities in certain ranges. These ranges (bins), of which there are k, are chosen such that the width of the bin increases by a factor of 2 for increasing intensity. We define M to be the total number of pixels and M_i to represent the numbers of pixels in the ith range. Similarly, n represents the total number of pixels associated with the peak of each blinker whilst n_i is the number of these pixels with intensities in the ith range. The likelihood ratio statistic, w_k, is then defined as

$$w_k = 2n_i \sum_{i=1}^{k} log\left(\frac{n_i M}{n M_i}\right) . \tag{2.1}$$

We can now compare w_k with the expected χ^2_{k-1} statistic. If w is large compared to χ^2_{k-1}, the distribution is not uniformly distributed, and suggests they are dependent on the brightness of emission.

Wavelength	k	χ^2_{k-1}	Likelihood ratio statistic
He I	4	17.73	795.622
O III	4	17.73	3129.42
O IV	6	22.11	4078.15
Mg IX	3	15.20	853.596
Mg X	3	15.20	957.243

Table 2.5: Values of the likelihood ratio statistic and corresponding χ^2_{k-1} statistic for QS blinker events identified with $n_\lambda = 5$ and $n_p = 3$.

The results of this analysis for the $n_\lambda = 5$ and $n_p = 3$ case are shown in Table 2.5. In all cases the likelihood ratio statistic is substantially (between 50 and 200 times) greater than the χ^2_{k-1} value, so clearly the blinkers are not uniformly distributed. This is no surprise for the O V blinkers, since by definition they are the brightest pixels, however, it is interesting that this still holds for the coronal lines even though we cannot detect blinkers there.

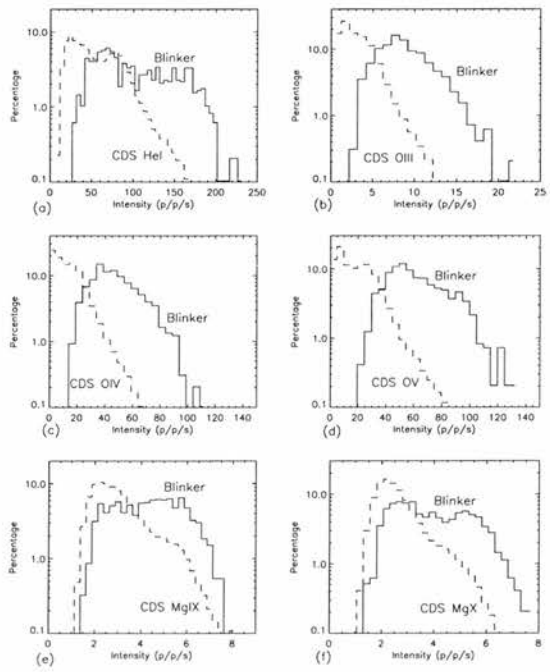

Figure 2.6: Histogram of distribution of all pixels intensities (*dashed*) and QS blinker pixel intensities (*solid*) for (a) He I, (b) O III, (c) O IV, (d) O V, (e) Mg IX and (f) Mg X lines respectively.

In most cases the QS blinkers appear to occur above regions of enhanced emission. Further analysis is used to determine whether blinkers are located over the areas of strongest emission. Figure 2.6 shows the distribution of intensity of CDS pixels in all wavelengths and QS blinker pixels (identified with $n_\lambda = 5$ and $n_p = 3$) at the time of the blinker peak. The *solid* line shows the distribution of pixels associated with blinkers and the *dashed* line shows the distribution of all pixels. From Figure 2.6 we can see that in all wavelengths the pixels with the weakest emission are not associated with blinkers and in the cases of He I, O III, O IV and O V the blinkers are clearly associated with the top few percent of pixels with the highest intensity. This, as already said, is no surprise in the case of O V since, by definition, blinkers are the high emission pixels, however, since this pattern is mirrored in the other wavelengths it implies that blinkers probably generally have similar signatures in these other wavelengths too. Also it confirms the results of Harrison et al. (1999) that QS blinkers occur above the network in quiet-Sun regions. Surprisingly, there is also an association between the highest intensity pixels and QS blinkers in the coronal Mg IX and Mg X lines, eventhough no blinkers were identifed in these lines.

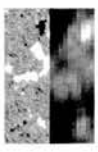

2.7 Conclusions

Our results confirm the properties of O V QS blinkers discovered by Harrison (1997), Harrison et al. (1999), Berghmans et al. (1998) and Brković et al. (2001). We find lifetimes from the data resolution up to 40 mins (mean 16 minutes), areas from 1 pixel up to 5.5×10^8 km^2 (mean approximately 3×10^7 km^2 or 8 pixels) and intensity enhancement ratios of around 1.8. The global frequency is, as expected, much higher than Harrison et al. (1999), but in agreement with Berghmans et al. (1998) and Brković et al. (2001) at around $1 - 20$ s^{-1} depending on whether large or small peak intensities are demanded. The ratios of the oxygen lines are again shown to be flat confirming the results of Harrison (1997) and Harrison et al. (1999) that QS blinkers appear to be increases in density or filling factor.

We have investigated the rise and fall times of the O V QS blinkers. There does not appear to be a clear pattern with 40% having a faster rise than fall time, 40% with a faster fall than rise time and 20% with effectively equal rise and fall times. The mean rise and fall times are both about 8 minutes. The 'blinking' nature of QS blinkers was also investigated with approximately 75% of blinkers having a repetitive nature. Fourier and wavelet analysis, however, do not reveal evidence of any periodic behaviour in blinkers.

QS blinkers that are identified in O V can also be readily detected as blinkers in O IV and He I with $80 - 91\%$ and $23 - 28\%$ of the O V blinkers detected in these lines, respectively. The O IV and He I lines are two of the strongest transition region and chromospheric lines, respectively, that CDS has. In the weaker line, O III, the blinkers are much harder to detect with less than 6% of the O V blinkers seen. The blinkers detected in these wavelengths tend to occur simultaneously with the O V blinkers. No significant peaks at the time of the blinkers are seen in the Mg IX and Mg X coronal lines. In the cases of 8% and 13% of the O V blinkers, small intensity enhancements greater than $n_{\lambda \mathrm{MgIX}} = 1$ and $n_{\lambda \mathrm{MgX}} = 1$ are observed, respectively for the Mg IX and Mg X lines. These results suggest that QS blinkers have no coronal signatures, however, it may be simply that these lines are too weak to detect anything in.

Statistical analysis has been used to confirm that the distribution of QS blinkers is not uniform and they are preferentially located in regions of strongest emission in the chromospheric, transition region and coronal lines studied. This suggests that they are (i) located over the network and that (ii) the signatures of QS blinkers in the He I and oxygen lines are all very similar.

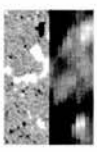

Chapter 3

Active-Region Properties

As in the previous Chapter, we investigate the properties of blinkers but this time in an active-region (AR) data set. The discovery of AR blinkers was an accident. This was the first data set that we analysed using BLIP but we were unaware at the time that it was of an active region until we analysed the associated MDI data. This aspect is discussed in more detail in Chapter 5. We follow the same pattern as in the previous Chapter; in Section 3.1, we discuss the data used; in Section 3.2, we compare the properties of AR blinkers identified using different n_p and n_λ input parameters to BLIP. The signatures of the blinkers in a variety of CDS wavelengths are examined in Section 3.3 and the line ratios are investigated in Section 3.4. We consider the relationship of blinkers to active-region emission in Section 3.5 and finally, we make some concluding remarks in Section 3.6.

3.1 Data

The data used in this Chapter was taken with SOHO/CDS. It has the same properties as the data analysed in Chapter 2, i.e. it contains 6 emission lines (He I, O III, O IV, O V, Mg IX and Mg X), it covers an area of $40'' \times 124''$ with pixels of $4'' \times 1.6''$, the exposure time is 15 seconds and the cadence of the rasters are approximately 151 seconds.

The S11478 data sequence started on 18th June 1998 at 18:17 UT. It was immediately followed by the S11479 data set. Both data sets use feature tracking, as discussed in the previous Chapter, and were joined together to make one data set which lasted 6 hours. A segment of a high

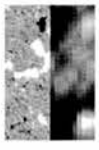

resolution MDI image the same size as the CDS rasters can be seen in Figure 3.1 (b) and shows the magnetic field below the CDS data. Its position on the Sun is indicated by a small white rectangle in the full disc MDI image in Figure 3.1 (a). It is clear that the region observed lies above an active region and contains a large positive polarity sunspot that dominates the field of view. The coordinates of the first raster are 39.6″E and 295.7″N.

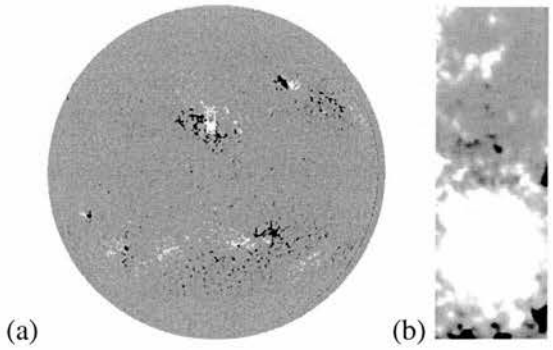

Figure 3.1: (a) Full disk MDI magnetogram taken on 18th June 1998 at 19:12 UT. The small white rectangle indicates the area covered by the CDS rasters investigated. (b) Partial frame high resolution MDI magnetogram (right) taken 5 minutes earlier showing the magnetic field below the CDS rasters.

The data was prepared using the same methods described in Section 2.1.

3.2 Active-region blinker properties

We use BLIP to investigate a series of different sizes of events by varying the minimum size, n_p, and the minimum intensity factor, n_λ, in each run of our algorithm. The error threshold, λ, of the O V data equals 6.97 photons per pixel per second (p/p/s). Table 3.1 shows the numbers and properties of blinkers identified in O V.

From Table 3.1, it is clear that the properties of the O V events identified by BLIP in the active region have similar properties to quiet-Sun (QS) blinkers, as discussed in the Introduction and presented in Chapter 2, and so we call these events active-region blinkers (AR blinkers). Note, however, until we have considered their line ratios (Section 3.4) we cannot say for certain that they really are blinkers.

The mean lifetimes and mean areas of the O V AR blinkers are slightly longer and larger than

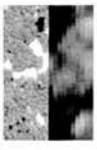

Properties	n_λ	3	5	5	5	10
	n_p	3	1	2	3	3
No. of blinkers		253	224	163	125	64
Global frequency (s^{-1})		27.7	24.5	17.8	13.7	7.0
Mean intensity enhancement factor		1.8	2.1	2.2	2.4	3.3
Mean area ($\times 10^7$ km^2)		3.3	2.4	3.2	3.9	4.3
Mean lifetime (minutes)		16.5	18.0	17.7	17.5	19.3
Mean rise time (minutes)		8.2	8.8	8.5	8.6	9.5
Mean fall time (minutes)		8.3	9.3	9.2	8.9	9.8

Table 3.1: Properties of O V active-region events identified using BLIP.

those found in Chapter 2 for the QS blinkers. Indeed, for each parameter set the mean lifetimes of the AR blinkers are at most 10% longer than for the QS blinkers, whilst their areas are between 6% and 50% larger. The lifetimes of the AR blinkers are similar to those observed by Walsh et al. (1997) for their two blinker-like events. As one would expect, an increase in n_λ generally leads to an increase in both the area and lifetime of the blinkers as the smaller, weaker events are discounted, however, as n_p increases the mean areas increase, but the mean lifetimes fall. The largest blinker observed has an area of 2.7×10^8 km^2 (75 pixels) and covers just over 10% of the raster area. The minimum area of a blinker is, of course, restricted by the choice of n_p and equals $3.6\ n_p \times 10^6$ km^2. The longest lived blinker lasts for just under 42 minutes and is a $n_\lambda = 3$ and $n_p = 3$ blinker. The minimum lifetime of the blinkers is just over 5 mins which is restricted by the time resolution of the data.

The mean rise and fall times of the AR blinkers are consistent with those for the QS blinkers as they again appear to be approximately equal (if anything the mean fall time is slightly longer than the mean rise time). If the individual blinkers are considered, however, it is found that about 40% have longer rise times than fall times, similarly about 40% have the reverse and only 20% have rise times approximately equal to their fall times. This variation in rise and fall times is consistent with the two events found by Walsh et al. (1997) who found that one event had a rise time greater than fall time whilst the other had a rise time less than its fall time.

Just like the mean areas of the blinkers their mean intensity enhancement factors are between 6% and 57% larger than those for the QS blinkers. Furthermore, they also increase with increasing

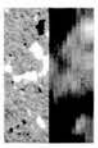

n_λ and n_p. It is important to note that the values of λ in the active region are considerably larger than those in the quiet Sun, hence the actual sizes of the intensity enhancements here are larger still than those in the QS blinkers.

Once again the active region lives up to its name and is found to be more 'active' than the quiet Sun, since it produces blinkers more frequently. Indeed, the global frequencies show that at least 42% more blinkers occur in an active region than in the quiet Sun. The choice of parameters clearly varies the number of blinkers identified. Decreasing the value of n_p from 3 to 2, and from 2 to 1 produces 37% and 30% more blinkers, respectively. A bigger increase is caused, however, with the reduction of n_λ from 10 to 5 and from 5 to 3 where the number of blinkers identified is practically doubled in each case. These increases are similar to those found for the QS blinkers in Chapter 2.

3.3 Signatures of active-region blinkers

Figure 3.2 shows the light curves of a typical AR O V blinker in six different wavelengths (He I, O III, O IV, O V, Mg IX and Mg X, (a) - (f), respectively). The O V light curve of the blinker is very similar to those observed for QS blinkers (Chapter 2). This blinker was detected using the O V wavelength, however, it is also clearly detectable in all other wavelengths other than Mg IX. In the Mg IX we do see an event, but its peak is not significant enough to be counted as a blinker. If we calculate the difference between the peak intensity and maximum of the two troughs either side of the peak, we find that the event has a jump equal to $n_{\lambda MgIX}\lambda_{MgIX}$, where the peak factor, $n_{\lambda MgIX}$, is just 3.7 as opposed to $n_\lambda = 5$. Indeed, if we calculate all the peak factors in the different wavelengths for this blinker we find they equal 31, 8.8, 20, 23 and 6.4 for He I, O III, O IV, O V and Mg X, respectively. Clearly, this blinker is a strong event yet, its signature is only just identified in O III and Mg X. This is probably a reflection of the strength of these lines rather than a significant feature of the blinkers.

We have analysed the O V blinkers to determine how many register as blinkers in the other wavelengths observed. The results are shown in Table 3.2. For all values of n_λ and n_p at least 67-82% of blinkers seen in O V can also be identified in O IV, 59-73% in He I and 16-28% in O III. As in the quiet-Sun case, all the blinkers seen in O III are also visible in O IV and He I. In Mg IX, 6-10% of OV blinkers are seen, whereas in the Mg X, 11-18% are identified. All except

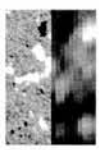

Wavelength	n_λ	3	5	5	5	10
	n_p	3	1	2	3	3
O V		253	224	163	125	64
He I/O V		158	133	105	85	47
O III/O V		68	35	32	30	18
O IV/O V		194	149	117	102	49
Mg IX/O V		19	13	12	12	4
Mg X/O V		30	25	23	22	10
He I/O III/O V		64	35	32	30	18
He I/O IV/O V		143	120	95	83	41
He I/Mg IX/O V		19	13	12	12	4
He I/Mg X/O V		29	25	23	22	10
O III/O IV/O V		68	35	32	30	18
O III/Mg IX/O V		19	12	12	12	4
O III/Mg X/O V		29	24	22	21	10
O IV/Mg IX/O V		19	13	12	12	4
O IV/Mg X/O V		30	25	23	22	10
Mg IX/Mg X/O V		19	12	12	12	4
He I/O III/O IV/O V		64	35	32	30	18
He I/O IV/Mg IX/O V		19	13	12	12	4
He I/O IV/Mg X/O V		29	25	23	22	10
O III/O IV/Mg IX/O V		19	12	12	12	4
O III/O IV/Mg X/O V		29	24	22	21	10
O IV/Mg IX/Mg X/O V		19	12	12	12	4
He I/O III/O IV/Mg IX/O V		19	12	12	12	4
He I/O III/O IV/Mg X/O V		28	24	22	21	10
O III/O IV/Mg IX/Mg X/O V		19	12	12	12	4
He I/O III/O IV/Mg IX/Mg X/O V		19	12	12	12	4

Table 3.2: Numbers of blinkers identified in O V and other wavelengths.

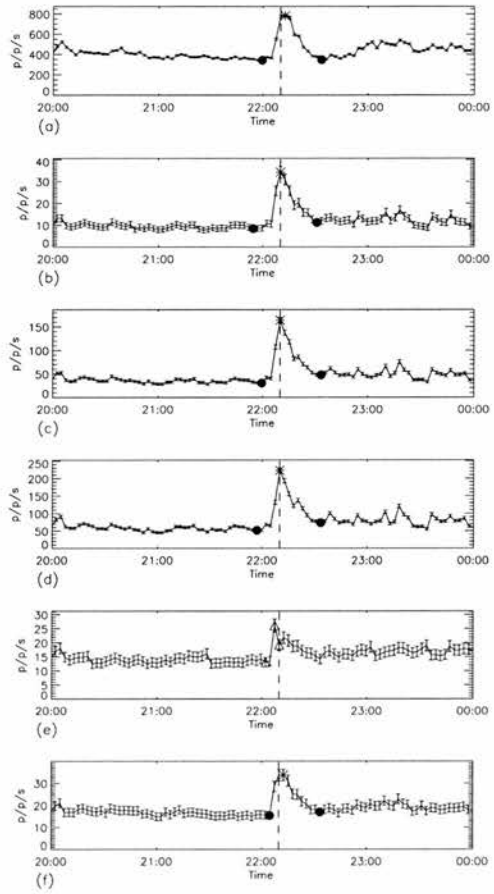

Figure 3.2: Comparison of light curves for a blinker identified in O V and seen in different wavelengths: (a) He I; (b) O III; (c) O IV; (d) O V; (e) Mg IX and (f) Mg X. The stars mark the peaks identified as blinkers and the •s mark their starts and ends whilst the △s mark the start, peak and end of any event not counted as a blinker. The *dashed* line indicates time of the peak of the O V blinker.

one of the Mg IX blinkers can be readily identified in all the other wavelengths, whilst all except two of Mg X blinkers are detected as blinkers in He I, O III, O IV, and O V.

Even though in some emission lines, in particular Mg IX and Mg X, a blinker is not always detected, a peak signature is often seen. We calculate the peak factors of all the signatures that occur simultaneously with the blinkers identified in O V to determine the strengths of the events seen. Table 3.3 gives the λ values for each wavelength, as well as the minimum and maximum peak factors observed. We find that in all wavelengths 47% of the O V blinkers have peak factors greater than 1, whilst 15% have peak factors greater than 3. The minimum peak size factor of

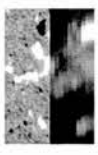

Wavelength	λ	Minimum peak factor	Maximum peak factor	% w. peak factor > 1	% w. peak factor > 3
He I	14.11	0.0	115.4	92.0	78.4
O III	2.78	0.1	32.7	89.6	52.0
O IV	6.26	1.7	66.3	100.0	93.6
O V	6.97	5.3	82.8	100.0	100.0
Mg IX	2.72	0.0	15.2	47.2	15.2
Mg X	2.73	0.0	21.9	71.2	24.0

Table 3.3: Range of peak factors for events in all wavelengths associated with blinkers identified in O V with $n_\lambda = 5$ and $n_p = 3$.

0.0 in the He I, Mg IX and Mg IX lines indicate that there is not always an event identified in these wavelengths. All maximum peak factors are, however, well over the $n_\lambda = 5$ criteria, implying that all wavelengths have a high enough intensity and sufficient variability to identify the blinkers. The absence of any signature of an event in the helium or magnesium lines is, therefore, probably real and suggests that blinkers are likely to be caused by something that happens in the transition region, rather than blinkers being the transition regions response to events in either the chromosphere or corona.

3.4 Line ratios

It has been well established (Chapter2, Harrison et al., 1999) that the intensity increases of QS blinkers are due to enhancements in either density or filling factor rather than temperature. Clearly, this fact also needs to be established for the blinkers seen in active regions to check they really are the same type of phenomenon. To do this we look at the line ratios of the oxygen light curves.

Figure 3.3 (a) shows the light curve of the O V blinker seen in Figure 3.2 (d). The line ratios of the O V line with the He I, O III and O IV lines are also shown in Figure 3.3 (b) - (d), respectively. The *dashed* line marks the time of the peak of the O V blinker. In this case, it appears as if the line ratios of the oxygen species dip around the time of the blinker, although the dips are only slight and within the error bars. If these dips are real then it would imply that

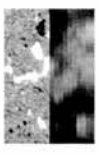

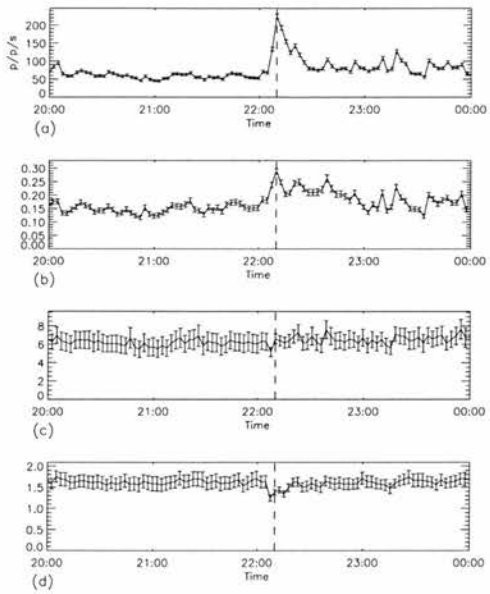

Figure 3.3: (a) O V blinker light curve, (b) O V/He I line ratio, (c) O V/O III line ratio and (d) O V/O IV line ratio. The *dashed* line indicates the peak of the O V blinker.

active-region blinkers are slightly cooler events than their surroundings.

To determine the significance of these dips and to test whether these dips are a common feature in AR blinkers we investigate the variability of the line ratios. We do this by calculating the minimum, mean and maximum values of the light curves between the start and end of the blinker and also over the entire light curve (Table 3.4). If the differences between the entire light curve ratio and blinker light curve ratio values are larger than the typical error bars expected then the change is considered significant.

Wavelength	Minimum		Mean		Maximum	
	Entire	Blinker	Entire	Blinker	Entire	Blinker
O V/O III	3.74	3.60	8.37	8.77	36.88	39.24
O V/O IV	1.16	1.09	1.66	1.64	3.68	3.67

Table 3.4: Minimum, mean and maximum line ratio values for the entire light curve and for the blinker region only.

From the results in Table 3.4 it appears as if there is little variation in the oxygen species between the entire and the blinker light curve ratios, even though the maximum, mean and minimum

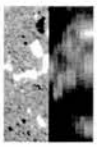

values are themselves quite different. The typical errors on the ratios of the O V/O III and O V/O IV are 1.32 and 0.14, respectively, however, the difference between the entire and blinker line ratios are always less than these errors except in the case of the maximum line ratio values for O V/O IV. We, therefore, conclude that these ratios are again effectively flat and thus AR blinkers are enhancements in either density or filling factor just like the QS blinkers.

3.5 Relationship to active-region emission

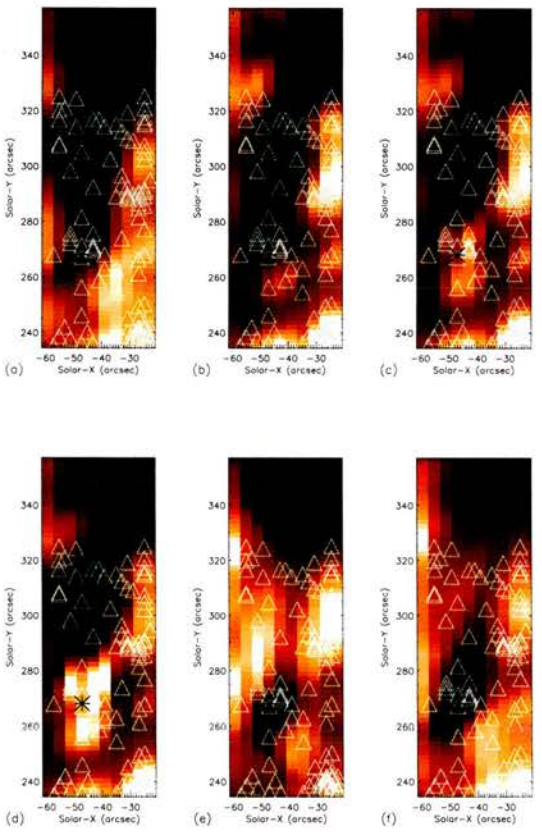

Figure 3.4: Comparison of the location of blinkers with the active-region network. Time integrated emission of the derotated (a) He I, (b) O III, (c) O IV, (d) O IV, (e) Mg IX and (f) Mg X rasters. Each △ identifies the location of a blinker and the ∗ refers to the blinker shown in Figure 3.2 (d).

It has been found that QS blinkers preferentially occur above quiet-Sun network regions. Indeed, in Chapter 2, it was found that no QS blinkers occurred in the bottom 5-10% of the intensity

range in He I, O III, O IV, and O V. It is interesting to test to see if this is still the case for AR blinkers.

Figure 3.4 shows the emission integrated over time from each of the six CDS wavelengths, with the location of the blinker midpoints plotted as $\triangle$s. The $*$ marks the blinker seen in Figure 3.2 (d). Clearly, the spatial distribution of the blinkers is not uniform, however, as in the QS case, we test to see if the distribution of blinkers with respect to intensity in the different wavelengths is uniform. To do this we use a likelihood statistical test as in Section 2.6. We calculate the likelihood ratio statistic, w_k using Equation 2.1 and compare it with the expected χ^2_{k-1} statistic. If w_k is large compared to χ^2_{k-1} then the distribution is not uniformly distributed with respect to intensity and suggests that the location of the blinkers is dependent on brightness of emission.

Wavelength	k	χ^2_{k-1}	Likelihood ratio statistic
HeI	7	24.10	2911.26
OIII	8	26.02	5132.24
OIV	9	27.87	5809.47
MgIX	6	22.11	1431.46
MgX	6	22.11	3114.04

Table 3.5: The likelihood ratio statistic and corresponding χ^2_{k-1} values calculated from a test to determine whether active-region O V $n_\lambda = 5$, $n_p = 3$ blinkers are uniformly distributed with respect to intensity.

The results from these tests are shown in Table 3.5 for the $n_\lambda = 5$, $n_p = 3$ blinkers. The blinkers are clearly not uniformly distributed with respect to the intensity of the pixels - the likelihood ratio statistic is between 65 and 210 times greater than the expected χ^2 statistic.

Figure 3.5 shows the distribution of intensity of CDS pixels in all wavelengths and AR blinkers (identified with $n_\lambda = 5$ and $n_p = 3$) at the time of the peak of the blinker. The *solid* line shows the distribution of pixels associated with the blinkers and the *dashed* line shows the distribution of all pixels. Figure 3.5 shows that for all wavelengths the blinker pixels are distributed such that they are not associated with low intensity pixels. This suggests that the blinkers are preferentially located over regions of strong emission for all wavelengths including coronal ones.

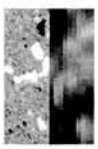

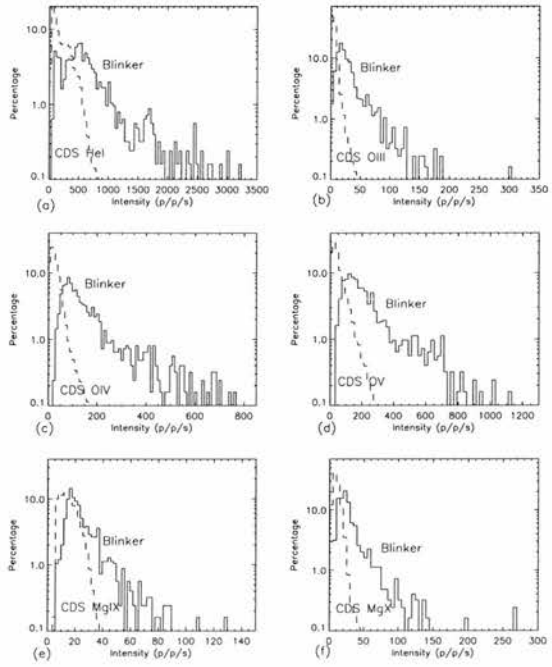

Figure 3.5: Histograms showing the distribution of intensity in the whole data set (*dashed*) and in the blinkers (*solid*) for (a) He I, (b) O III, (c) O IV, (d) O V, (e) Mg IX and (f) Mg X lines, respectively.

3.6 Conclusions

We have identified events in an active region that have the same characteristics as QS blinkers (Chapter 2) and have named these events 'active-region blinkers'. Two similar events had previously been found by Walsh et al. (1997), but little was known about these events in general. We have found that AR blinkers have mean lifetimes between 16.5 and 19.3 minutes, mean areas between 2.4×10^7 and 4.3×10^7 km^2 and mean intensity enhancement factors between 1.8 and 3.3. They are more abundant than QS blinkers and have a global frequency between 7 and 28 s^{-1}. These characteristics suggest that AR blinkers are a little larger and slightly more intense than QS blinkers, but have approximately the same lifetimes. Furthermore, our results suggest that, like QS blinkers, AR blinkers are enhancements in density or filling factor and are not temperature events.

In all wavelengths the light curves of the blinkers are very similar. Indeed, approximately 5-10% of the AR blinkers show peaks in both the coronal lines (Mg IX and Mg X) that are significant

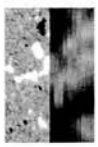

enough to count as blinkers. The presence of these coronal blinkers is the most significant difference between AR and QS blinkers. It is possible that these signatures are only visible because the counts in the coronal lines are much higher in an active region than in the quiet Sun. Even if the peaks in the coronal lines are not significant enough to be blinkers they are still indicating that an event has occurred.

We have shown that blinkers are located over the regions with the strongest emission from all lines, chromospheric, transition region and coronal. This suggests that blinkers occur above sites of active-region network and plage regions.

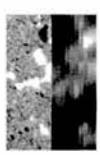

Chapter 4

Velocities of Blinkers

In this Chapter, we use the spectral capabilities of the CDS instrument to try and determine the velocities of the plasma within blinkers. We compare the velocities of blinkers with those found for the entire transition region and chromosphere in this study, and from previous studies by a number of authors. In Section 4.1 we review the velocities found in the chromosphere and transition region over the last few decades using different instruments. The data and method of analysis is presented in Section 4.2 with further details given in Appendix B. In Section 4.3 we describe the velocities found and in Section 4.5 we make our concluding remarks. In this Chapter we only investigate the plasma velocities relating to blinkers identified with BLIP in O V using $n_\lambda = 5$ and $n_p = 3$. We also investigate the chromospheric He I plasma velocities directly below these blinkers. Analysis of the velocity within blinkers is essential if we are to understand the mechanism that causes blinkers, and may lead us to determine which mechanism is at work. Discussion on how our results effect possible blinker mechanisms is left until Chapter 7.

4.1 Velocities in the chromosphere and transition region

Much work has been carried out to determine the velocities of transition-region plasmas. Using Skylab data, Doschek et al. (1976) discovered red-shifted quiet-Sun plasma in a variety of emission lines, including Si IV, C IV, O IV, N V and O V formed at temperatures of 7.1×10^4 K, 8.9×10^4 K, 1.3×10^5 K, 1.8×10^5 K and 2.2×10^5 K, respectively. The observed shifts implied

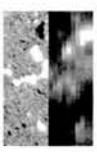

velocities of 15 km s^{-1} or less.

The High Resolution Telescope and Spectrograph (HRTS) was used by Achour et al. (1995) to show that transition region plasma is red-shifted up to a temperature of 1.35×10^5 K in both quiet-Sun and active regions using a number of lines whose temperatures of formation ranged from 1×10^4 K to 1.4×10^6 K. The peak velocities were found to be 11 km s^{-1} in the quiet-Sun and 18 km s^{-1} in active regions. Above this temperature, they find that the velocity decreases with increasing temperature for the transition region and coronal O V, N V and Fe XII lines.

More recently, the Solar Ultraviolet Measurements of Emitted Radiation (SUMER) instrument on SOHO has been used to calculate plasma velocities in the transition region. Chae et al. (1998b) used twelve lines which had temperatures of formation that ranged from $10^4 - 10^6$ K and found that the average Doppler shift at the base of the transition region was 1 - 2 km s^{-1}. They also found that the observed Doppler shifts increased with temperature peaking at 11 km s^{-1} near a temperature of 2.3×10^5 K. The average velocity then decreases, but still remained above zero, as the temperature increased still further. Chae et al. (1998b) interpret this as evidence of plasma flowing from the corona down into the transition region.

Further work, using SUMER, has shown evidence for blue-shifted plasma in the upper transition region. Teriaca et al. (1999) found that the velocities of red-shifted material increased from 0 km s^{-1} at 2×10^4 K, to 10 km s^{-1} at 1.9×10^5 K, but then decreased and became blue shifted (-2 km s^{-1}) at 6.3×10^5 K. Dammasch et al. (1999) also found blue shifted plasma (-1 ± 1 km s^{-1}) at a temperature of 6.3×10^5 K. Peter and Judge (1999), however, found that plasma changed from being mostly red shifted to blue-shifted at a lower temperature of 5×10^5 K.

By looking at the different parts of the quiet Sun and comparing network and intranetwork regions, Hansteen et al. (2000) found that transition region lines are, on average, red shifted with plasma velocities of 5 - 10 km s^{-1} in the network and < 4 km s^{-1} in intranetwork regions. They also found a correlation between the mean red shift and the mean intensity in the network, but no such correlation was found in intranetwork regions.

Analysis of plasma velocities in active regions have shown similar results to those in the quiet Sun. Feldman et al. (1982) found only red shifts at active transition-region temperatures with velocities ranging from 4 - 127 km s^{-1}, with the largest shifts at temperatures of 5×10^4 - 10^5 K. Dere (1982) used twelve emission lines with temperatures of formation that ranged between 10^4

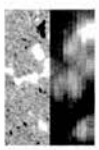

K and 10^6 K, and found downflows with a magnitude of 10 km s^{-1} throughout plage regions, whilst above the umbra of sunspots he found velocities of 5 - 20 km s^{-1}. No velocities, however, were found over the penumbra. He also found that the velocities peaked at a temperature of 10^5 K, with lower velocities found at both higher and lower temperatures. Mariska and Dowdy (1992), however, observed velocities of up to 70 km s^{-1} in an active region with the Ne VII emission line formed at 5×10^5 K. More recently using SUMER, Teriaca et al. (1999) found an average velocity of 19 km s^{-1} at 10^5 K in an active region, which then changed to a blue shift of -8 km s^{-1} at a temperature of 6.3×10^5 K and -10 km s^{-1} at 10^6 K in the corona. Brynildsen et al. (1998), however, suggest that the active transition region is generally red-shifted at a temperature of 6.5×10^5 K.

In general, therefore, the plasma in the chromosphere and transition region appears to be typically red shifted with a peak velocity of about 10 km s^{-1} in the quiet Sun and 20 km s^{-1} in active regions at a temperature of 2×10^5 K, and blue shifted at higher temperatures of about 5×10^5 K.

Non-thermal velocities have also been found using a variety of satellite data. Mariska et al. (1978) using Skylab, found that non-thermal transition-region velocities increase with temperature. They quote a velocities of 0 km s^{-1} at 10^4 K, rising to 22 km s^{-1} at 2.2×10^5 K. Dere and Mason (1993) used HRTS data and found peak non-thermal velocities of 17 km s^{-1} and 27 km s^{-1} at a temperature of 10^5 K for quiet-Sun and active regions, respectively. They also found that the quiet Sun had a wider distribution of velocities than active regions.

More recently, using SOHO/SUMER, Chae et al. (1998a) found non-thermal velocities of <10 km s^{-1} at temperatures of $\leq 2 \times 10^4$ K. They also found that these velocities increased with temperature, peaking at about 30 km s^{-1} at a temperature of 3×10^5 K. A strong correlation was found between intensity and non-thermal velocity of plasma with temperatures between 2×10^4 - 1×10^5 K. Hansteen et al. (2000) determined that the line widths of C II and O VI lines do not vary much between the network and internetwork regions and increase with increasing temperature of line formation from 30 km s^{-1} at 10^5 K to 45 km s^{-1} at 3.2×10^5 K.

In general, therefore, it appears that non-thermal velocities increase with increasing temperature, from 0 km s^{-1} at 10^4 K to 20 - 30 km s^{-1} at a few times 10^5 K.

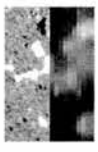

4.2 Data and analysis

In this Chapter, we use two data sets taken by the SOHO/CDS instrument. Both data sets used have the same properties as the data analysed in Chapter 2, i.e. they contain 6 emission lines (He I, O III, O IV, O V, Mg IX and Mg X), they cover areas of $40'' \times 124''$ with pixels of size $4'' \times 1.6''$, they have exposure time of 15 seconds and the cadence of the rasters are approximately 151 seconds. Only the He I and O V emission lines are suitable for analysis since, they are the only lines with sufficient counts to produce good spectral profiles and are not blended. The spectral resolution of the data is 0.12 Å.

We have chosen to analyse two pre-recovery data sets, (i.e. data taken before the loss of SOHO on 25th June 1998) since the line profiles are essentially Gaussian and are more reliable and easier to use for velocity analysis. For this reason, the quiet Sun data are not the same as that analysed in Chapter 2, but were taken on 19th June 1998; the region analysed can be seen in Figure 4.1. The start of the observation run was 12:30 UT and it lasted almost 8 hours; there were 180 rasters taken. The coordinates of the centre of the first raster are $221.7''$ E and $246.4''$ N. The active-region data (Figure 3.1) are the same as that analysed in Chapter 3. The data were prepared using the same methods as those described in Section 2.1.

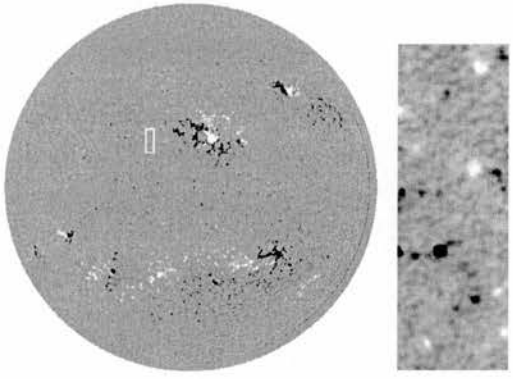

Figure 4.1: Full disk magnetogram taken on 19th June 1998 at 12.48 UT showing the location of the quiet-Sun data analysed. The white box indicates the area covered by the CDS rasters investigated. The partial frame high resolution MDI magnetogram shows the magnetic field below the CDS rasters in more detail.

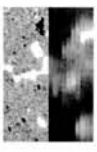

4.3 Results

4.3.1 All pixels

We investigate the velocity of all the pixels in both the quiet-Sun (QS) and active region (AR) He I and O V data sets. We fit the spectra of each spatial pixel in the dataset with a Gaussian function and calculate the relative Doppler and non-thermal (NT) velocities with respect to a time-dependent reference line centre position and width. The reference line centre and width only enable us to determine the velocities of the pixels relative to the typical Doppler and NT velocities, but not their absolute velocities. This is because for the CDS instrument it is not possible to perform a wavelength calibration, since CDS is is flown on board the SOHO spacecraft and therefore the spectra are affected by the flexing of the instrument, thermal changes, etc. The reference line centre position and width are the modal line centre and modal width values of each raster and vary with time. More details can be found in Appendix B.

Quiet Sun

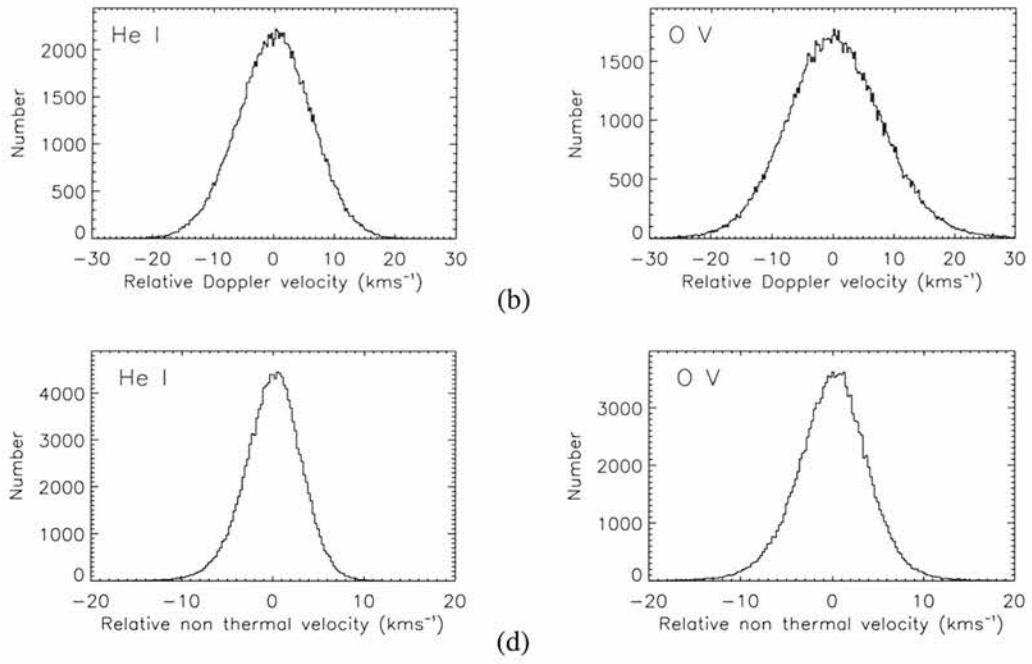

Figure 4.2: Distribution of QS velocities. (a) He I Doppler velocity, (b) O V Doppler velocity, (c) He I NT velocity and (d) O V NT velocity. The bin size in all plots is equal to 0.25 km s^{-1}.

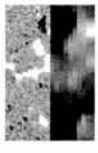

First, we consider the distribution of the relative velocities in all the QS pixels. Figure 4.2 shows the distribution of relative Doppler and NT velocities for all the pixels in the QS data set for both He I and O V. In all cases, the distributions look to be essentially Gaussian suggesting that they may be completely dominated by noise. To test to see if this is true, we test for normality using the Bowman & Shenton normality test (D'Agostino and Stephens, 1986), which is detailed below.

A random sample of n velocities, $x_1, \ldots, x_n$, has a mean, m_1 which is given by

$$m_1 = \sum_{j=1}^{n} \frac{x_j}{n} , \tag{4.1}$$

and central moments, m_i, which are given by

$$m_i = \sum_{j=1}^{n} \frac{(x_j - m_1)^i}{n} , \qquad i = 2, 3, 4. \tag{4.2}$$

The sample skewness ($\sqrt{b_1}$) and kurtosis (b_2) are given, respectively, by

$$\sqrt{b_1} = \frac{m_3}{(m_2)^{1.5}} , \tag{4.3}$$

$$b_2 = \frac{m_4}{(m_2)^2} . \tag{4.4}$$

The values of the skewness and the kurtosis are then compared to the contour graph shown in Figure 4.3 to determine whether the velocities are normally distributed. If the distribution is perfectly normal then $\sqrt{b_1} = 0$ and $b_2 = 3$. Note, that $\sqrt{b_1}$ can be either positive or negative, since m_3 may be greater or less than zero, and for $\sqrt{b_1} < 0$ the contours are simply a mirror image of those for $\sqrt{b_1} > 0$, shown in Figure 4.3.

From this test, it is only the QS He I Doppler velocities that we can accept with a 90% confidence that the distribution is normal. In all other cases, we are considerably less than 90% sure of this hypothesis, indeed it is quite possible these distributions are not normal. Thus, we can consider the distributions to be composed of a normal and a non-normal component, where the non-normal component will show up as wings on the distributions. The normal component of the distribution is comprised of the Poisson noise which gives a spread about the typical velocities. To determine the noise of the velocities we fit a normal distribution to our samples. The full width of the fit, i.e. twice the square root of the variance, represents the 2σ noise associated with the velocities in the data set. The non-normality of the Doppler and NT velocity distributions,

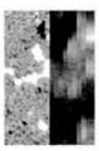

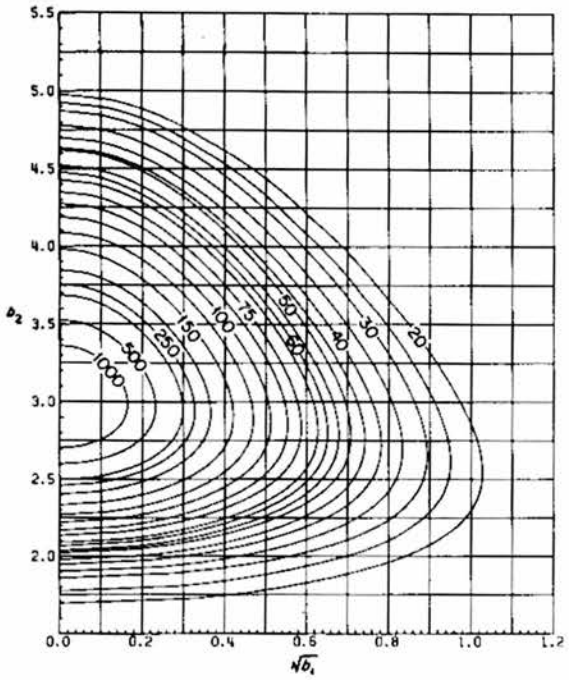

Figure 4.3: 90% contours for Bowman & Shenton normality test (D'Agostino and Stephens, 1986).

suggests that there are some pixels with velocities that are above the noise, but the majority of pixels have velocities that are within the noise of the data. For the NT velocity distributions, only a wing on the right-hand-side suggests the presence of broadenings greater than the noise of the data. A wing on the left-hand-side suggests that some pixels have a narrower width that is typical for that wavelength and region, i.e. it may suggest that these pixels have zero NT velocity.

For all the QS pixels, the 2σ noise is calculated as 11.0 and 14.0 km s^{-1} for the He I and O V Doppler velocities, respectively, and 5.4 and 6.6 km s^{-1} for the He I and O V NT velocities, respectively. The approximate ranges of the QS Doppler velocities are ± 20 and ± 30 km s^{-1} for He I and O V, respectively, and the ranges of the NT velocities are ± 10 and ± 15 km s^{-1} for He I and O V, respectively. As expected, the spread of both O V Doppler and NT velocities is greater than the spread of the He I Doppler and NT velocities, since the O V line is formed at a higher temperature than the He I line and the typical background O V Doppler and NT velocities quoted in the literature are higher than the those quoted for He I.

To compare the distribution of the velocities greater than and less than the typical value, we look at plots of the percentage of pixels that have unsigned velocity less than v, where v is given on

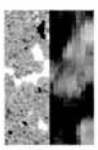

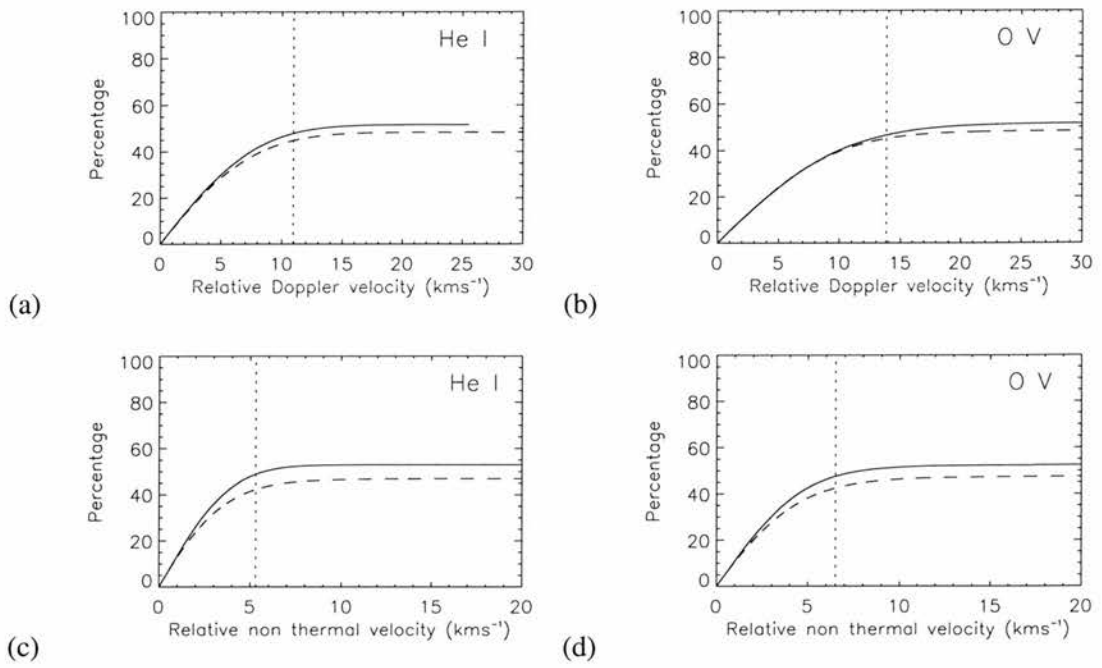

Figure 4.4: Percentage of all QS pixels with unsigned relative Doppler or NT velocities less than the value on the x-axis. (a) and (b) show the relative Doppler velocities for He I and O V pixels, respectively. (b) and (d) show the relative NT velocities for He I and O V pixels, respectively. The *solid* and *dashed* lines represent the pixels with velocities that are greater than and less than the typical value, respectively. The *dotted* lines indicate the noise levels on all the QS pixel velocities.

the x-axis (Figure 4.4). In Figure 4.4 (a) and (b) the relative Doppler velocities for the He I pixels and the O V pixels are shown and in Figure 4.4 (c) and (d) the relative NT velocities for the He I pixels and the O V pixels are plotted. The *solid* and *dashed* lines in each graph represent the pixels that have velocities greater than and less than the typical velocity, respectively. The *dotted* line indicates the noise associated with all the QS pixel velocities.

In all cases, there are approximately 5 - 10% more QS pixels that have Doppler and NT velocities greater than the typical value rather than less than this value. Chae et al. (1998b) quote typical Doppler velocity values in the chromosphere and the transition region as 1 - 2 and 11 km s^{-1}, respectively. Our results show that these Doppler velocites can be as high as 22 ± 11 km s^{-1} and 40 ± 14 km s^{-1} for He I and O V, respectively, although they may also be as low as -18 ± 11 km s^{-1} and -20 ± 14 km s^{-1}, respectively. The typical NT velocities quoted for the chromosphere and transition region given by Chae et al. (1998a) and Mariska et al. (1978) are

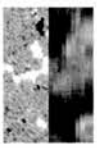

0 km s^{-1} and 20 km s^{-1}, respectively. We find, therefore, that these NT velocities can reach as high as 10 ± 6 km s^{-1} and 35 ± 7 km s^{-1} for He I and O V, repsectively.

Active Region

Next we consider the distributions of all the AR pixels. Again, we test for normality of the velocity distributions and find that none of the AR velocity distributions are normal. We also calculate the noise associated with the velocities by determining the full widths of Gaussians fitted to the velocity distributions. The noise is found to be 10.8 and 15.0 km s^{-1} for the He I and O V Doppler velocities, respectively, and 4.4 and 5.8 km s^{-1} for the He I and O V NT velocities, respectively.

The approximate range of the Doppler velocities in He I and O V are ± 20 and ± 35 km s^{-1}, respectively, and the range of NT velocities are ± 10 and ± 15 km s^{-1} for He I and O V, respectively. As in the QS data, the spread of AR Doppler and NT velocities is greater in the transition region O V line than in the chromospheric He I line. The range of the O V Doppler velocities is slightly greater in the AR than in the QS, suggesting that the Doppler velocities in the AR are higher than in the QS.

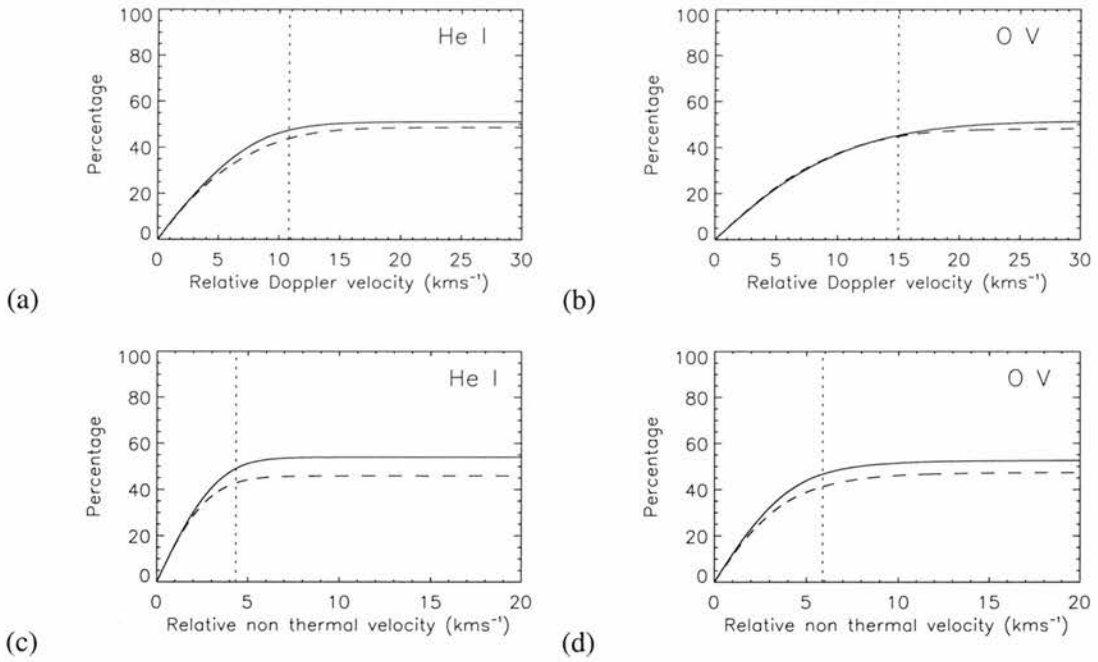

Figure 4.5: As for Figure 4.4 but for all the AR pixels.

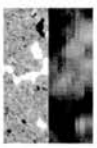

Figure 4.5 shows the percentage of all the AR pixels that have velocities less than the value on the x-axis. Figure 4.5 shows the relative Doppler and NT velocity of the He I pixels in graphs (a) and (c), respectively and the O V pixels in graphs (b) and (d), respectively. The *solid* and *dashed* lines represent the pixels that have velocities that are greater than and less than the typical value, respectively. The *dotted* lines mark the noise levels calculated from all the AR velocities.

As in the QS case, there are $\approx 5\%$ more pixels with velocities greater than the typical value rather than less than this value. The typical AR Doppler velocities for the chromosphere and transition region given by Dere (1982) and Teriaca et al. (1999) are 10 and 20 km s^{-1}, respectively. Our results show that these Doppler velocities may vary between -10 ± 11 and 30 ± 10.8 for He I and between -15 ± 15 and 55 ± 15.0 km s^{-1} for O V. The observed typical NT velocities are not quoted in the literature as varying from QS to AR, so our findings indicate that the AR NT velocities range up to 10 ± 5 and 25 ± 6 km s^{-1} for He I and O V, respectively.

4.3.2 Blinker pixels

Next we consider just the O V pixels that comprise the blinkers for the duration of the blinker only and the He I pixels in the corresponding position. This enables us to determine how the velocities of plasma within blinkers compares with the plasma in the whole of the chromosphere and transition region.

Quiet Sun

As in the previous sections, we test the He I and O V Doppler and NT relative velocity distributions for normality and calculate the noise associated with the data in the same way as above. As before, in all cases, except that of the He I Doppler velocities, we find that all the velocity distributions are not normal. The calculated values of the 2σ noise associated with the data are 11.6 and 13.0 km s^{-1} for the He I and O V Doppler velocities, respectively, and 4.6 and 5.4 km s^{-1} for the He I and O V NT velocities, respectively. Since by definition, the blinker pixels are the brighter pixels and, therefore, have a higher signal to noise, the noise on the velocities has been slightly reduced for this subset of the data. The range of the QS Doppler velocities are ± 20 and ± 30 km s^{-1} for the He I and O V, respectively and ± 10 and ± 15 km $s^{-1}$for the He I and O V NT velocities, respectively.

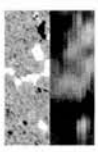

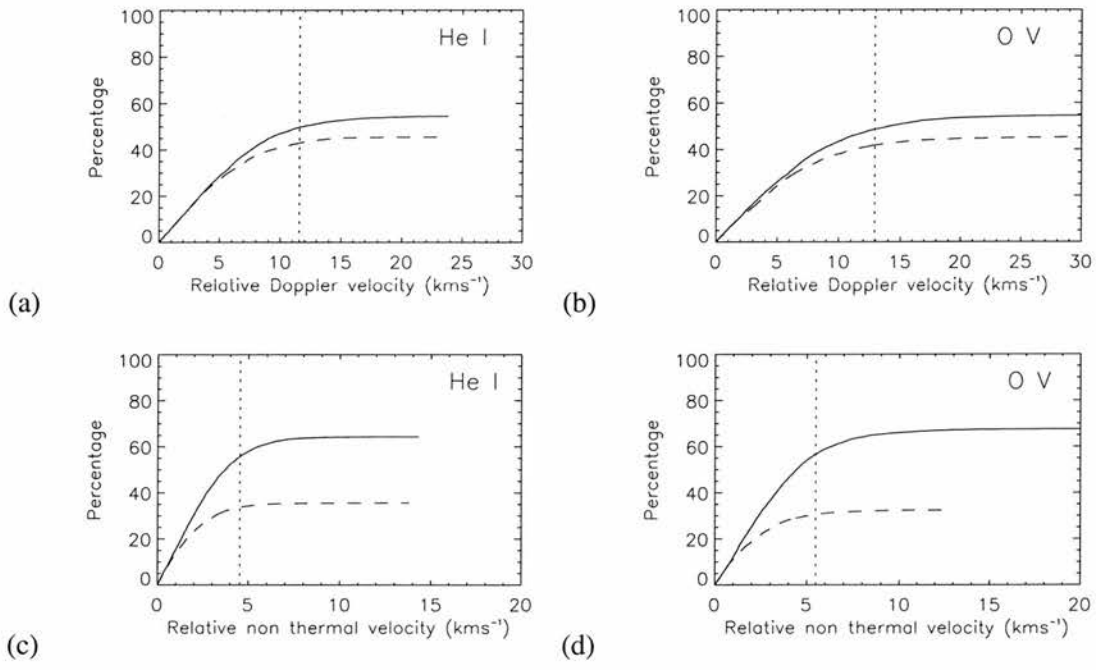

Figure 4.6: As for Figure 4.4 but for QS blinker pixels for the lifetime of the blinker.

Again we investigate the asymmetry of the distribution of the relative velocities. Figure 4.6 shows the percentage of QS blinker pixels that have unsigned relative velocities less than the value on the x-axis. In Figure 4.6 (a) and (b) the relative Doppler velocities for the He I blinker pixels and the O V blinker pixels are considered, whereas, Figure 4.6 (c) and (d) show the relative NT velocity of the He I blinker pixels and the O V blinker pixels, respectively. The *solid* lines show those pixels that have velocities greater than the typical values and the *dashed* lines show those pixels that have velocities less than the typical values.

For the blinkers, there are 10% more He I and O V blinker pixels that have Doppler velocities greater than the typical value than have less than this value. This is double the imbalance seen when all the pixels were considered. As has already been discussed, the typical Doppler velocities in the chromosphere and transition regions are 1 - 2 km s^{-1} and 11 km s^{-1}, respectively. This suggests that there is a slightly higher than normal tendancy for blinker pixels to have velocities larger than these values. The majority of these Doppler velocities have speeds up to 20 ± 12 km s^{-1} and 40 ± 13 km s^{-1} for He I and O V, repsectively. Some of the blinker pixels may be blue-shifted, but most of these travel at speeds less than 15 ± 12 km s^{-1} and 20 ± 13 km s^{-1} for the He I and O V, respectively.

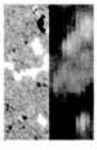

As expected, there are more blinker pixels that have NT velocities greater than the typical value, but the ratio of those greater than and less than the typical for the blinker pixels is significantly larger than for all the pixels. As previously stated, the typical NT velocities for the QS chromosphere and transition region are 0 km $s^{-1}$and 20 km s^{-1}, respectively. This means that most blinker pixels have NT velocities of up to 10 ± 5 km s^{-1} and 35 ± 6 km s^{-1} for He I and O V, respectively. These velocities are within the range of all the pixels NT velocities, but 25% and 30% more of the blinker pixels have velocities greater than 0 and 20 km s^{-1}, respectively for He I and O V, compared to just 10% for all the pixels.

Active Region

For the AR, we similarly test the He I and O V Doppler and NT velocity distributions for normality and calculate the 2σ noise associated with the AR blinker velocities. As for all the AR pixels, we find that none of the velocity distributions are normal. The 2σ noise associated with the blinker pixels is calculated to be 11.8 and 16.4 km s^{-1} for the He I and O V Doppler velocities, respectively, and 4.4 and 5.8 km s^{-1} for the He I and O V NT velocities, respectively. These values of noise are reduced compared to the whole of the data set for the same reasons given for the QS blinkers. The range of the AR Doppler velocities span ± 20 and ± 35 for He I and O V, respectively, and the NT velocities span ± 10 and ± 15 km $s^{-1}$for He I and O V, respectively.

Figure 4.7 shows the percentage of AR blinker pixels that have unsigned relative velocities less than the value on the x-axis for the Doppler velocities of the He I blinker pixels and the O V blinker pixels (graphs (a) and (b)) and also the NT velocities of the He I blinker pixels and the O V blinker pixels (graphs (c) and (d)). The *solid* and *dashed* lines represent the AR blinker pixels that have velocities greater than and less than the typical value, respectively. The *dotted* lines mark the 2σ noise associated with the blinker velocities.

As with the AR blinker pixels, there are (up to 30%) more blinker pixels that have Doppler and NT velocities greater than the typical value than less than this value. Taking the typical AR Doppler velocities of 10 and 20 km s^{-1} for the chromosphere and the transition region, our results show that the majority of AR blinker velocities vary between -10 ± 12 and 30 ± 12 for He I and between 0 ± 16 km s^{-1} and 40 ± 16 km s^{-1} for O V. Then taking the typical AR NT blinker pixel velocities of 0 and 20 km s^{-1} for the chromosphere and transition region,

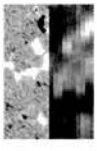

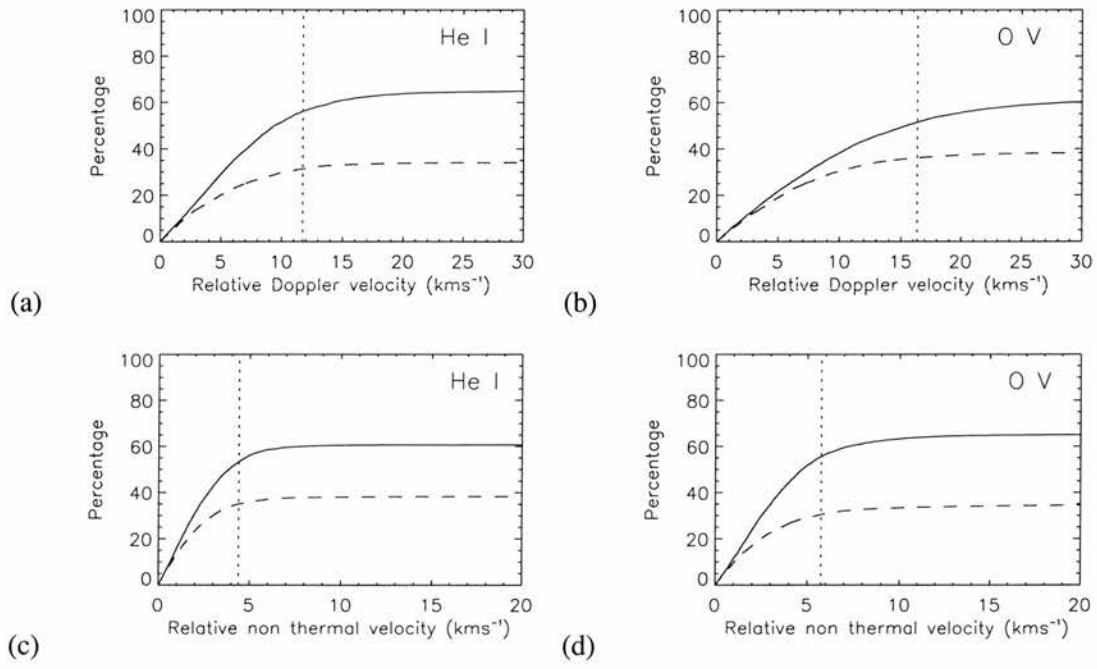

Figure 4.7: As for Figure 4.4 but for AR blinker pixels for the lifetime of the blinkers.

repsectively, our results suggest that the He I NT velocities are less than 20 ± 4 km s^{-1} and the O V NT velocities are less than 30 ± 6 km s^{-1}.

4.3.3 Blinkers

Next we consider the O V spectra of the whole blinker for the whole of its lifetime and the He I spectra for the corresponding position. We sum the spectra of the pixels that make up the blinker to make a single spectra for the whole blinker which we fit with a Gaussian function. From these, the relative Doppler and NT velocities can be calculated for the whole blinker at each step in time.

Quiet Sun

Histograms showing the distribution of the relative He I and O V Doppler and NT velocities of the whole blinker for the lifetime of the blinkers only are plotted in Figure 4.8. Again, we test to determine whether the velocity distributions are normally distributed and find that none of them are. The 2σ noise associated with the whole blinker velocities are calculated by fitting Gaussians

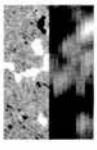

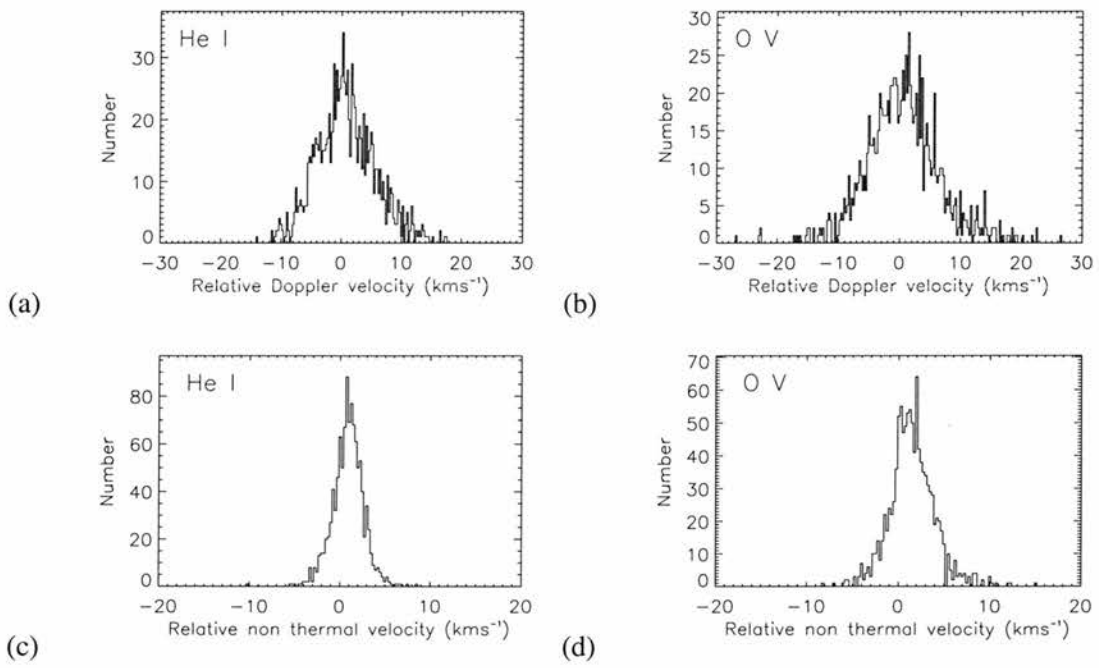

Figure 4.8: As for Figure 4.2 but for the grouped spectra of the QS blinkers for their lifetime only.

to the histograms and are found to be 8.2 and 9.2 km s^{-1} for both the He I and O V Doppler velocities and 2.6 and 3.6 km s^{-1} for the He I and O V NT velocities. The noise on the whole blinker velocities is much lower than the noise on the individual pixels because we are summing at least 3 spectra and so significantly increasing the ratio of signal to noise.

Figure 4.9 shows the percentage of the relative velocities that are less than the value on the x-axis. As in all cases, the *solid* and *dashed* lines represent the relative velocities greater than and less than the typical values, respectively. The *dotted* lines mark the noise associated with the velocities.

Again, in all cases for the QS blinkers we see that there are more velocities with speeds greater than the typical value than less than this value; 15% more of the He I Doppler velocities and 10% of the O V Doppler velocities have velocity greater than the typical value. The typical Doppler velocity values are roughly 0 and 10 km s^{-1} in the chromosphere and transition region, thus the majority of blinkers should have velocities between $10 - 20$ km s^{-1} ± 8 km s^{-1} and $15 - 35$ km s^{-1} ± 9 km s^{-1} for He I and O V, respectively. Even more significant is the number of NT velocities higher than the typical value, with 50% more He I and 55% more O V blinkers with

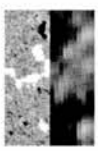

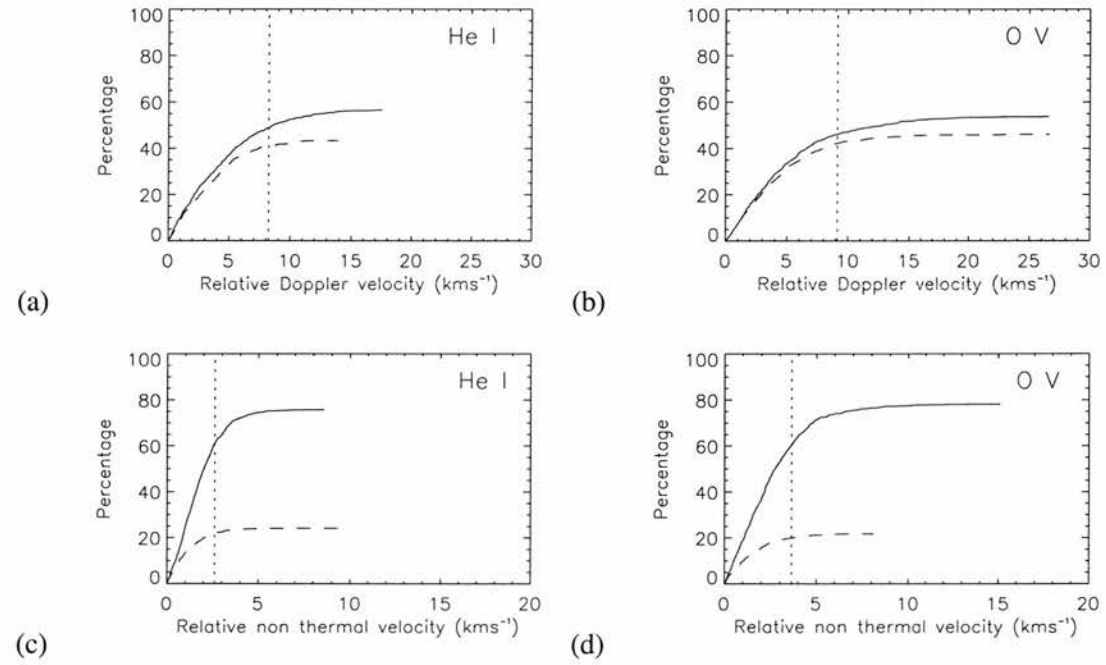

Figure 4.9: As for Figure 4.2 but for the grouped spectra of the QS blinkers for their lifetime only.

NT velocities greater than typical, compared to less than typical. This means that most blinkers have broader velocity profiles than the rest of the chromsphere and transition region. Taking the typical NT velocities of the chromosphere and transition region to be 0 and 20 km s^{-1}, the majority of blinkers have NT velocities up to 5 ± 3 km s^{-1} and 30 ± 4 km s^{-1}, respectively, for He I and O V.

Active Region

Next we consider the velocities of the AR blinkers which are calculated in the same way as the QS blinker velocities. Figure 4.10 shows the distribution of relative velocities of the whole blinker for the whole of its lifetime. As previously, we determine whether the velocity distributions are normally distributed, and find that none of them are. We calculate the noise associated with the data to be 8.2 and 12.4 km s^{-1} for the He I and O V Doppler velocities and 2.6 and 4.2 km s^{-1} for the He I and O V NT velocities, respectively.

Figure 4.11 shows the percentage of the He I and O V Doppler and NT velocities that have relative velocity less than the value on the x-axis. The *solid* and *dashed* lines represent the

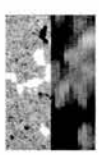

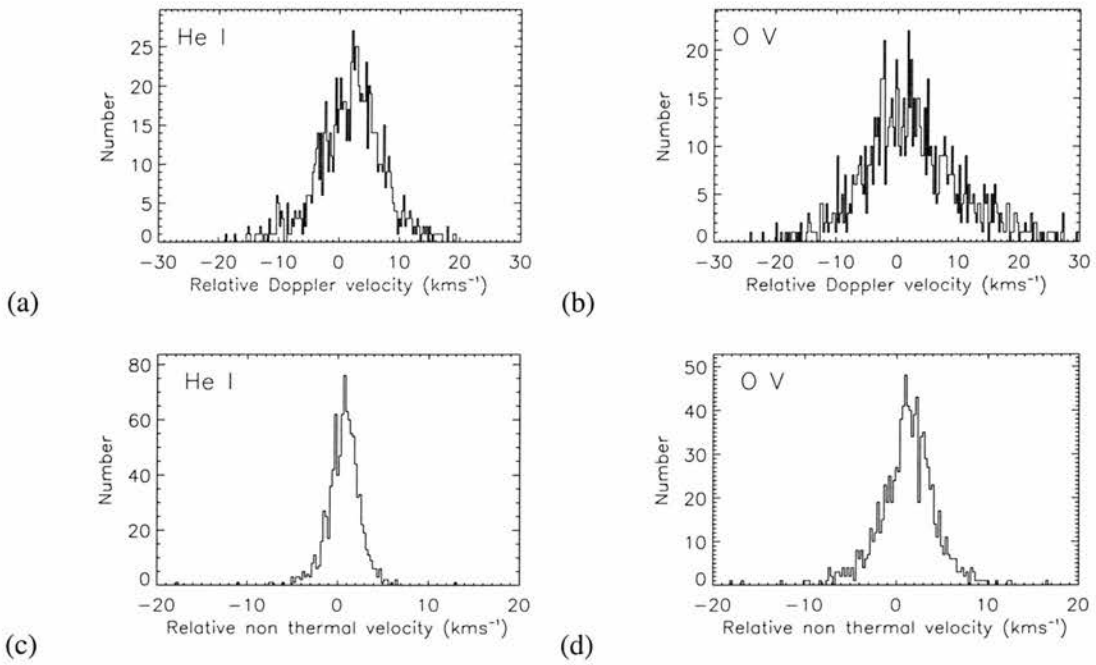

Figure 4.10: As for Figure 4.2 but for the grouped spectra of the AR blinkers for their lifetime only.

velocities greater than and less than the typical value, respectively. The *dotted* lines mark the noise associated with the AR blinker velocities.

In all cases, there is a significantly higher percentage of blinkers that have Doppler and NT velocities greater than the typical value rather than less than it. In the case of the He I Doppler velocities, the difference is 35% whereas for the O V Doppler velocities the increase is 20%. These values are larger than those found when all the pixels were considered all the pixels which was just 5%. Thus the majority of AR blinkers have red-shifts of up to 25 ± 8.2 km s^{-1} and 50 ± 12 km s^{-1} if we take the typical Doppler velocities in AR's to be 10 and 20 km s^{-1} for He I and O V, respectively. For both the He I and O V NT velocities, there are again significantly more blinkers with widths broader than the typical He I and O V width. Indeed, the number on the right of the distribution relative to the left is an increase of 40% and 45%, respectively for the He I and O V. These are about 8 and 9 times bigger than the imbalance seen for all the AR pixels in the chromosphere and transition region, respectively. This means that in general, the AR blinkers have larger NT velocities than the typical plasma with these velocities ranging up to 5 ± 3 km s^{-1} and 30 ± 4 km s^{-1} for the He I and O V, when taking typical values of 0 and

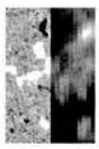

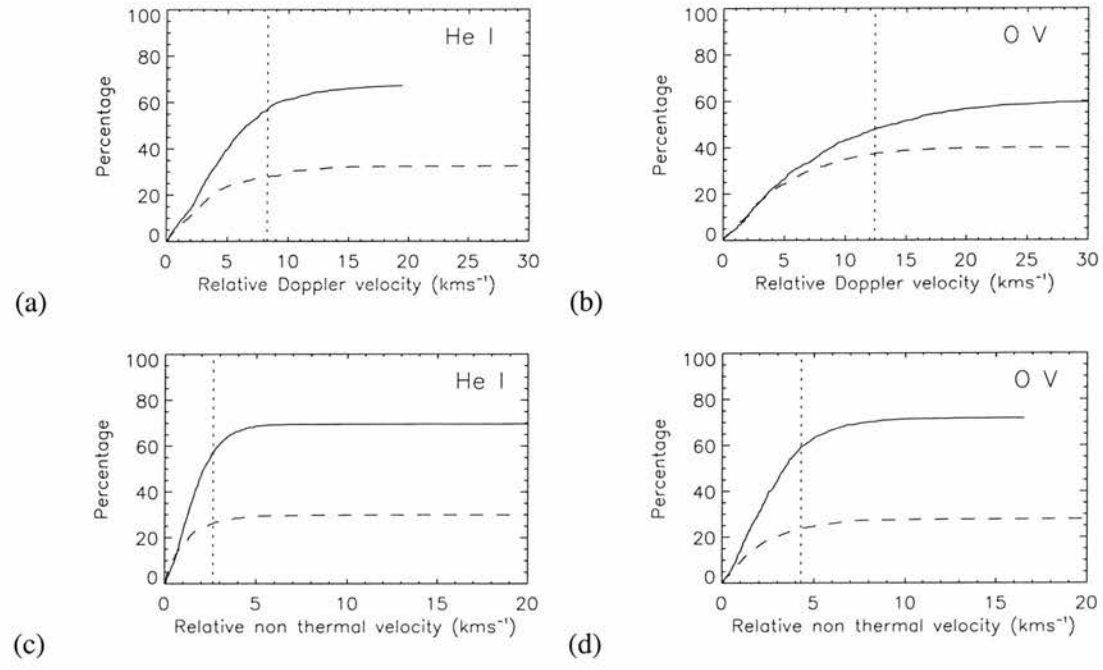

Figure 4.11: As for Figure 4.2 but for the grouped spectra of the AR blinkers for their lifetime only.

20 km s^{-1}.

4.4 Conclusions

In general, we have found that the majority of relative Doppler and NT velocity distributions are not normal. Thus the relative velocities may be preferentially higher or lower than the typical values.

When the whole of the data set is considered, we find that all the relative Doppler velocity distributions have a larger right-hand wing. This difference is only slight when the velocities of all the pixels are considered, however, when the blinker pixel velocities or the blinker velocities are considered this imbalance becomes more significant. Thus, in general, blinkers and the chromosphere directly below have a preference to be more red-shifted than the normal chromospheric and transition region plasma, although the range of these enhanced shifts are no larger than the typical spread of Doppler velocities in these regions. Furthermore, blinkers and the chromosphere directly below are also found to preferentially have larger NT velocities than the typical

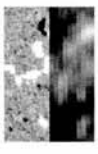

background chromosphere and transition region. Again the increase in magnitude of the NT velocity is no greater than the typical range of NT velocities, there are just more blinkers with these larger velocities than one would expect in comparison to the chromosphere and transition regions as a whole.

Thus we anticipate that QS blinkers have Doppler shifts of between 10 km s^{-1} and 20 km s^{-1} in He I and between 15 km s^{-1} and 35 km s^{-1} in O V and have NT velocities between 0 km s^{-1} and 5 km s^{-1} in He I and between 20 km s^{-1} and 30 km s^{-1} in O V. The AR blinkers show similar ranges of Doppler and NT velocities, but the Doppler velocities may range between 10 km s^{-1} and 25 km s^{-1} for He I and between 20 km s^{-1} and 55 km s^{-1} for O V.

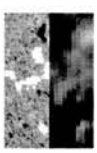

Chapter 5

Magnetic Structure of Blinkers

In this Chapter, we analyse the photospheric magnetic field beneath the quiet-Sun and active-region blinkers identified in Chapters 2 and 3. We only investigate those O V blinkers that have $n_\lambda = 5$ and $n_p = 3$. We compare the magnetic field strength (where only one polarity of field is present) and the ratio of minority to majority field (where both positive and negative field is present) to the area, lifetime and peak factor of blinkers. This analysis is crucial to understanding the mechanism that causes blinkers.

We use magnetogram and white light data from the SOHO/MDI instrument (described in Section 1.2.2) for the analysis in this Chapter. Figures 2.1 and 3.1 show the quiet Sun and active region investigated, respectively. As can be seen from the partial frame magnetograms in these Figures, both regions are dominated by positive polarity flux.

5.1 Data

The magnetogram and white light data used in this chapter are MDI high resolution data and have a cadence of 1 minute and pixels of size $0.6'' \times 0.6''$. The effect of the rotation of the Sun and cosmic ray hits are removed from the data. A correction is also used to convert the line-of-sight values of the magnetic field into radial values. We group the data into sets of 3 consecutive images and average these, thus reducing the cadence of the data to that of the CDS images, as well as reducing the noise in the MDI data.

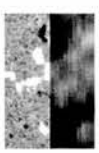

The MDI data is aligned to the CDS rasters using the pointing information given in the index structures of the data. This alignment is known to have a root mean square (rms) error of between $5''$ and $10''$, however, comparison of features in the two data sets suggests we have achieved an alignment that has an error of nearer $2'' - 3''$.

5.2 Quiet-Sun blinkers

5.2.1 Relationship to magnetic field

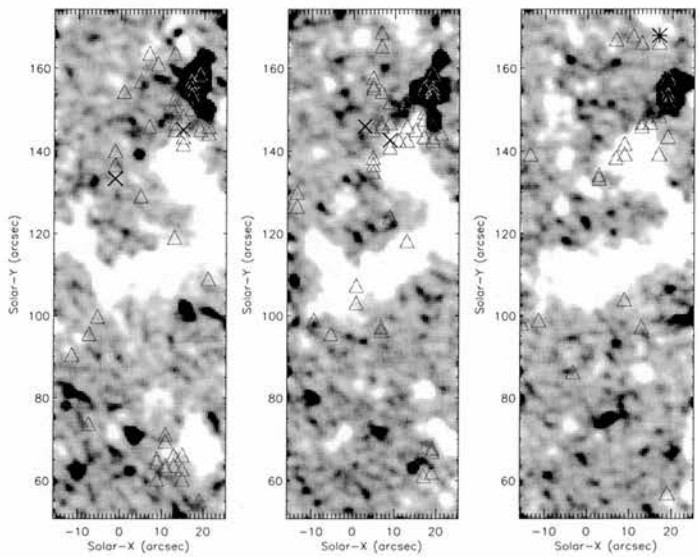

Figure 5.1: Comparison of the location of the midpoints of the $n_\lambda = 5$ and $n_p = 3$ blinkers ($\triangle$s) with the underlying magnetic field. Sections of MDI magnetograms, with maximum colour intensity limits set for absolute fields above 20 Mx cm^{-2}, are shown at times 14:10 (left), 18:16 (middle) and 20:45 (right). From left to right over each magnetogram there are, respectively, 51, 52 and 33 blinkers. The $\times$s indicate the blinkers that peak in the left and middle frames whilst the $*$ indicates the blinker shown in Figure 2.2

The location of the blinkers can be compared to the magnetic fragments in the photosphere below. In Figure 5.1, the location of the midpoint of the QS blinkers ($\triangle$s) are drawn over sections of MDI magnetograms taken at three different times. Note, that the blinkers themselves are much bigger than the symbols shown. The $\triangle$s over each magnetogram, going from left to right, are those that occur in the first 4 hrs 11 mins, the next 4 hrs and 32 mins and the final 2 hrs

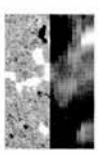

and 56 mins of the data set, respectively. The blinker shown in Figure 2.2 is marked with an $*$ and the underlying MDI image is taken at 20:45, the nearest frame to the peak of this blinker. The $\times$s indicate the blinkers that peak at the same time as the other two magnetograms. Although all the other blinkers are marked, it is important to remember that they peak at different times, and, therefore, the actual magnetic field below may have changed considerably.

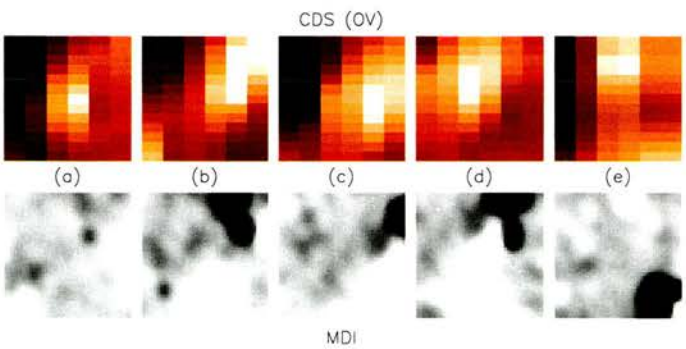

Figure 5.2: Images in the CDS O V line of the five blinkers indicated in Figure 5.1 by $\times$s and a $*$; (a) - (e) corresponds to their order from left to right as seen in Figure 5.1. The MDI images are of the magnetic field below the blinkers taken at the time of the peak of each blinker; maximum colour intensity limits set for absolute fields above 20 Mx cm^{-2}.

Consider the five blinkers that peak at the time of the images (shown by $\times$s and an $*$) in Figure 5.1. Figure 5.2 shows a close up of these blinkers taken by CDS in the O V line, as well as the corresponding magnetic field below. The blinkers from left to right (a) - (e) are ordered as they are seen from left to right in Figure 5.1. The first blinker, Figure 5.2 (a), appears above a region where there are no fragments except a small, weak negative magnetic fragment to the right. The second, Figure 5.2 (b), occurs directly above a large negative fragment, although the blinker may just touch the large positive fragment below. The blinker in Figure 5.2 (c) is similar in that it is predominantly over the large positive fragment, but may just touch the large negative one nearby. In Figure 5.2 (d) the blinker overlies large fragments of both polarities, whilst the last blinker, Figure 5.2 (e), just overlies the positive fragment at the top of the image.

Clearly, from the illustration of these five blinkers, we see that the nature of the magnetic fields below blinkers is not clear cut. All situations arise. Mixed magnetic fields directly below a blinker is not essential, however, in most cases a reasonable sized magnetic fragment of one polarity is found. In Figure 5.1 it appears as if a few blinkers occur in regions where there are no well defined fragments. A similar likelihood ratio test to that described in Section 2.5 is

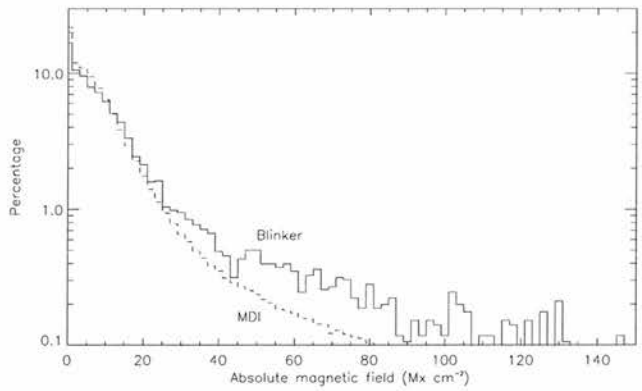

Figure 5.3: Distribution of blinker pixel values (*solid*) and all pixel values (*dashed*) versus absolute magnetic flux.

performed to determine whether blinkers preferentially occur above regions of strong absolute magnetic field. Here the MDI pixels are binned into k bins according to their absolute field strength with, this time M representing the total number of MDI pixels, M_i the number of these pixels in each bin, n represents the total number of MDI pixels associated with the peak of each blinker and n_i the number of these pixels in each bin. The likelihood ratio statistic, w_k, is calculated in exactly the same way as before. We find that w_k (which equals 580.5) is considerably larger than the χ^2_{k-1}, (which equals just 27.9 for $k = 9$) and so the distribution of the blinkers above the magnetic field is not uniform. Furthermore, by comparing the distribution of absolute magnetic field in the blinker pixels (identified with $n_\lambda = 5$ and $n_p = 3$) and the absolute strength of the magnetic field in all the pixels (Figure 5.3) we see that blinkers do generally occur above the pixels with stronger absolute field strength. As we have already seen, however, blinkers can also occur above all field strengths and are not just confined to strong fields. This may be because, the actual roots of the field lines involved in the blinker have strong field, but are confined in rather small areas, whereas due to the canopy effect (Gabriel, 1976) the blinker itself may spread over a much wider area.

5.2.2 Comparison of blinker properties and magnetic field strength

If we consider a histogram of the magnetogram values and fit a Gaussian to its core, the ratio of the survival functions of the Gaussian and the data show that, above 20 G, 1% of the pixels are associated with noise. Hence, in the quiet-Sun data set, we only consider pixels with absolute

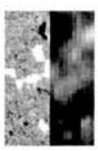

value greater than 20 Gauss.

As shown in Table 2.1, 136 blinkers were identified in the QS with $n_\lambda = 5$ and $n_p = 3$. If we consider the magnetic field directly below these blinkers at the time of their peaks, 8% have no absolute magnetic field above 20 G below them, 22% have only negative polarity below -20 G, 33% have only positive polarity above 20 G, and 37% have both positive and negative field. Of the 50 blinkers that have mixed field associated with them, the ratio of minority to majority field is between 0.1 and 1.0.

This suggests that it is the presence of large or strong magnetic regions that is important for blinkers rather than close pairs of opposite polarity magnetic fragments. It is interesting that 33% of blinkers occur above regions where large positive fragments dominate, whereas only 22% occur above regions where negative fragments dominate. This is probably because our CDS rasters have only a fairly small field of view and are situated above regions of network field that are dominated by positive magnetic fields.

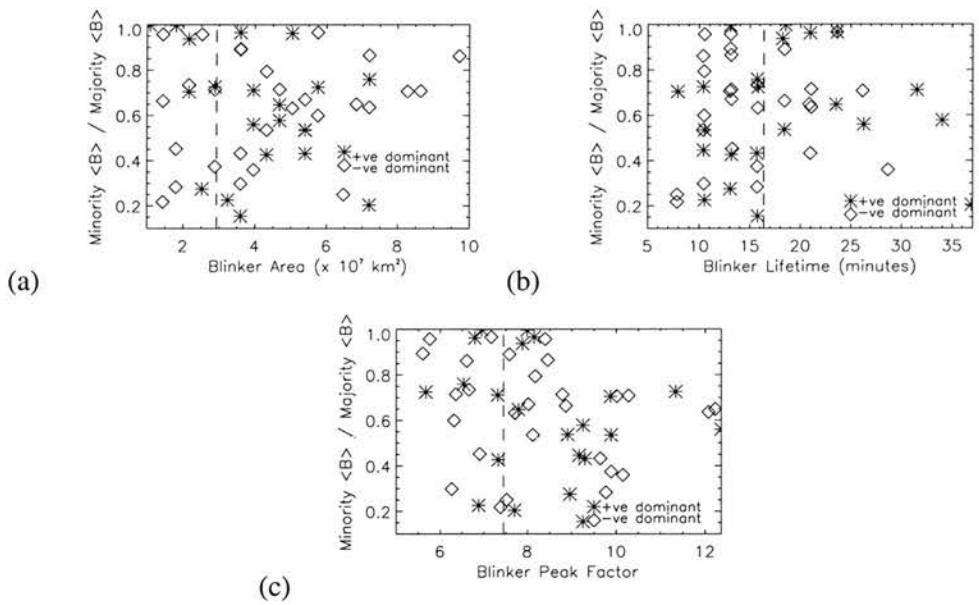

Figure 5.4: Quiet Sun Minority $\langle B \rangle$/Majority $\langle B \rangle$ versus (a) blinker area, (b) lifetime and (c) peak factor for blinkers with both positive and negative field directly beneath them ($|B| > 20$ G).

Figure 5.4 shows the ratio of minority mean field and majority mean field versus (a) area, (b) lifetime and (c) peak factor for blinkers that have both positive and negative field associated

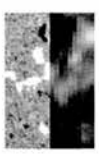

with them. In all graphs, the $\diamond$'s ($*$'s) show blinkers that have majority negative (positive) field associated with them. In each graph, the *dashed* lines mark the mean area, lifetime and peak factor, respectively. The random spread of the data points suggest that there is no correlation between the ratio of the mixed magnetic field strengths and the blinker area, lifetime or peak factor.

Figure 5.5 shows the absolute mean field versus the same blinker characteristics for blinkers that have only positive or negative field associated with them. The $\diamond$'s ($*$'s) show blinkers that have just negative (positive) field associated with them.

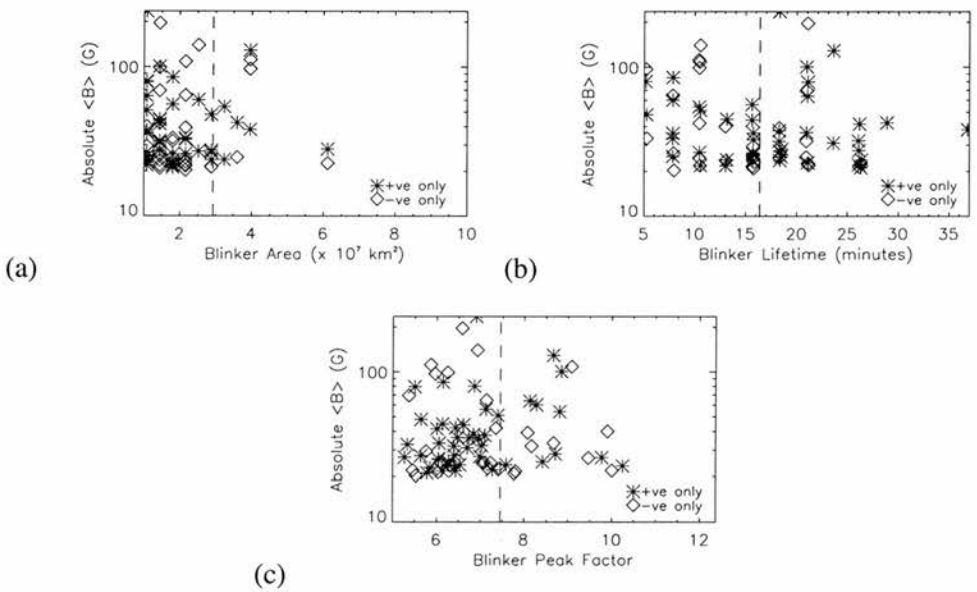

Figure 5.5: Quiet Sun absolute $\langle B \rangle$ versus (a) blinker area, (b) lifetime and (c) peak factor for blinkers with either positive or negative field directly beneath them ($|B| > 20$ G).

87% of these blinkers have an area that is less than the mean area and 75% have a peak factor less than the mean. This implies that it maybe the small size of the blinkers that is leading us to find just one polarity and there may indeed be an opposite polarity fragment close by, but not directly below the blinker. Again, there appears to be no correlation between the strength of the magnetic field and the blinker area, lifetime or peak factor.

5.3 Active-region blinkers

5.3.1 Relationship to the magnetic field

In Figure 5.6 the △s indicate the locations of the midpoints of the $n_\lambda = 5$ and $n_p = 3$ AR blinkers with respect to the magnetic field and white light images. (Note: the size of the blinkers is larger than the symbols shown). The △s plotted are those that occur (from left to right) in the first 1 hour 50 minutes, the next 2 hours 2 minutes and the last 1 hour and 47 minutes, respectively, of the observing sequence.

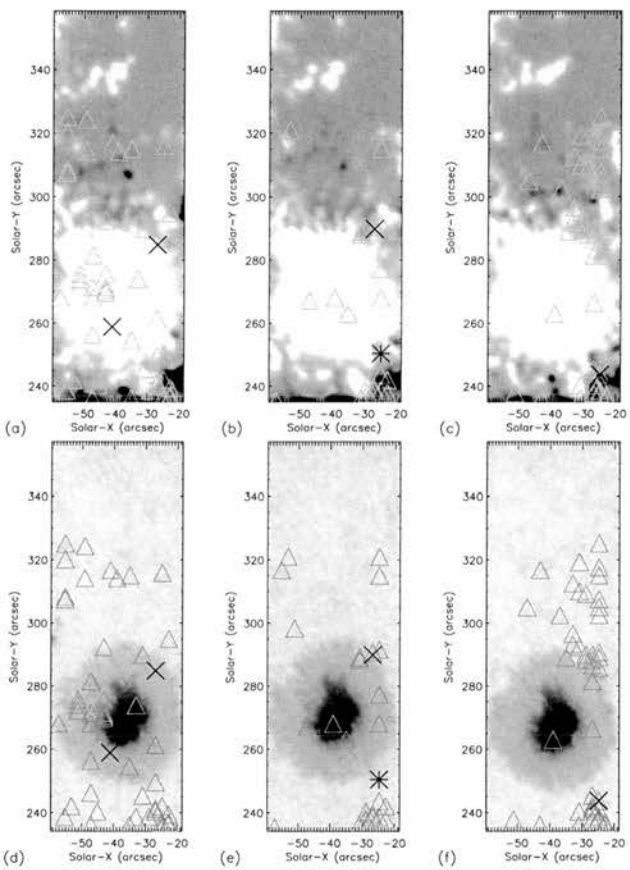

Figure 5.6: Comparison of the location of the midpoints of the O V $n_\lambda = 5$ and $n_p = 3$ AR blinkers (△) with the underlying magnetic field (a) - (c) and white light images (d) - (f). The sections of MDI magnetograms, with maximum colour intensity limits set for absolute fields of 500 Mx cm^2, and MDI white light images are shown at times 20:07 (left), 22:10 (middle) and 00:07 (right). The ×s indicate the blinkers that peak in the corresponding frame and the ∗ indicates the blinker seen in Figure 3.2 (d).

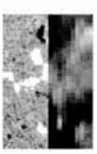

The blinker shown in Figure 3.2 (d) is identified with a $*$ and is drawn over the MDI image taken at 22:10, the nearest frame to the peak of that blinker. The $\times$s shown on the magnetograms and white light frames indicate the blinkers that peak at the times of the MDI images underneath them. From left to right over each magnetogram and white light image there are, respectively, 51, 27 and 47 blinkers. It is important to note that the underlying magnetic field can change substantially in between the frames such that the positions of the blinkers shown by the $\triangle$s may be misleading since these blinkers do not peak at the time of the MDI images they are plotted over.

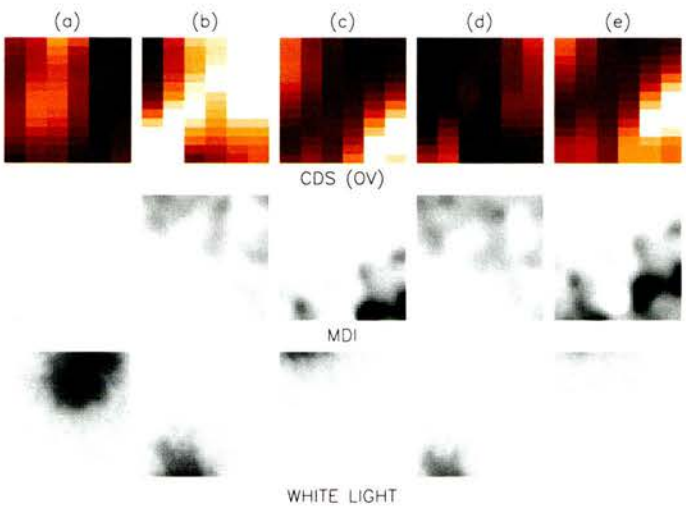

Figure 5.7: CDS O V images of the five blinkers indicated in Figure 5.6 by $\times$s and an $*$; (a) - (e) corresponds to their order from left to right as seen in Figure 5.6. The MDI magnetogram images show the magnetic field below the blinkers taken at the time of the peak of each blinker; maximum colour intensity limits are set for absolute magnetic fields above 500 Mx cm^{-2}. MDI white light images showing the umbra and penumbra of the sunspot are also shown.

We focus on the 5 blinkers marked with the $*$ and $\times$s that peak at the times of the MDI images. Figure 5.7 shows a close up of each blinker as seen in O V from the CDS data, the underlying magnetic field taken by MDI and the photosphere as seen in white light. The blinkers in Figure 5.7 are ordered as they are seen from left to right in Figure 5.6. The first blinker, Figure 5.7 (a), is situated over the positive sunspot which dominates the MDI frame. From the white light it is clear that the blinker is on the edge of the umbra and penumbra. In Figure 5.7 (b), the second blinker, which is on the edge of the penumbra of the sunspot over some smaller positive fragments, is shown. The third blinker, Figure 5.7 (c), is positioned near the edge of the sunspot

in the bottom right-hand corner of the frame outside the penumbra. This blinker is found to be associated with a negative fragment rather than with the sunspot. The fourth blinker, Figure 5.7 (d), is similarly placed just outside the penumbra but this time on the edge of a large positive fragment, whilst the fifth blinker, Figure 5.7 (e), is associated with a region that includes both large positive and negative polarities, but is primarily situated over a negative fragment.

Analysis of the white light data does not reveal any evidence of umbral spots or light bridges being present within the umbra of the sunspot investigated, and therefore, no connection between blinkers and these sunspot phenomena can be made.

These results suggest that the nature of the magnetic fragments below blinkers does not have a unique configuration, indeed all combinations of magnetic fragments can exist below a blinker. Furthermore, it seems clear, from the blinkers located above the sunspot, that mixed polarity is not a necessary condition for a blinker to occur.

5.3.2 Comparison of the blinkers in sunspot and non-sunspot regions

Properties	Sunspot		Non-Sunspot	Active Region
	Umbra	Penumbra		
No. of blinkers	6	18	101	125
Global frequency (s^{-1})	12.5	10.8	14.4	13.7
Mean intensity enhancement factor	2.0	2.4	2.4	2.4
Mean area ($\times 10^7$ km^2)	3.2	5.2	3.8	3.9
Mean lifetime (minutes)	19.6	17.0	17.5	17.5
Mean rise time (minutes)	11.7	8.1	8.5	8.6
Mean fall time (minutes)	7.8	8.9	9.0	8.9
Rise time>Fall time	4	6	44	54
Rise time<Fall time	1	10	37	48
Rise time≈Fall time	1	2	20	23

Table 5.1: Properties of the active-region O V $n_\lambda = 5$, $n_p = 3$ blinkers that were observed above the sunspot in either the umbra or penumbra, non-sunspot regions and the whole active region.

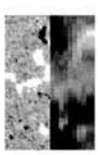

As seen in Section 5.3.1, the AR O V blinkers identified are found both inside a sunspot with their midpoints situated above both the umbra and penumbra, as well as in the surrounding (non-sunspot) region. To check that these types of events are all the same, we compare their properties which are shown in Table 5.1. Most of the properties of the three types of blinker are fairly similar. There are a few small differences, but due to the low statistics it is not clear whether these are significant. For instance, the mean lifetimes of the umbral, penumbral and non-sunspot blinkers appear to be approximately the same, although the umbral blinkers seem to last a little (11%) longer and the penumbral blinkers seem to last a little (3%) shorter then the non-sunspot blinkers. The mean areas of the umbral and penumbral blinkers are 16% smaller and 37% larger, respectively, than those for the non-sunspot blinkers, however, these differences are still within the observed spread of non-sunspot blinker areas. The penumbral blinkers appear to have the same mean intensity enhancement factor as non-sunspot blinkers, however, the umbral ones are 17% weaker. The frequency of occurrence of sunspot blinkers in both the umbra and penumbra is slightly lower than that for non-sunspot blinkers but is still higher than that for QS blinkers. There are more umbral blinkers with rise times greater than fall times and more penumbral blinkers with rise times less than fall times than in the non-sunspot case, however, this is most likely to be due to the small numbers of events detected. Therefore, we conclude that the properties of the three different types of blinkers are similar enough to suggest that sunspot blinkers are essentially the same as non-sunspot blinkers. Finally though, we note that only 46% of the O V sunspot blinkers can also be observed in either He I or O IV, whereas 73% and 91%, respectively, of the non-sunspot O V blinkers can also be observed in these lines. The physical significance of this discrepancy is not clear. Indeed, it may again simply be due to the small number of sunspot blinkers observed.

5.3.3 Comparison of blinker properties and magnetic field strength

From Figure 5.6, it appears that there are blinkers that occur in regions where there is little or no significant magnetic fragments. This may, of course, be because the fragments associated with these blinkers have either cancelled or not yet emerged in the particular frame shown. As in Section 5.2.2, we consider the magnetic field directly below the blinkers at the time of their peak and compare the magnetic field strength with the area, lifetime and peak factor of the blinkers.

For the active-region data set, analysis of the magnetic field shows that for pixels above 45 Gauss,

only 1% of the data is associated with noise, hence, we only consider pixels with absolute value greater than 45 G.

As shown in Table 3.1, 125 blinkers were found with $n_\lambda = 5$ and $n_p = 3$. Of these, 1% of blinkers have no absolute magnetic field greater than the cutoff directly below them, 13% have only negative field, 37% have only positive field, and 49% have both positive and negative field directly below them.

Figure 5.8 is similar to Figure 5.4 and shows a comparison of the ratio of the mean magnetic field strengths beneath blinkers, that are associated with mixed field, with the (a) blinker area, (b) lifetime and (c) peak factor.

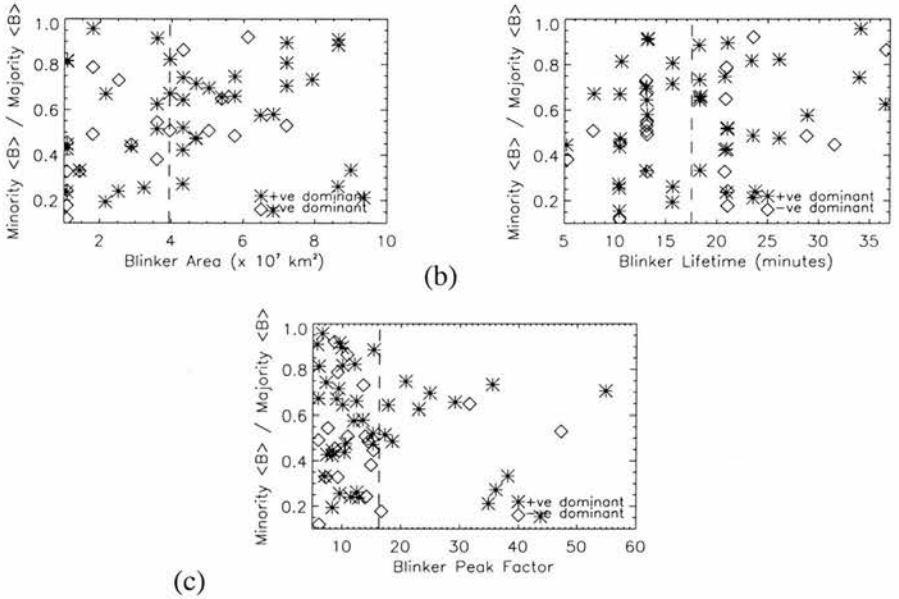

Figure 5.8: Active region Minority $\langle B \rangle$/Majority $\langle B \rangle$ versus (a) blinker area, (b) lifetime and (c) peak factor for blinkers with both positive and negative field directly beneath them. $|B| > 45$ G.

As in the quiet Sun, the random spread of the data points in all the graphs suggest that there are no correlations between the ratio of mixed field and the blinker characteristics.

Figure 5.9 is similar to Figure 5.5 and shows a comparison of absolute mean magnetic field beneath blinkers that are associated with a single polarity field and (a) the blinker area, (b) lifetime and (c) peak factor.

82% of blinkers have an area that is greater than the mean and 79% of blinkers have a peak factor

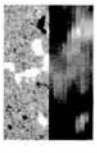

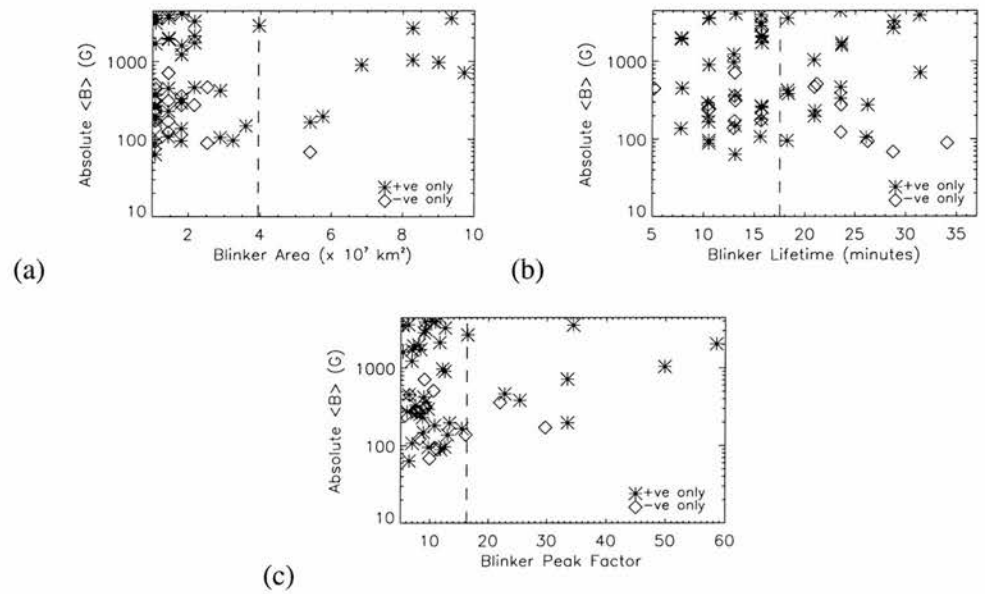

Figure 5.9: Active region absolute $\langle B \rangle$ versus (a) blinker area, (b) lifetime and (c) peak factor for blinkers with either positive or negative field directly beneath them ($|B| > 45$ G).

greater than the mean peak factor. As in the quiet Sun, this may mean that we have not searched in a wide enough area around each blinker to find any opposite polarity field. Again, there is no correlation between the strength of the magnetic field and the blinker characterisitcs.

5.4 Conclusions

A statistical analysis was used to show that QS blinkers have a preference for regions with strong absolute magnetic fields. This is of course to be expected, since we find 99% of them occur above the network. Analysis of the position of blinkers with respect to magnetic fragments show that 8% have no magnetic field above 20 G (cutoff) directly below them, 55% have only single polarity field associated and 37% have mixed field below them. These results suggest that local mixed polarity field is not a key ingredient for blinkers and, hence, insitu magnetic reconnection may not be the mechanism that causes blinkers. This does not, however, say anything about reconnection occuring at the opposite magnetic field footpoint from the blinker. Further analysis of the magnetic field in the vicinity of the blinker would be needed to determine whether this is a valid mechanism.

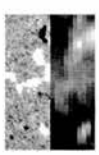

Our analysis of the magnetic field below AR blinkers reveals that they can occur both inside a sunspot and in the surrounding non-sunspot region. The blinkers that occur inside a sunspot occur both in the umbra and the penumbra. Furthermore, the properties of the blinkers in these regions are comparable and so we believe that they are both created by the same mechanism. Investigations of the magnetic fragments below blinkers show that no specific magnetic fragment pattern is needed for blinkers to occur. Blinkers do, however, show a slight preference for regions of strong unipolar field with 50% having only single polarity field directly below them. Only 1% had no magnetic field above the 40 G cutoff below them and 49% had both positive and negative polarity field directly below.

In both quiet Sun and active regions, there is no correlation between the strength of the magnetic field and the area, lifetime or peak factor of the blinkers. This suggests that blinkers are not caused by reconnection directly below them, but another, as yet, unknown process.

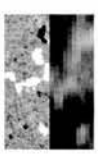

Chapter 6

Blinkers and Explosive Events

There has been much speculation over recent years as to whether blinkers and explosive events are the same phenomenon observed with different instruments. As discussed in the introduction, blinkers are observed SOHO/CDS and explosive events are observed using SOHO/SUMER. In this Chapter, we use co-aligned SUMER and CDS data to compare blinkers and explosive events. The CDS data is the QS data set used in Chapter 4, which is described in detail in Section 4.1. The SUMER data have been supplied and are used with the permission of Davina Innes (Max-Planck, Lindau). We investigate only those blinkers that have been identified using BLIP and have parameters $n_\lambda = 5$ and $n_p = 3$.

6.1 Properties of blinkers and explosive events

Table 6.1 shows the general properties of QS and AR blinkers identified using BLIP with n_λ equal to 5 and n_p equal to 3 and also the properties of explosive events (Dere et al., 1989). Dere et al. (1989) give the birth rate of explosive events as 1×10^{-20} cm^{-2} s^{-1} in the quiet-Sun which is equivalent to a global frequency of 600 s^{-1}, if we assume that this birth rate is representative of the whole Sun. They also quote a size of 2 arcsec^2 for an explosive event which is equivalent to an area of 0.1 $\times 10^7$ km^2.

Comparing the results from this table, we see that blinkers are 60 times less frequent than explosive events, 20 times larger in area, and 20 times longer in lifetime. The intensity enhancement factors of both phenomena are approximately the same.

Property	QS Blinkers	AR Blinkers	Explosive Events
Global frequency (s^{-1})	10.8	13.7	≈ 600
Mean intensity enhancement factor	1.9	2.4	2-5
Mean area ($\times 10^7$ km^2)	2.7	3.9	≈ 0.1
Mean lifetime (minutes)	19.2	17.5	1.0 - 6.0

Table 6.1: Properties of QS and AR O V blinkers and explosive events

Explosive events have been identified in quiet Sun, active regions and coronal holes (Dere et al., 1989, 1991). Blinkers have also been identified in both the quiet Sun and active regions, as discussed in Chapters 2 and 3, and, from the initial analysis of a CDS O V data set covering a coronal hole region, we also believe blinkers may occur in coronal holes. A complete analysis of this new data, however, is needed to determine the properties of these coronal hole events to determine if they really are blinkers. Both blinkers and explosive events, therefore, appear to occur throughout the transition region in all regions.

In Chapters 2 and 3, we also investigated the signatures of blinkers in various wavelengths throughout the solar atmosphere. We have shown that 27% of QS and 68% of AR blinkers can be seen in the He I chromospheric line. Explosive events are also seen in the chromosphere (Madjarska and Doyle, 2002). In the hotter coronal lines no QS blinkers and only 18% of AR blinkers are identified, whereas explosive events are only seen occasionally in the corona (Dere, 1994).

As described in the Introduction, explosive events are identified by the short-lived, but large velocities that are associated with them. In Chapter 4, we investigated the Doppler velocity of blinkers in the chromosphere and the transition region. We found that the Doppler velocity of plasma in blinkers is preferentially more red-shifted than the whole of the chromosphere and transition region and range from 10 - 20 km s^{-1} in He I and 15 - 35 km s^{-1} in O V. The velocity of an explosive event, however, can reach 100 km s^{-1} and they can also show evidence of highly turbulent motions which can reach 500 km s^{-1}. This appears to be a clear difference between blinkers and explosive events which arises because either the two phenomena are different or because there are differences in the instrument resolution and sensitivity used to observe them. SUMER has a higher spectral resolution and smaller pixels than CDS, so is more sensitive to detecting Doppler shifts of small regions of plasma. The larger CDS pixels may not be sensitive

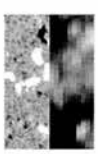

enough to pick up such changes in velocity. More recently, however, Innes (2001) looked for enhancements in the wings of line profiles to determine the velocities of explosive events. We undertake an initial investigation of wing enhancements in CDS blinkers profiles in this Chapter.

In Chapter 5, we investigated the magnetic field structure of blinkers. We have shown that blinkers are preferentially located above regions where a single polarity dominates, whether this is in the quiet Sun or above a sunspot in an active region. We also showed that the strength of the field beneath the blinker has no bearing on the area, lifetime or peak factor of the blinker, suggesting that insitu reconnection may not be the mechanism that causes them. Explosive events, however, have been found to be associated with regions of complex weak field or on the edges of unipolar field (Porter and Dere, 1991). Dere et al. (1991) and Dere (1994) associated explosive events with magnetic reconnection that occurred during the cancellation of magnetic flux and Innes et al. (1997) present a model of the magnetic reconnection configuration required for an explosive event to occur.

6.2 Data

The data used in this Chapter are taken from the CDS and SUMER instruments. The CDS data are a series of feature tracking rastered images, the same data as that used in Chapter 4 and is described in Section 4.1. It contains 6 emission lines (He I, O III, O IV, O V, Mg IX and Mg X), covers an area of $40'' \times 124''$ with pixels of size $4'' \times 1.6''$, and has a 15 second exposure time and a cadence of 151 seconds. We use only the O V data and only investigate blinkers identified using BLIP with n_λ equal to 5 and n_p equal to 3.

The SUMER data are a series of Si IV single slit line profiles formed at a temperature of 6.6×10^4 K. The data has 15 second cadence and a pixel size of $1'' \times 2''$. The SUMER data tracks the same part of the Sun within $1''$ throughout the time sequence. A full description of the data and the preparation used can be found in Innes (2001). The SUMER data coincides with the CDS data for 3.5 hours from the start of the CDS S11484 data sequence at 12:30 until 15:49. The cadence of the SUMER data has been reduced to that of the CDS data. The SUMER and CDS data have been aligned using the position information given in the header structures of the data. This alignment is known to have an error of approximately $5''$. An additional alignment correction, calculated by directly comparing the CDS rasters and the SUMER data was used,

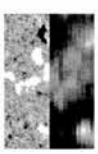

achieving a final alignment error of between $2'' - 3''$.

The explosive events investigated in Innes (2001) are identified where the intensity in the red or blue non-Gaussian wing is greater than 8×10^{12} ph s^{-1} cm^{-2} sr^{-1}. The core Gaussian was assumed to have a Doppler width of 21 km s^{-1}, an amplitude equal to the maximum value of the line and a line centre position at the actual line centre. The wing components were then computed from the excess emission in the line profile compared to the core Gaussian. The width of 21 km s^{-1} is based on the average width of the line throughout the data set.

Previously, we have only investigated the line shift and broadening of blinkers. Here we attempt to repeat the analysis undertaken by Innes (2001) and investigate the non-Gaussian wing enhancements in CDS blinker profiles. We compare not only the location of blinkers and explosive events in a co-aligned data set, but also the SUMER and CDS line profiles of the events. We know the velocity of the explosive events calculated from the wing enhancements (Davina Innes, private communication), and also the Doppler velocity and broadening of the whole of the blinker. We also repeat the analysis of Innes (2001) and determine the velocity of the blinker using the wing enhancement technique. For our reference core Gaussian, we use a Gaussian with amplitude equal to the maximum of the profile, the line centre and width of the line equal to the reference wavelength and width at the time of the profile. These are both calculated in Appendix B. We choose this as our reference Gaussian since we know from previous analysis that the Gaussian parameters vary in time throughout the data.

6.3 Comparison of blinker and explosive event location

In the co-aligned CDS O V and SUMER Si IV data, we observe 58 blinkers and 8 explosive events (Davina Innes, private communication). After comparing the locations of both with respect to each other, we find that during this 3.5 hour data set three different scenarios occur, namely: a co-spatial and co-incident blinker and explosive event; a blinker with no associated explosive event; and an explosive event with no associated blinker. We investigate these three scenarios in more detail in the following subsections.

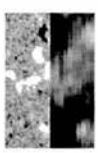

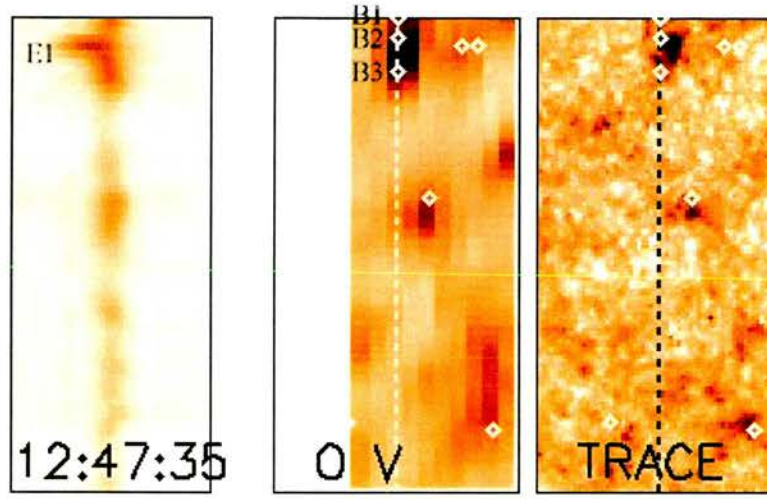

Figure 6.1: SUMER Si IV single slit data (*left*), CDS O V rastered data (*middle*) and simulated TRACE C IV data (*right*). The ⋄'s on the CDS and TRACE data are the mid-points of blinkers identified with $n_\lambda = 5$ and $n_p = 3$, whilst the vertical *dashed* lines indicate the position of the SUMER slit.

6.3.1 Blinker and explosive event

The first scenario, that of a coincident blinker and explosive event is seen at time 12:47. The images in Figure 6.1 show an image of the SUMER Si IV single slit data (*left*), a CDS O V raster (*middle*) and a simulated TRACE C IV image (*right*). The *dashed* lines and ⋄s on the CDS and TRACE data mark the positions of the SUMER slit and the mid-points of the $n_\lambda = 5$ and $n_p = 3$ blinkers, respectively. The SUMER image is an intensity plot of wavelength (x-axis) versus position along the slit (y-axis). At the top of the SUMER Si IV frame an explosive event (E1), that has a maximum velocity of approximately -120 km s^{-1}, can be seen. At the same location in the CDS O V raster, three blinkers (B1, B2 and B3) are also observed. The middle blinker (B2) is the nearest spatially to the explosive event. This is the only example within our 3.5 hour sequence of data of a blinker and an explosive event together.

Figure 6.2 (a) shows the SUMER Si IV lightcurve of the explosive event, E1. Figure 6.2 (b) shows the CDS O V lightcurve of the blinker labeled B2. The start and end of the blinker are marked with •s. The *dashed*, *solid* and *dotted* lines refer to times, t1, t2 and t3, which correspond to the time before, the time of the frame shown in Figure 6.1 and the time after. The data shown in Figure 6.1 were taken at time t2. Figure 6.2 (c) shows the SUMER Si IV line profile for the

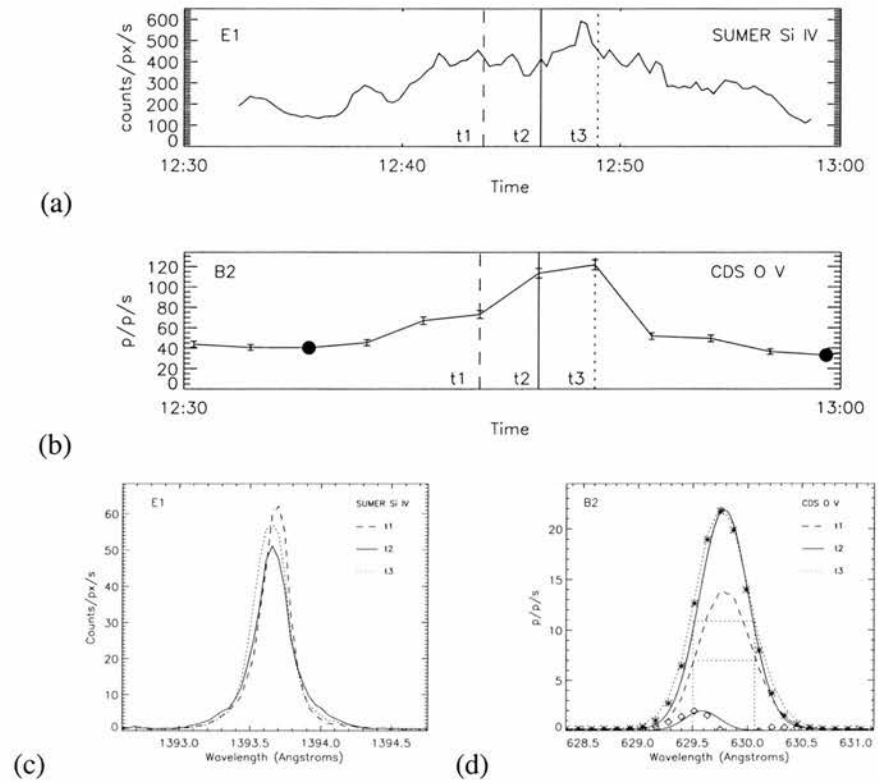

Figure 6.2: (a) SUMER Si IV lightcurve for the explosive event, E1. (b) CDS O V lightcurve for blinker, B2. The •s mark the start and end of the blinker. (c) SUMER Si IV line profiles at times, t1 (*dashed*), t2 (*solid*) and t3 (*dotted*), of the explosive event, E1. (d) CDS O V line profiles at times, t1 (*dashed*), t2 (∗s) and t3 (*dotted*) for the blinker, B2. The reference Gaussian at time t2 is plotted with a *solid* line and the wing enhancement is plotted with ⋄s and is fitted with a Gaussian function (*solid*)

explosive event, E1, at times, t1, t2 and t3. Figure 6.2 (c) shows a plot of the CDS O V line profiles for the blinker, B2 at times, t1 (*dashed*), t2 (∗s) and t3 (*dotted*). The full-width-half-maximum (FWHM) of the two CDS line profiles taken at times t1 and t2 have been drawn on this graph with *dotted* lines. The reference Gaussian for time t2 is plotted with a *solid* line and the non-Gaussian wing enhancement in the CDS line profile at time, t2, is plotted with ⋄s and has been fitted with a Gaussian (*solid*). The SUMER lightcurve shows a decrease and in intensity from 420.1 counts/px/s to 414.2 counts/px/s between times t1 and t2, and then an increase in intensity between times t2 and t3 from 414.2 counts/px/s to 452.1 counts/px/s. This variation can also be seen in the SUMER line profiles as a decrease in amplitude with a slight broadening

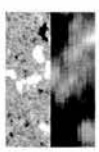

of the line at time t2, and an increase in amplitude with a broadening of the line at time t3. There is evidence of a blue-shift in the line profiles and an enhancement on the blue side of the profile which correspond to a maximum velocity of about -120 km s^{-1}.

The blinker can be seen to be in its rise phase with an increase of intensity from time, t1 to time, t2 and reaching its peak at time t3. There is an intensity increase in the SUMER over the whole time range, but it is not clear whether this is evidence of a blinker or whether it is due to the short time range and long duration of the blinker. The increase in amplitude of the spectral lines from times t1 to t2 and to t3 corresponds to the increase of intensity of the blinker in Figure 6.2 (a), as one would expect. There is a small line shift that corresponds to a velocity of 0.4 km s^{-1} between times, t1 and t2, which is below the CDS resolution, but there is no evidence of a broadening. A non-Gaussian wing enhancement that has 5.7% of the flux of the whole profile is also observed. It has a velocity of -95.0 km s^{-1}. This indicates that we may be able to observe SUMER wing enhancements in CDS. Between times t2 and t3, there is no evidence of a line shift, but there does appear to be a broadening of the line. This suggests that we might be seeing evidence of the exploisve event in the CDS line profiles.

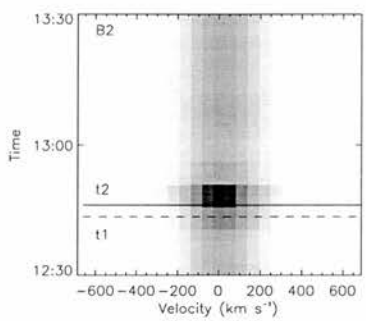

Figure 6.3: Intensity plot of velocity (wavelength) vs time for blinker B2. The *dashed* and *solid* line correspond to times, t1 and t2.

Figure 6.3 shows an intensity plot of wavelength versus time for blinker B2. The *dashed* and *solid* lines refer to the times t1 and t2. The blinker can be clearly seen as the dark enhancement which peaks just after the time t2, as seen in the blinker lightcurve in Figure 6.2. Like the SUMER line profile, an enhancement/broadening, on the (left) blue side of the profile, can be seen which is at its maximum at the time of the peak blinker intensity, which occurs just after the explosive event seen by SUMER.

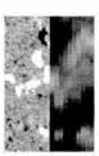

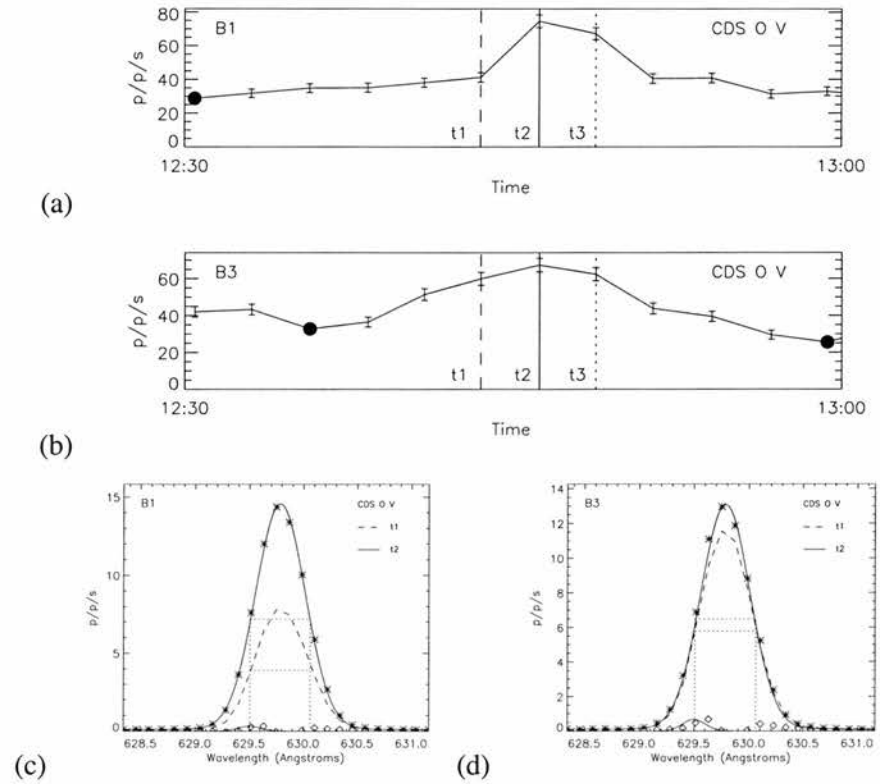

Figure 6.4: Same as Figure 6.2, but CDS O V lightcurves and line profiles are for the two blinkers B1 and B3.

For completeness, we show the lightcurves and the CDS O V line profiles for the other two blinkers, B1 and B3, which occur in the same region (Figure 6.4). As for blinker B2, the CDS O V line profiles show increases in intensity corresponding to the increases in intensity of the blinkers. These increases in intensity are consistent with those seen for the SUMER Si IV event. The two blinkers, B1 and B3, show line shifts that correspond to velocities of 0.2 km s^{-1} and 0.1 km s^{-1}, respectively, between times t1 and t2. These velocities are again below the resolution of CDS. Neither blinkers show any significant line broadening. The blinkers B1 and B3 have small wing enhancements (1.8% and 2.3% of the whole profile) which have velocities of -136.3 and -135.4 km s^{-1}, respectively. These wing components have higher velocities than that seen in blinker, B2, which is the nearest spatially to the explosive event, but they both contain less flux than the wing in blinker, B2.

Figure 6.5 (a) and (b) show intensity plots of wavelength versus time for blinkers B1 and B3, respectively. As previously, for blinker B2, we can clearly see the blinkers at a time just after t2.

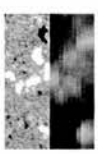

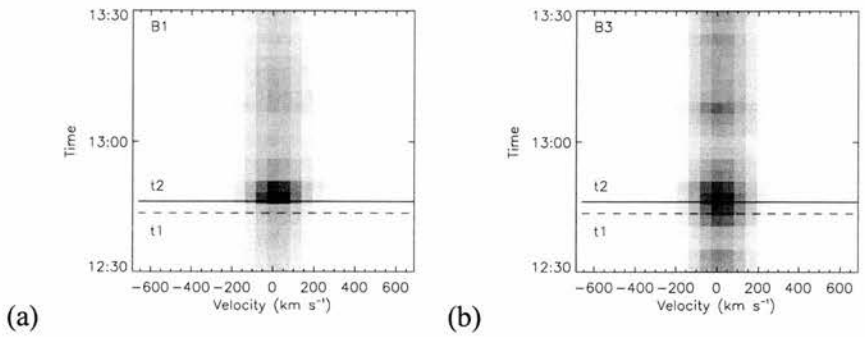

Figure 6.5: As for Figure 6.3, but for blinkers, B1 and B3.

Again in both blinkers, we can see a broadening of the blinker profiles and an enhancement in the wings just after the explosive event occurs, which is again consistent with the wing enhancements seen in Figure 6.4 (c) and (d).

6.3.2 Blinker and no explosive event

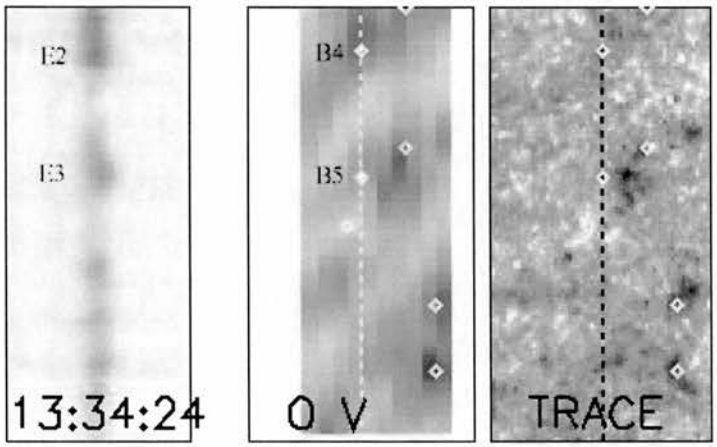

Figure 6.6: As Figure 6.1, but with SUMER Si IV, CDS O V and simulated TRACE C IV frames taken at time 13:34

The second scenario is the situation involving a blinker, but no explosive event. Figure 6.6 shows the same three types of frames as those shown in Figure 6.1 but these frames are taken at time 13:34. Two blinkers, B4 and B5, observed in the CDS O V data, lie along the SUMER slit. In the SUMER Si IV data, the two regions that correspond to B4 and B5 are labeled E2 and E3, but neither region contains an explosive event. These are two examples out of ten observed in the data, where there are blinkers present in the CDS data, but no explosive events seen in the

SUMER data. We investigate these two blinkers and the corresponding SUMER regions in more detail.

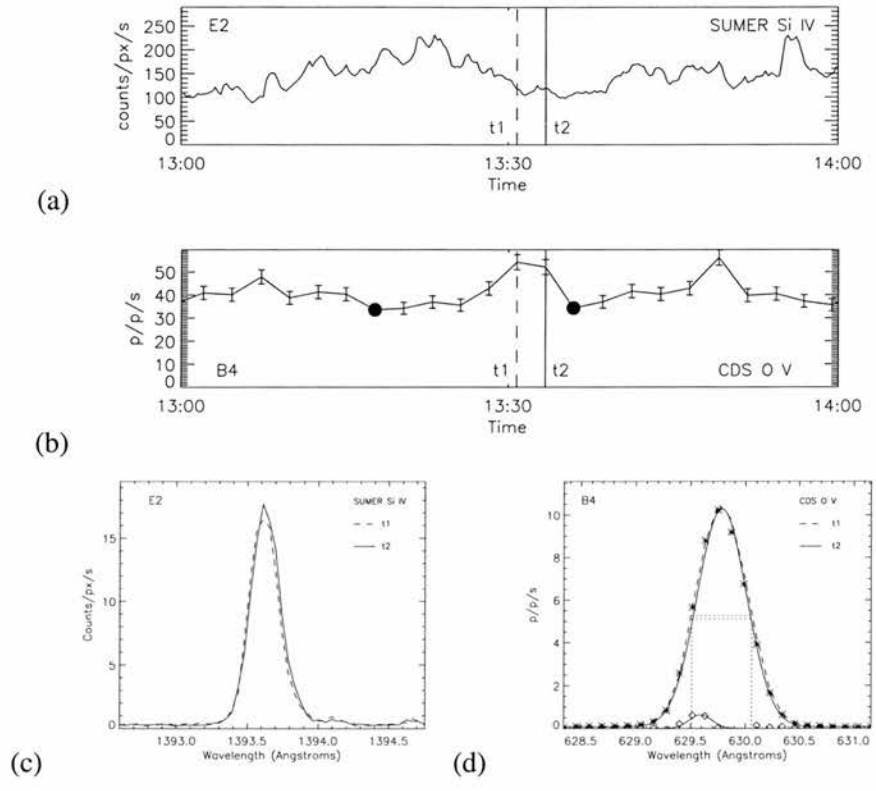

Figure 6.7: As for Figure 6.2, but for SUMER region E2, and blinker B4.

Figure 6.7 is similar to Figure 6.2 and shows (a) the SUMER Si IV lightcurve for the SUMER region E2, (b) the CDS O V lightcurve of blinker, B4, (c) the SUMER Si IV line profiles at times t1 and t2 for the SUMER region E2, and (d) the CDS line profiles of the blinker B4 at times t1 (*dashed*) and t2 ($*$s). Times t1 and t2 have the same meaning as before. Figure 6.7 (d) also shows the fitted reference Gaussian (*solid*) and the non-Gaussian wing component ($\diamond$s) to the CDS profile. The blinker lightcurve shows a decrease in intensity from time t1 to t2, which is also evident in the CDS O V line profiles. There is a small intensity increase in the SUMER lightcurve from 117.9 counts/px/s at time t1 to 119.9 counts/px/s at time t2, but this increase is not a sufficient signature of a blinker. The SUMER Si IV line centre positions do not show a shift between times, t1 and t2, or a significant change in the width of the lines implying no broadening or enhanced wings exist. The CDS O V line centre does have a very small shift that corresponds to a velocity of 0.1 km s^{-1} between times t1 and t2, which is below the CDS resolution, and there is no significant broadening. This is consistent of a region without an explosive event, but

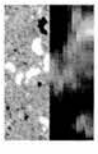

with a blinker. There is, however, a wing enhancement with 2.7% of the flux of the whole profile that has a velocity of -92.0 km s^{-1}.

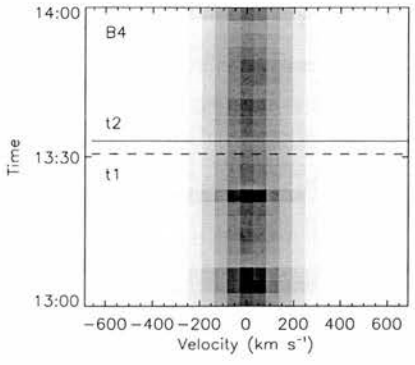

Figure 6.8: As for Figure 6.3, but for blinker B4.

Figure 6.8 is similar to Figure 6.3 and shows an intensity plot of wavelength versus time for blinker B4. The blinker in this Figure is not as clear as the previous examples, and shows a slight broadening during the whole of the time period. There does not appear to be a significant enhancement in the wings of the profile. This suggests that blinkers are slightly broader than the surroundings, but do not show significant wing enhancement. This is consistent with the small wing enhancement seen in Figure 6.7 (c).

Figure 6.9 (a) the SUMER Si IV lightcurve for the region E3, (b) shows the CDS O V lightcurve for the blinker, B5, (c) the SUMER Si IV line profiles for the SUMER region E3 and (d) the CDS O V line profiles for the blinker B5. As in the previous example, the blinker is nearing the end of its lifetime and so a decrease in intensity is seen between times t1 and t2 in the CDS lightcurve and line profiles. Again there does not appear to be any evidence of the blinker in the SUMER lightcurve. The SUMER line profiles also show a increase in amplitude with the total intensity increasing from 220.5 counts/px/s at time t1 to 243.5 counts/px/s at time t2. There is no evidence of a line shift or broadening in the SUMER Si IV line. In the CDS O V line there is a small shift that corresponds to a velocity of 1.9 km s^{-1} between t1 and t2, which is again below the resolution of CDS, but again, no significant broadening. A small wing enhancement with 1.5% of the flux of the whole profile is also seen with a velocity of -79.2 km s^{-1}.

Figure 6.10 shows an intensity plot of wavelength versus time for blinker B5. The peak of the blinker can clearly be seen to occur before time t1, which is consistent with the blinker

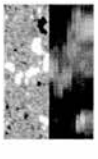

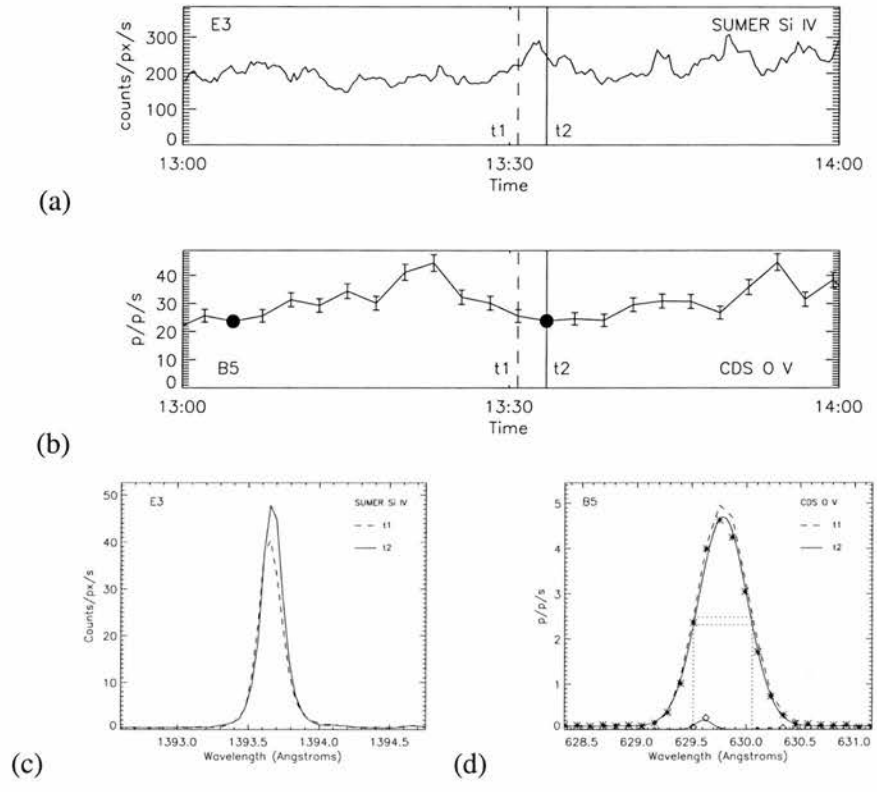

Figure 6.9: As Figure 6.2, but for SUMER region E3, and blinker B5

lightcurve seen in Figure 6.9. As with blinker B4, there is a slight broadening in the whole of the time period, but there does not appear to be a significant wing enhancement at the time of the blinker.

6.3.3 Explosive event and no blinker

Figure 6.11 is similar to Figures 6.1 and 6.6. At the top of the SUMER Si IV frame (*left*), a bi-directional explosive event can be seen; it is labeled E4. In the CDS O V data, the corresponding region, B6, shows no blinker. This is one of seven cases in the data, where an explosive event is observed in the SUMER data, but no associated blinkers are seen in the CDS data.

Figure 6.12 (a) shows a lightcurve of the SUMER Si IV E4 region. Figure 6.12 (b) shows a lightcurve for a group of six pixels in region B6. The *dashed* and *solid* lines mark the two times, t1 and t2, at which the line profiles are drawn. The intensity of the region increases between times t1 and t2. The intensity of the SUMER region has a substantial increase between time

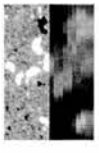

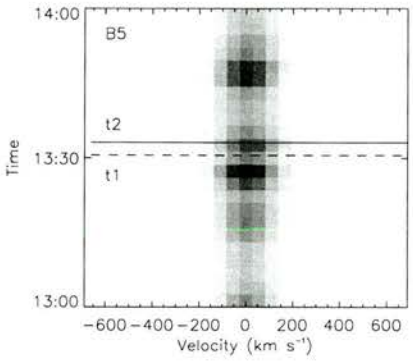

Figure 6.10: As for Figure 6.3, but for blinker B5.

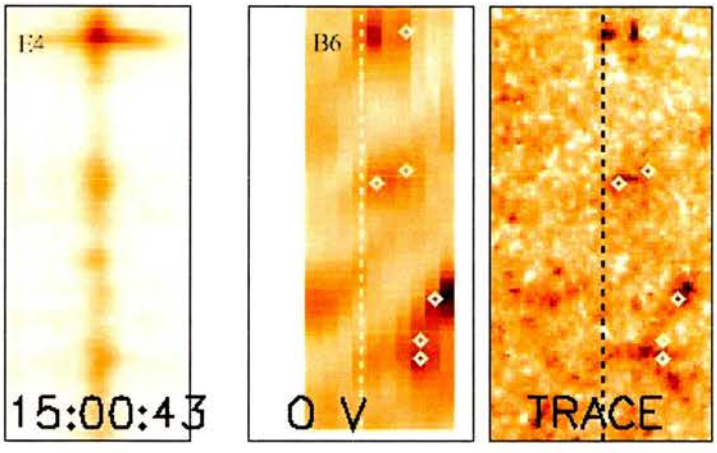

Figure 6.11: As Figure 6.1, but SUMER Si IV, CDS O V and simulated TRACE C IV data frames taken at time 15:00

t1 and t2, but the CDS region does not show an increase of similar magnitude. Figure 6.12 (c) and (d) show the SUMER Si IV line profile for the explosive event, E4, and CDS O V line profiles for the B6 region, respectively. Both the amplitude of the SUMER and CDS line profiles increase from t1 to t2. More importantly though the SUMER line profile at time t2 is broader and has enhancements in both wings compared to the SUMER profile at t1. The wings show velocities of approximately 200 km s^{-1} in both directions. This is a signature of a bi-directional explosive event. The CDS line profiles show a Doppler velocity of -0.2 km s^{-1} between t1 and t2, which is below the resolution of CDS, but no evidence of any broadening. There is, however, a non-Gaussian component that has 3.0% of the flux of the whole profile and has a velocity of -138.0 km s^{-1}.

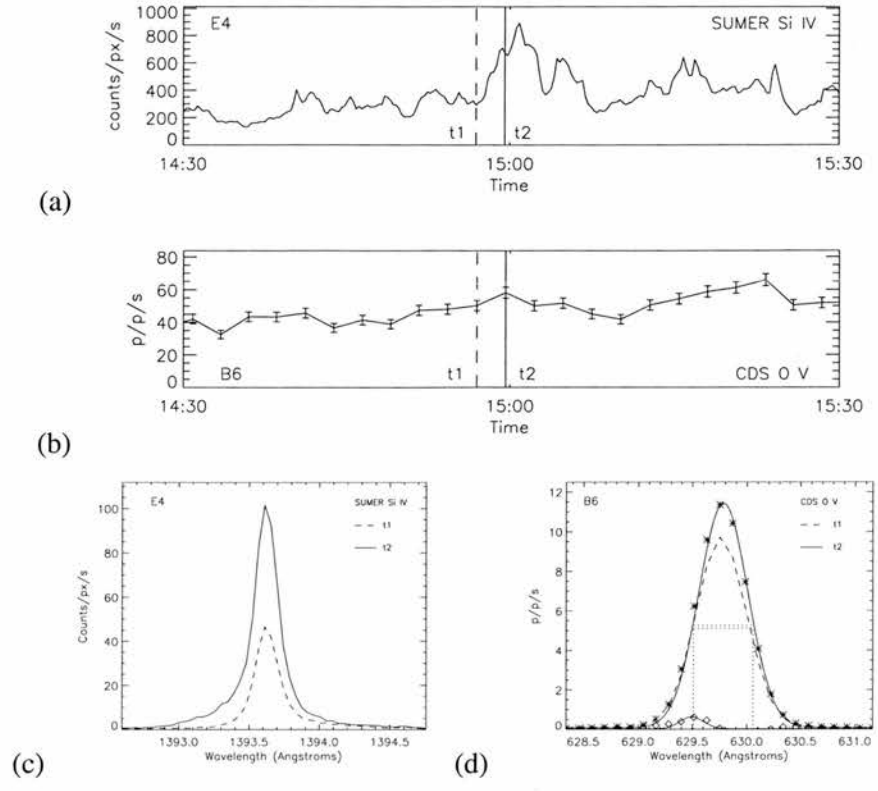

Figure 6.12: As in Figure 6.2, but for explosive event E4, and for CDS region B6

Figure 6.13 shows an intensity plot of wavelength versus time for CDS region B6. The variation of intensity in the plot follows the same trends as that seen in the lightcurve for the region in Figure 6.12. This region shows slight evidence of a broadening/wing enhancement on the blue side of the line profile just after the explosive event. In general, however, this region is narrower than the other examples.

6.4 Could blinkers and explosive events randomly coincide?

Let assume that blinkers and explosive events are random and not connected in any way. What is the chance that they can randomly occur in the same spot at the same time?

If we assume that the spread of blinkers throughout the CDS field-of-view is representative of the spread of blinkers in the SUMER slit, then the area-time volume of blinker pixels, V_b is 26395 arc sec^2 tp (where tp = the number of time pixels, and is equivalent to 151 seconds) and the equivalent for the whole of the CDS area-time volume, V_c, is 393743 arc sec^2 tp. The

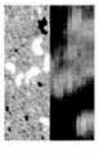

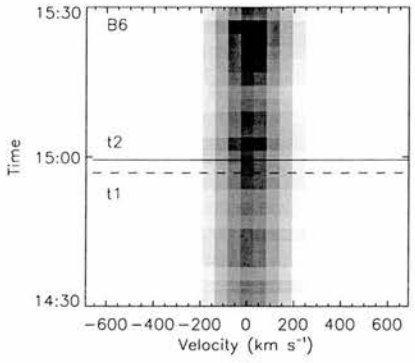

Figure 6.13: As for Figure 6.3, but for CDS region B6.

percentage of CDS space that contains blinkers, therefore, is 6.7%. We make this assumption, since the SUMER slit is not in a fixed location on the CDS raster, and moves throughout the data set.

Taking this as representative of the percentage of blinkers in the SUMER area-time volume, the probability, P_s, of a point (eg, centre of an explosive event) in the SUMER area-time volume coinciding with a blinker is given by

$$P_s = \frac{V_b}{V_c} \approx 0.067 \tag{6.1}$$

Multiple explosive events will give us a binomial distribution with probability of k explosive events being coincident with a blinker space is

$$P(k) = \binom{n_e}{k} P\left(e_k \notin V_b\right)^{n_e - k} P\left(e_k \in V_b\right)^k \tag{6.2}$$

where

$$P\left(e_k \in V_b\right) = P_s \tag{6.3}$$

and

$$P\left(e_k \notin V_b\right) = 1 - P_s \tag{6.4}$$

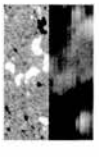

which gives

$$P(k) = \frac{n_e!}{(n_e - k)!k!}\left(1 - \frac{V_b}{V_c}\right)^{n_e - k}\left(\frac{V_b}{V_c}\right)^{k} \tag{6.5}$$

where, n_e is the number of explosive events and e_k is the kth explosive event.

Table 6.2 gives the probabilities of k explosive events occurring within a blinker using the data shown in Section 6.3, where we have 8 explosive events. Of these 8 events, there is one example of a blinker and an explosive event coincident, which the model suggests occurs at a probability of 0.33.

k	Expected probability	Experimental probability
0	0.57	0.875
1	0.33	0.125
2	0.083	0.0
3	0.012	0.0
4	0.0012	0.0
5	6.2×10^{-5}	0.0
6	2.2×10^{-6}	0.0
7	4.5×10^{-8}	0.0
8	4.1×10^{-10}	0.0

Table 6.2: Expected probability and experimental probability of k explosive events occurring within a blinker

For a binomial distribution, the mean is given by

$$\mu = n_e p_s \tag{6.6}$$

and the standard deviation is given by

$$\sigma = \sqrt{n_e p_s (1 - p_s)} \tag{6.7}$$

In our case, this gives a mean of 0.54 and a standard deviation of 0.71

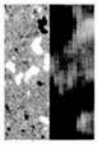

Our observations, however, have one coincident blinker and explosive event which is well within one standard deviation of the mean. We are unable therefore, to reject our hypothesis that explosive events occur randomly and independently from blinkers.

6.5 Conclusions

We have analysed a co-aligned SUMER and CDS data set and compared the locations of explosive events and blinkers. We have found three scenarios: one case where a blinker and an explosive event are coincident; 10 cases where there are lone blinkers and 7 cases where there are lone explosive events. We have also compared the lightcurves and line profiles of the Si IV and O V lines. In the majority of cases the profiles show the same characteristics, even though the two lines are formed at different temperatures (6.6×10^4 and 2.0×10^5 K, respectively). The lightcurves, however, do not show the same characteristics.

We find a significant Doppler velocity in the blinker where there is also an explosive event, but no significant broadening in any of the blinkers. As expected, both the SUMER explosive event line profiles had enhancements in the wings. But can we expect to see the same wing enhancements in CDS given that the resolution of the two instruments are different? To determine this, we assume that a theoretical line profile is comprised of two Gaussian profiles: one core Gaussian with amplitude A_1, line centre λ_1 and width σ; and one wing Gaussian with amplitude A_2, line centre λ_2 and the same width σ. For a given line shift (velocity) and amplitude of the wing Gaussian, we can calculate the fraction of the whole line profile that is made up of the wing component (i.e. the integral of the wing component divided by the integral of the whole profile).

Figure 6.14 shows a contour plot of the fraction of the line profile that is made up of the wing component. In the case of the explosive event, E1 and blinker, B2, the area of the SUMER explosive event is 0.12 times the area of the CDS blinker. If we assume that the whole of the plasma in the SUMER region is giving rise to the explosive event, then a velocity of 120 km s^{-1} (Figure 6.14 *dotted* line) would show up as a wing which has one fifth the flux of the whole profile. The whole of the SUMER region, however, will not contribute to the explosive event, and if we assume that only one fifth of the plasma in the SUMER region gives rise to the explosive event (i.e. 0.024 of the CDS blinker), then the wing will contribute less than a tenth of the whole profile. This is consistent with our results, where we find in both blinker and non-blinker cases,

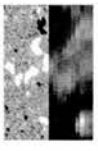

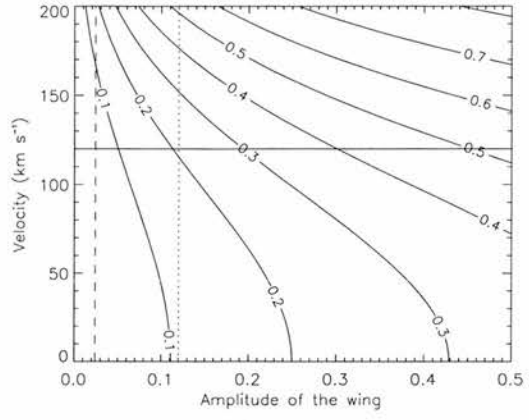

Figure 6.14: Contour plot of the fraction of the profile made up of the wing Gaussian when the amplitude and the velocity of the wing Gaussian are varied. The *solid* line marks the 120 km s^{-1} velocity of the SUMER explosive event E1, and the *dotted* and *dashed* lines mark the amplitude expected from the whole and a fifth of the SUMER explosive event producing the 120 km s^{-1} velocity observed, respectively.

less than a tenth of the line profile was made up of the wing component. Only in blinkers, did we find significant velocities associated with these wing enhancements.

From Figures 6.2 (c), 6.4 (c) and (d), 6.7 (c), 6.9 and 6.12 (c), we have to question whether the wing enhancements observed in CDS line profiles are significant. The wing enhancements all have similar magnitude and the same direction of velocity as those seen in SUMER, but the flux present in the wing is not significant compared with the core. The spectral resolution of CDS maybe preventing us from accurately repeating the analysis carried out by Innes (2001).

From our probability analysis, we would expect more blinkers and explosive events to be co-incident than our data has suggested. It is possible that we have missed some short duration explosive events in the 151 second cadence of the CDS data. We cannot, however, reject our initial hypothesis that explosive events occur randomly and independently from blinkers. There are not, however, enough events for this result to be statistically significant, and further analysis of other co-aligned SUMER and CDS data sets are needed.

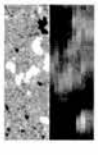

Chapter 7

Discussion and Future Work

7.1 Thesis summary

In Chapter 2, we discuss the general properties of QS blinkers identified with BLIP. They have typical areas of 3×10^7 km^2, lifetimes of 16 minutes, global frequency of 7 s^{-1} and intensity enhancement factor of 1.8. We also investigate QS blinker signatures in other wavelengths, and find that they are most easily identified in the O V emission line, but they have signatures in cooler transition region and chromospheric lines, but not in hotter coronal lines. Analysis of blinker line ratios shows that blinkers are either density or filling factor enhancements, but not temperature enhancements. We also find that blinkers are preferentially located above regions of strong chromospheric, transition region and coronal emission, such as network boundaries.

In Chapter 3, we identified AR blinkers in an active-region data set, and find their areas and lifetimes to be approximately the same as those for QS blinkers. The global frequency and intensity enhancement factors of AR blinkers, however, are found to be greater than QS blinkers. As in the case of QS blinkers, we find that AR blinkers have signatures throughout the transition region and chromosphere, but unlike the QS blinkers, AR blinkers also have occasional signatures in coronal lines. Using line ratios, we confirm that like QS blinkers, AR blinkers are density or filling factor enhancements and not temperature enhancements. When comparing blinkers with active region emission, we find that they were preferentially located above regions of high emission.

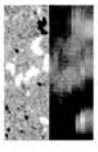

In Chapter 4, we investigate the Doppler and non-thermal velocities of the O V blinkers and the chromospheric plasma beneath. The Doppler velocities found have a preference to be more red-shifted than the normal chromosphere and transition region, but the range of these enhanced shifts are no larger than the typical spread of Doppler velocities in these regions. Furthermore, the non-thermal velocities are preferentially larger than the typical background chromosphere and transition region. Again the increase in magnitude of the non-thermal velocities is no greater than the typical range.

In Chapter 5, we investigate the photospheric magnetic field beneath blinkers using SOHO/MDI data. We find that blinkers are preferentially located above regions of single dominant polarity magnetic field, and in the AR data set, we find blinkers both above plage, umbral and penumbral regions. We also compared the strength (where only one polarity is present) or ratio of magnetic field (where both polarities of field are present) with blinker properties. We find no correlation between blinker area, lifetime or peak factor with either the strength of magnetic field or the ratio of magnetic field.

Finally, in Chapter 6, we make an initial comparison of blinkers and explosive events. We observed one case where a blinker and an explosive event are co-incident, 10 cases where there are blinkers only and no explosive events and 7 cases where there are explosive events only and no blinkers. An initial comparison of the SUMER line profiles of the explosive events and the CDS line profiles of the blinkers is made. Comparisons of the Doppler velocity, broadening and wing enhancements in the line profiles are also made. We find significant velocities in the CDS line profiles where a SUMER explosive event is present, but the proportion of the plasma in the pixel giving rise to this velocity is not significant. Initial probability analysis suggests that we cannot reject a hypothesis that explosive events occur randomly and independent of blinkers.

7.2 Discussion on blinkers and other phenomena

To determine whether blinkers might be related to other phenomena, we compare rates of occurrence and other properties of blinkers to those for other events in the photosphere, chromosphere, transition region and corona.

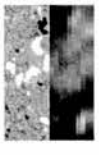

7.2.1 Comparison with other photospheric phenomena

First, let us compare rates of occurrence of blinkers with rates of occurrence of events, that occur in the photosphere near network regions, namely ephemeral regions and cancelling magnetic features. Ephemeral regions have a global frequency of 0.5 s^{-1} (Hagenaar, 2001), and the global frequency of cancelling magnetic features is 0.15 - 0.25 s^{-1} (Parnell, 2001) compared to a global frequency of 7.5 s^{-1} for $n_\lambda = 3$ and $n_p = 3$ QS blinkers. Clearly, both ephemeral regions and cancelling magnetic features occur far too infrequently to account for blinkers and their lifetimes are much longer than that of blinkers. These rates of occurrence suggest that it is not reconnection driven by emergence or cancellation that is causing blinkers, but they do not rule out the possibility that reconnection due to the passing of opposite polarity fragments might be a mechanism. Furthermore, we have found that in the quiet Sun, 39% of blinkers do not occur above regions of mixed polarity and that 59% of these lie above regions where one polarity is dominant. Equally in active regions, we have found that blinkers occur above the umbra and penumbra of a sunspot where reconnection is unlikely to occur.

7.2.2 Comparison with other chromospheric phenomena

Next, we compare blinkers with chromospheric spicules. The birth rate of spicules was estimated by Wilhelm (2000) to be 2×10^{-5} Mm^{-2} s^{-1}, which is equivalent to a global frequency of ≈ 120 s^{-1}. This is 15 - 20 times higher than the global frequency of $n_\lambda = 5$ and $n_p = 3$ QS and AR blinkers, but it may be possible that one blinker maybe made up of many spicules. Spicules also have plasma ejections of 20 - 30 km s^{-1} associated with them. We do not find any evidence of velocities of this magnitude in our investigation of chromospheric and transition region blinker line profiles, but if the time scale of these motions was on the order of the cadence of our data, them we may miss the blue shift of the ejection and the red-shift of the plasma falling down. The area of a spicule, however, has a wide range from 10^6 to 10^{10} km^2, which includes the range of blinker areas observed. The mean lifetime of spicules (15 minutes) is also very similar to the lifetime of blinkers and so a link between these two phenomena should not be ruled out.

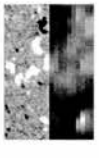

7.2.3 Comparison with other transition-region phenomena

Next, we will compare blinkers with other quiet-Sun transition-region phenomena. SUMER unit brightenings are both smaller in area and shorter in duration to blinkers and have been observed using single slit data that has a higher temporal and spatial resolution than the CDS rasters that are used to observe blinkers. We find, however, that only 7% of QS blinkers have lifetimes < 10 mins. The temporal resolution of CDS, which is ≈ 300 seconds and allows us to identify events with lifetimes as short as 5 minutes, is unlikely to cause the difference in the event durations. Analysis of blinkers in single slit SUMER data is impossible using BLIP, since we are looking for groups of pixels that all have significant increases in intensity at the same time. It is possible that blinkers are made up of many unit brightenings as suggested by Chae et al. (2000). Chae et al. (2000) also note that the line profile of SUMER unit brightenings are not as broad as an explosive event but do have significantly enhanced wings. As discussed earlier, blinkers may also have enhanced wings. A thorough investigation of SUMER unit brightenings and blinkers is needed with a co-aligned SUMER and CDS data set to determine whether a link exists. As part of this investigation, further comparisons of blinkers and explosive events can be made. As discussed in Chapter 6, there are many differences between blinkers and explosive events, particularly, the significance of the flows that are observed. More examples of blinkers with or without co-incident explosive events are needed to produce statistically signifcant results regarding any link there may be between the two phenomena.

Like SUMER unit brightenings, network and cell brightenings have both smaller area and shorter durations than blinkers, but like blinkers they are observed in both the chromosphere and the transition region. The differences in area and lifetime is probably due, however, to the single slit CDS data used to observe them. A thorough comparison of network and cell brightenings and blinkers is needed to determine whether a link exists between them and this possibility should not be ruled out.

Next, we will compare AR blinkers with other active region transition region phenomena. Since active transition-region brightening have a lifetime that is 30 - 40 times longer than that of blinkers, they are clearly not the same events. It is possible, however, that several blinkers could occur in one active transition-region brightening. Analysis of a data set including O IV (554 Å), O V (629 Å), Mg V (353 Å) and Mg VI (349 Å) would need to be undertaken to establish

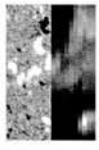

whether these events are connected. UV bursts on the other hand, are tending towards the lower end of the duration and size range of blinkers. They do, however, show both chromospheric and coronal signatures unlike many of the other phenomena discussed. Further analysis of properties of UV bursts, would provide more clues to whether these two events are linked.

7.2.4 Comparison with other coronal phenomena

Next we will consider other phenomena that occur in the corona. Although only our AR blinkers appear to have detectable coronal signatures we can still compare their frequency with that of nanoflares. From the results of Parnell and Jupp (2000) the occurrence rate of nanoflares appears to be between 2.3×10^{-21} cm^{-2} s^{-1} and 7.8×10^{-21} cm^{-2} s^{-1} which is equivalent to a global frequency of 100 - 500 s^{-1}. This is significantly greater than the number of AR (and QS) blinkers observed. The coronal signatures of blinkers are very similar to those found in nanoflares (i.e. peaks in intensity) and, therefore, if the blinkers with coronal events that we observe with peak factors greater than 3 are actually nanoflares our results suggest that at least 15% of AR blinkers could be associated with small nanoflares. Reconnection has been suggested as a mechanism that powers nanoflares, but this is unlikely to be responsible for blinkers since they do not always occur above regions of mixed magnetic field. This possible association is rather strange since nanoflares are believed to be heating events (Krucker and Benz, 1998; Parnell and Jupp, 2000; Aschwanden et al., 2000a,b) and yet we have found from line ratios that O V blinkers are not temperature enhancements. Clearly, before any firm conclusions about the connection between nanoflares and blinkers can be reached a proper investigation comparing CDS and TRACE or EIT images needs to be made.

Network flares have been observed in the quiet Sun corona at temperatures of 1.4 MK, and are believed to have a global frequency of 0.3 s^{-1} and lifetimes of 10 minutes. They are described by Krucker et al. (1997) as having an area that is an order of magnitude smaller than ARTBs, which is smaller than QS blinkers. The frequency of these events is considerably lower than QS blinkers, which do not show any coronal signatures, but the area and lifetime are similar. A full comparison of blinkers and network flares could be made using CDS and SXT images.

AR blinkers and ARTBs appear to be of a similar size, however, ARTBs tend to have shorter lifetimes than AR blinkers. It is possible that this difference may be due to the low time resolution

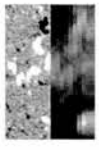

of 2.5 minutes of our data meaning that the shortest blinker lifetime that we can observe is just 5 minutes. The average lifetime of the blinkers, however, is 17 minutes with only a few ($\approx 7\%$) of blinkers having lifetimes less than 10 minutes and so the difference in lifetime is unlikely to be due to temporal resolution effects. Clearly, since we have only looked at a small section of an active region it is difficult to compare frequencies of events, however, the global frequency of blinkers (13 s^{-1}) is considerably larger than that of ARTB's (0.05 s^{-1}). Furthermore, ARTBs are not generally seen inside sunspots but more around their edges or in plage regions, unlike AR blinkers. Since we have not calculated the energy of our blinkers it is hard to compare blinker energies with those of ARTBs.

Walsh et al. (1997), however, indicate that one of the AR blinkers they found had energies of just 3×10^{27} ergs in He I, 3×10^{25} ergs in O V, 2×10^{24} ergs in Mg IX and 3×10^{24} ergs in Fe XVI. These energies are probably at the small end of the spectrum of energies estimated for ARTBs and no conclusions can be formed from a single event.

From the GOES data it is possible to see that there were just 3 flares during our active-region observing period, 2 of which were GOES B2 level and one of which was GOES B9. From the data it is not possible to say where the largest of the GOES flares originated, however, the other two flares were seen over AR 8243 which is the active region we observed. This suggests that the ARTB activity may have been fairly low, whereas we see quite a few AR blinkers. Furthermore, AR blinkers are thought to be density or filling factor enhancements whereas ARTBs are temperature events. It is therefore hard to say whether there is a relation between AR blinkers and either ARTBs or their EUV counterparts and this possibility needs testing.

7.3 Discussion of possible blinker mechanisms

Considering the results from all our analysis, a number of possible mechanisms for blinkers can be suggested. These are:

- *Isothermal compression of pre-existing plasma along field lines to increase the density, but not the temperature. The compression would occur at a rate that is less than the thermal conduction time-scale, so that the temperature would be maintained at the same value.*

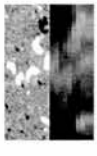

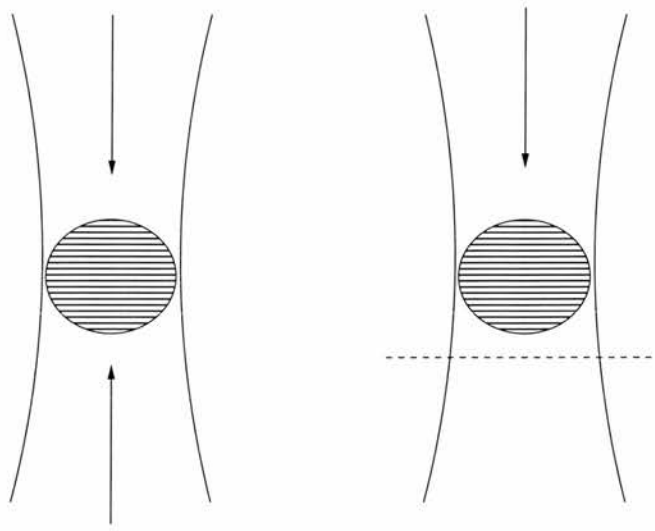

Figure 7.1: Cartoon illustrating two possible scenarios for isothermal compression along a field line

Isothermal compression is possible in both quiet Sun and active regions where mixed or unipolar field are present. A flow smaller than the conduction velocity which is based on the thickness of the transition region and the characteristic conduction timescale ($v \ll \frac{(\gamma-1)\kappa T^{5/2}}{2nk_B L} \approx 2.5$ km s^{-1}, where $\gamma = 5/3$, $\kappa = 10^{-11}$ W m^{-1} deg^{-1}, $n = 10^{15}$ m^{-3}, $L = 3 \times 10^4$ m, and $T = 10^5$ K) is needed so that the temperature would not be increased. This is consistent with the line-of-sight velocities that we have observed as long as the compression was along the line-of-sight. We cannot observe any flow or compression in the plane of the Sun.

- *The gathering together of field lines with pre-existing plasma at transition region temperatures to increase the filling factor.*

Blinkers typically occur above sites of strong magnetic field and so movement of these fields could be achieved by simply moving the other extended footpoints around. Due to the canopy effect any squeezing is likely to effect the chromospheric and transition region plasma more than plasma in widely spaced field lines at coronal temperatures. Modelling of the magnetic footpoints below blinkers would help us determine if this mechanism is likely. This type of squeezing is possible both in the quiet Sun and within sunspots where the magnetic field is continually being squeezed and buffeted by the convection motions below.

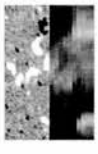

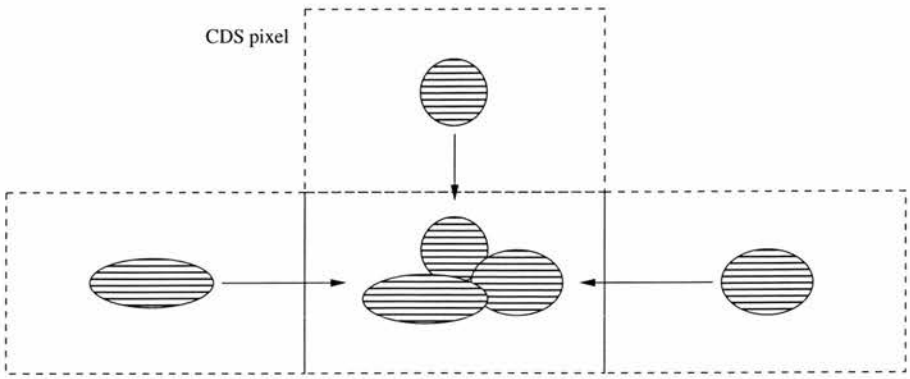

Figure 7.2: Cartoon illustrating the gathering together of field lines to increase the filling factor

If we assume that plasma moves from neighbouring CDS pixels in to a central pixel to increase the filling factor (Figure 7.2), it has to travel a maximum distance of 2 900 km (1 CDS pixel). For the movement of plasma to be responsible for a blinker, it must move within the rise phase of the blinker, i.e. approximately 8 minutes. So the velocity of the flow of plasma would be approximately 6 km s^{-1}. This is consistent with the flows that we observe and is also comparable to the velocity of granular motions producing the movement.

- *The distant reconnection of field lines that extend from a magnetic fragment below a blinker causing a 'sling shot' effect. During a 'sling shot' motion, field lines that start off almost perpendicular to the line of sight, may become parallel to the line-of-sight before ending up perpendicular once more causing an increase in the line of sight density.*

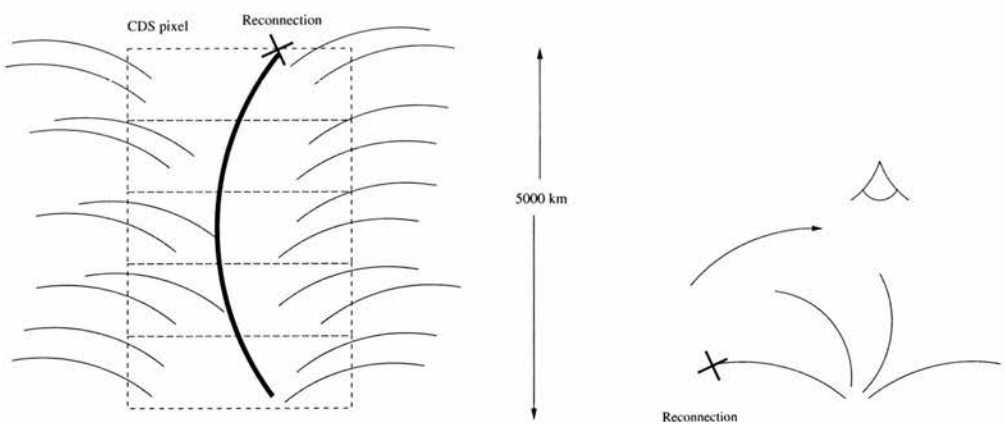

Figure 7.3: Cartoon illustrating the sling-shot effect of field lines

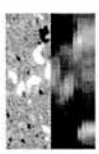

If we assume that we are observing 5 CDS pixels with size 3 000 $\times$ 1 000 km, and a 5 Mm loop is lying along the y-direction of these five pixels, and each pixel has 4 other loops contributing to the total emission emitted, then each pixel will have 5 units of emission (Figure 7.3). If we cut (or reconnect) one of the footpoints of the 5 Mm loop, and it moves up so that it is standing up vertically in the first pixel, that pixel will now have 9 units of emission, and the other 4 pixels will each have 4 units of emission. This produces an intensity enhancement factor of 1.8 in the first pixel as required for a blinker but it also suggests that a dimming would be present for the surrounding pixels. The velocity of the "cut" or reconnnected loop will be approaching the local Alfvén speed ($\approx$ 1 000 km s^{-1}) which suggests a time of 5 seconds to travel the 5 000 km distance of the 5 CDS pixels.

Although the actual crossing of the field lines may happen very fast, the time to reconnect all the field lines from one fragment may last several minutes and maybe long enough to account for a blinker. Comparing CDS rasters of blinkers and TRACE or Yohkoh images of loops would help decide if this was a likely mechanism. The idea of distant reconnection is unlikely as a cause for blinkers that are above sunspots, since, although the field lines that extend out from a sunspot will undoubtedly have distant connections in, say, another sunspot and these field lines may well reconnect, the field lines in the sunspot will always be predominantly vertical and therefore there is unlikely to be any change from any 'sling-shot' motion.

Recently, a paper by Priest et al. (2002) considered alternative mechanisms for blinkers. They mentioned the following mechanisms:

- *The compression of spicular material*

The compression of spicular chromospheric material which is ejected with velocities of 20 - 30 km s^{-1} and reaches coronal heights before being heated and falling back down to the chromosphere. The presence of this spicular material at transition region temperatures could give rise to a blinker.

As discussed previously, there are more spicules (100 - 200 s^{-1}) than either QS or AR blinkers on the Sun. Also, our velocity results do not show the magnitude of velocities required for spicules, however, if the rise and fall of spicular material occurs on the timescale of the cadence of our data, and we were unlucky with the timing, then we may miss the separate rise and

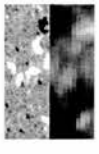

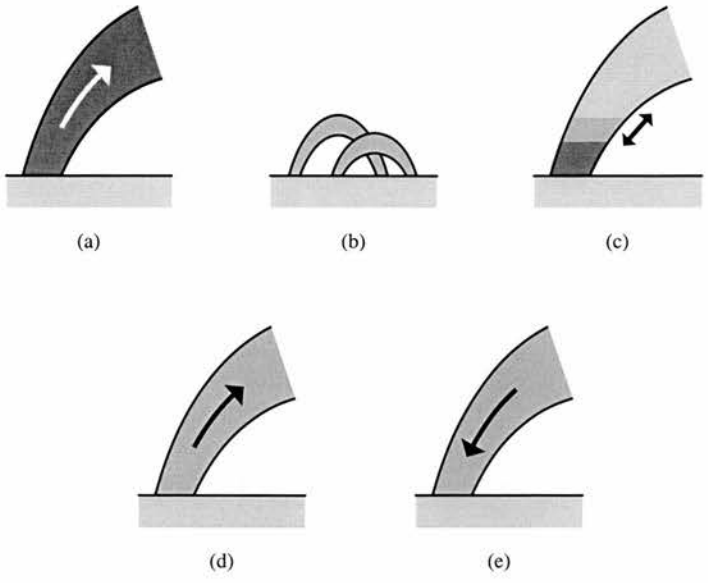

Figure 7.4: Cartoons illustrating the five blinker mechanisms suggested by Priest et al. (2002). (a) Heating of spicules, (b) Low-lying cool loops, (c) feet of coronal loops, (d) Heated and evaporating plasma and (e) Cooled and draining plasma

fall of plasma and simply observe a zero net velocity, which is consistent with our results. This suggestion cannot be ruled out, as many of the characteristics of blinkers and spicules are similar. A comparative study of Hα data and CDS O V data would be needed to determine if there is a link between the two phenomena.

- *Granular compression of cool low-lying loops: It is possible for short (5 Mm) loops to remain filled with plasma at temperatures of* 10^5 *K for several minutes - these could be blinkers.*

The presence of blinkers above unipolar regions is suggestive of field lines longer than 5 Mm rather than very short ones. Also considering the size of blinkers many short field lines would be needed which would seem to suggest a fairly obvious opposite polarity fragment should be present. Furthermore, the suggestion that blinkers are cool, short, low-lying loops does not fit with our observations of blinkers in a large sunspot where such field lines are unlikely to occur. In order to move the plasma to compress the short loops, one would expect a flow with a

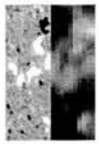

magnitude less than the horizontal granular velocity, 0.25 km s^{-1}, (Priest, 1982) to be present, which is consistent with the Doppler velocities found.

- *Compression of the coronal base of hot loops: The movement of the thin layer of plasma at the base of loops that lies between coronal and chromospheric plasma - this could give a blinking effect.*

This possibility needs to be tested by comparing CDS rasters with TRACE or Yohkoh SXT images of hot loops. Furthermore, high resolution images would give a better idea of the coronal structures above the blinkers, and would, indeed, show if blinkers even had signatures at these hotter temperatures. A small Doppler shift of a few km s^{-1} would be expected if the movement of the layer was upwards, and then a Doppler shift of no more than the free fall velocity, $\approx$ 12 km s^{-1} would be expected if the layer were moving downwards, which is consistent with our velocity results.

- *Heating and evaporating plasma: Plasma that passes through 10^5 K whilst being heated from chromospheric to coronal temperatures following heating and evaporation may be observed as a blinker.*

If this mechanism were to be correct, a large blue-shift of the order of the evaporation rate, few 100 km s^{-1}, ($v = \frac{2\kappa T^{5/2}}{5nk_BL}$ where $\kappa = 10^{-11}$ W m^{-1} deg^{-1}, $n = 10^{15}$ m^{-3}, $L = 5 \times 10^5$ m, and $T = 10^6$ K) would be expected, which is not consistent with our observations. One would also expect a consistent coherent flow that we do not observe. Furthermore, we see no delay in the onset, time of peak or end of a blinker in the different wavelengths which would be seen if the plasma were rising through the atmosphere. This may be due to the fairly low cadence (3 minutes) of our observations or may be because there is no time lag.

- *Cooling and draining plasma: Plasma that is cooling down from coronal to chromospheric temperatures and passing through 10^5 K could also be observed as a blinker.*

Similar arguments to those above for the heating of plasma apply. If this were the case, a time delay in the blinker signature would be expected in different wavelengths but the cadence of our

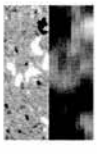

observations may prevent us from observing this. A red-shift of magnitude smaller than the free fall velocity (15 km s^{-1}) would also be expected. This is consistent with our velocity results.

From the results in this thesis, we are unable to determine exactly which of these mechanisms is the most likely cause of blinkers. If we consider all the results, the following four mechanisms cannot be ruled out and require further investigation in the ways described:

- The gathering together of field lines to increase filling factor
- The flipping of fieldlines due to distant reconnection
- Compression of cool low lying loops (Priest et al., 2002)
- Compression of the coronal base of hot loops (Priest et al., 2002)

7.4 Future work

As described previously, in order to determine the link between blinkers and many of the other phenomena discussed in Section 1.5, further investigation is needed with different types of data from different instruments not used in this thesis. Here, we describe four projects that would further the work completed here.

7.4.1 Blinkers in coronal holes

Initial analysis of a CDS O V data set in a polar coronal hole region shows evidence of blinkers. Before we can use BLIP to identify and determine the properties of these blinkers, we first must derotate and 'straighten out' the data taking into account the curvature of the observed region. There is no physical region why blinkers should not be visible in a coronal hole and the analysis of coronal hole blinkers will complete the study of blinkers in the three distinct regions of the Sun. A comparison of blinkers in these three regions will give us insight into the structure of the global transition region.

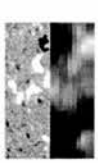

7.4.2 Further magnetic field studies

The analysis of the photospheric magnetic field beneath blinkers discussed in Chapter 5 was only of the magnetic field directly below the blinker at the time of its peak. A more detailed study would involve the identification of individual magnetic fragments beneath blinkers and investigating the dynamics and interactions of those fragments during the lifetime of the blinkers. This would provide information about the movement of the magnetic field in the vicinity of blinkers and also about the mechanism that causes blinkers.

7.4.3 Coronal blinker signatures

Observations of the corona, using either TRACE and/or EIT and SXT data, above blinkers is essential to furthering a number of aspects of the present study. Comparison of blinkers and coronal data will enable us to determine whether blinkers occur at the top or at the footpoints of coronal loop structures. A comparative study of blinkers and a coronal heating event, e.g. nanoflares or active-region transient brightenings would also be possible. This would provide information about the coupling of the solar atmosphere and in particular the transition region and the corona.

7.4.4 Further explosive event studies

As discussed in Chapter 6, we need to find several more data sets in which blinkers and explosive events can be identified to obtain a sufficient numbers of events so such comparative studies are statistically significant. A comparison of the underlying magnetic field of these events would also provide a unique insight to the links between the two phenomena. Further investigation of wing enhancements in CDS data is also needed.

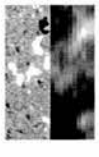

Appendix A

BLinker Identification Program, BLIP

BLIP is the top level program that analyses CDS data and automatically identifies blinkers. Its structure is illustrated in Figure A.1.

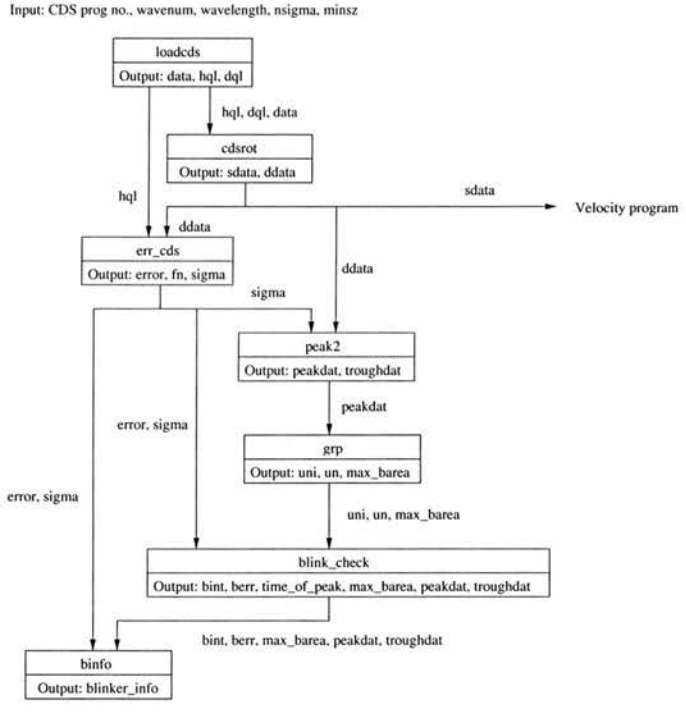

Figure A.1: A flow diagram to illustrate the structure of *BLIP*

BLIP contains many smaller functions/programs that each do a specific task that all contribute to the analysis. Several keywords are required as inputs to BLIP and these are:-

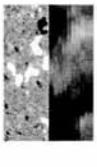

- The CDS program number. (e.g. 11484)
- The wavelength of data to be extracted and analysed. (e.g. HeI, OIII, OIV, OV, MgIX, MgX)
- *Wavenum*, wavelength window number
- The level of the error, *nsigma*, e.g. 3, 5 or 10
- The minimum number of pixels in a blinker, *minsz*, e.g. 1, 2, or 3

A.1 Loadcds

The *loadcds* function reads in the CDS fits files, prepares and calibrates the data and returns *hql*, *dql* and *data*. The function structure is illustrated in Figure A.2.

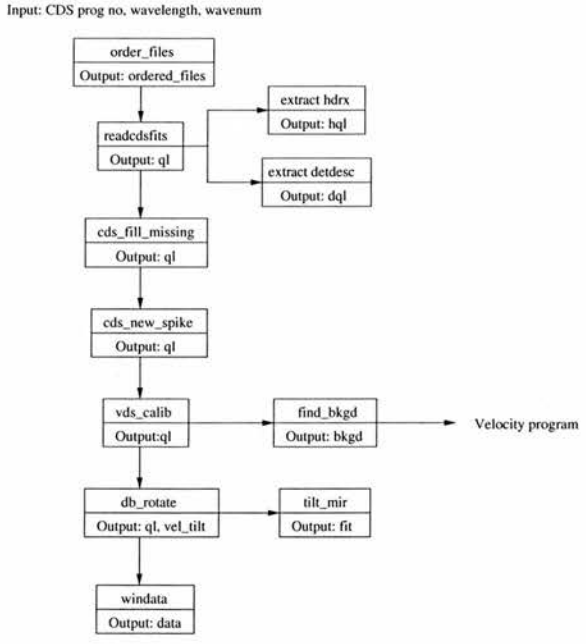

Figure A.2: A flow diagram to illustrate the structure of the *loadcds* program

The fits files are organised in numerical order by the *order_files* function, which enables the data to be read in chronological order into a 4D data array. This may appear to be trivial but one needs to take into account that some files do not exist and also the way they are listed on the Unix system is not in numerical order. This procedure ensures that the data array returned has all the correct images in the correct order.

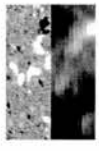

The *readcdsfits* command then reads in the files and extracts the quicklook data structure, *ql*. From this, *hql* and *dql*, the hdrx and detdesc parts of the header structure, are extracted. These two structures contain the essential information about the data which is used throughout the rest of the analysis.

The following procedures are then used to prepare and calibrate the data:

- *cds_fill_missing*: fills missing pixels.
- *cds_new_spike*: removes cosmic rays.
- *vds_calib*: calibrates the data, including correction for the CCD bias as a function of read-out quadrant, images are divided by the appropriate parts of the flat field image, the exposure time is corrected and divided into the data and finally, the data is converted from ADC (Analogue-to-Digital Conversion) counts to photon-events.

The *find_bkgd* procedure calculates the average background data value which is used when fitting the spectra to calculate velocities. The data is summed in the x and y directions to produce a 'super pixel' spectra. This spectra is fitted with a Gaussian (or skewed Gaussian, see Section B.3) function and the value of the background returned.

As well as the standard CDS data preparation detailed above, we perform a number of additional corrections that we have found to be necessary for the velocity analysis undertaken later.

The *db_rotate* procedure is a copy of the sswidl *nis_rotate*, which corrects for the tilt between the spectrometer slit and the CCD detector, which causes a N-S bias along the slit. The *nis_rotate* procedure uses a constant value for the tilt correction. Further work (see Section B.5) has shown that the tilt varies in time, and so we calculate a tilt value for every raster and correct them individually. The tilt is calculated by summing the data in the x-direction and fitting the spectra in the solar-y direction. The variation of the line centre position along the slit is calculated and then divided by the width of the spectral pixel to give the tilt (pixels/pixel along the slit) for each raster.

BLIP has been designed for use with feature tracking data, i.e. data that follows the same piece of Sun for its whole duration. There are two methods for following the same piece of Sun, (i) move the internal mirror and (ii) move the 'legs' on the instrument.

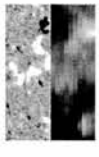

The data that we have analysed uses the internal mirror to follow the same piece of Sun. Two of our data sets, however, were long duration data sets (over 12 hours each), and the internal mirror reached its full movement, and so the mirror was reset and the legs were used in the feature tracking. This resetting of the mirror has been shown to cause a jump in the value of the tilt (see Section B.6). The *tilt_mir* procedure finds any jumps in the tilt and fits a polynomial function to the variation in the tilt which is used as the correction for the data. Within the *tilt_mir* procedure, the *times* function calculates the time difference in seconds between the first CDS image and subsequent images. The variable returned contains an array of times, *diffsec*. Finally, the *wavenum* input into *loadcds* specifies the wavelength of the data to be extracted by the *windata* command. The 4D data array, *data*, is of the form (*spectral pixel, xpixel, ypixel, time*).

A.2 CDSrot

The *cdsrot* function removes the effect of rotation of the Sun from the series of CDS images and is illustrated in Figure A.3.

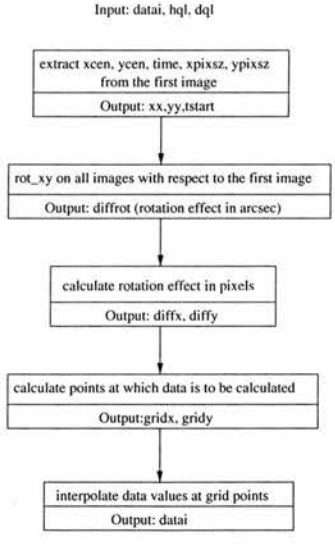

Figure A.3: A flow diagram to illustrate the structure of the *cdsrot* program

First a 3d data array, *datai*, for each spectral dimension of the 4d data array, *data*, is fed into the *cdsrot* program. The program extracts the distance from Sun centre to the centre of the each image in x and y in arc sec, *xcen* and *ycen*, respectively. The rotation effect of the Sun is

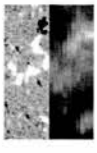

calculated by the difference in the value of *xcen* and *ycen* in subsequent images. The series of images is shifted back to the first image which is used as the reference point. The magnitude of the rotation of the images was found to be a fraction of a pixel, so interpolation was used to calculate new data values at the derotated positions for each image. The interpolation method used was a cubic convolution interpolation method that approximates a theoretically optimum sinc interpolation function using cubic polynomials. The program returns a 3d data set, *sdatai*, which is accumulated into a 4d data set, *sdata*.

This 4d data set is subsequently used to calculate the velocities of the blinkers. To proceed with the rest of the blinker identification program the 4d data is summed in the spectral dimension to produce a 3d data array, *ddata*.

A.3 Err_cds

The *err_cds* function estimates the error on each pixel and finds a global error, *sigma*, that is used when determining if a peak in the data is significant. The structure of the function is illustrated in Figure A.4.

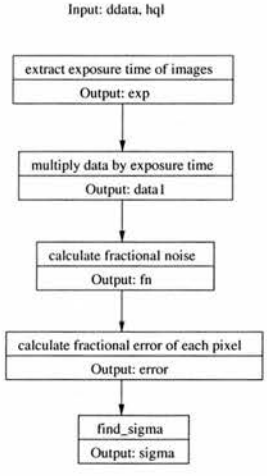

Figure A.4: A flow diagram to illustrate the structure of the *err_cds* program

The error on each pixel was estimated following the suggestions given in Thompson (1998). In *loadcds*, the data was calibrated using the routine *vds_calib* to convert the data to physical units of photons/pixel/second. The data is then multiplied by the exposure time to give the data in units of photons/pixel, denoted by N. The fractional noise, fn, is then calculated using the

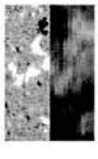

equation,

$$fn = \sqrt{2/N} \tag{A.1}$$

The fractional noise is then multiplied by the calibrated data to give the statistical error, *error*. The *find_sigma* procedure is then used to calculate the global error, *sigma*, of the data, which is defined as the value below which 99% of the errors exist.

A.4 Peak2

The *peak2* function locates peaks and troughs in the data and its structure is illustrated in Figure A.5.

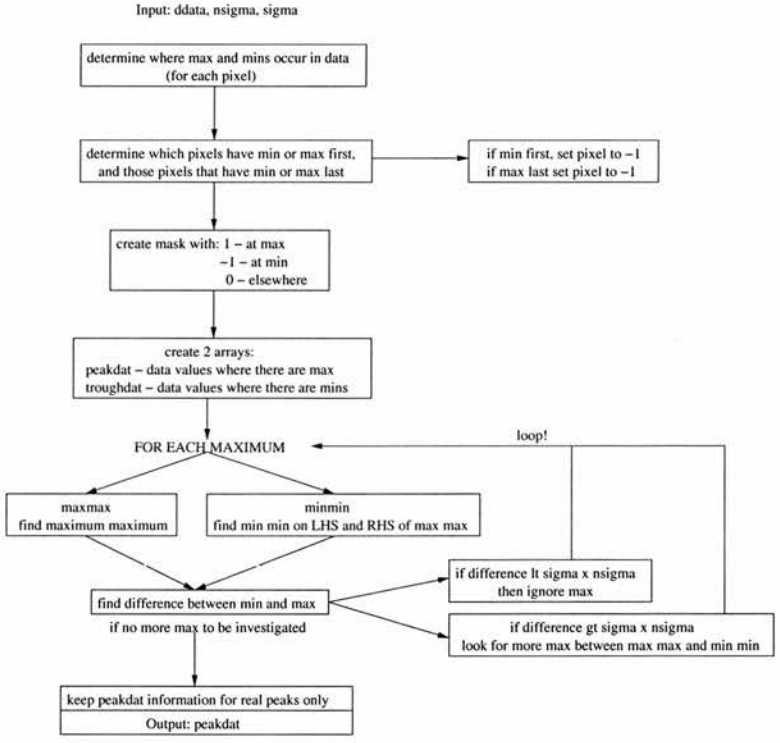

Figure A.5: A flow diagram to illustrate the structure of the *peak2* program

For each (x,y) pixel in the 3D data array the temporal maximum and minimums (peaks and troughs) of the data are identified. Each (x,y) pixel is then investigated to see whether the column of pixels starts with a maximum or minimum, or ends with a maximum or minimum. This

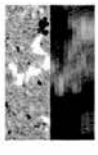

enables the identification of the start and end minimums and the first true peak. The function *maxmax* is then used to identify the position of the maximum peak lying between the temporal range for each (x,y) pixel and the value of that peak. The *minmin* function is then used to identify the position of the minimum troughs to the left hand side and the right hand side of the maximum and the value of these troughs.

If the drop in the value of the intensity jumps between the maximum peak and both minimum troughs is larger than a given threshold, *sigmadat* ($nsigma \times sigma$, both variables being specified by keywords) then the peak is kept. We then investigate the next maximum peak in the two ranges between the global maximum peak just identified and the two minimum troughs at either end of the temporal range. In both of these ranges the maximum peaks are identified and the minimum troughs on either side of these peaks are found. Again, if the jumps from the minimums to the maximums are big enough on both sides of the maximum then the maximum is kept and the range is divided into two yet again, see Figure 1.10 for an illustration. A 3D array, *peakdat*, containing the *ddata* values, where the significant peaks occur, and zeros elsewhere is returned.

A.5 Group

The *group* function groups the peak pixels identified in *peak2* and stored in *peakdat* into a blinker and its structure is illustrated in Figure A.6.

Integer values are given to all the pixels in *peakdat* where *peakdat* is not equal to zero. The *asignmentp* function (written by C.E. Parnell) determines the maximum unique value of a set of adjacent pixels and assigns that value to all the adjacent pixels in that set. A pixel $p_i = (x_i, y_i, t_i)$ is said to be adjacent to another pixel $p_j = (x_j, y_j, t_j)$ if $t_i = t_j$ and $x_j \in [x_{i-1}, x_{i+1}]$ and $y_i \in [y_{i-1}, y_{i+1}]$ and the value of the pixels (x_i, y_i, t_i) and (x_j, y_j, t_j) are both non zero. Furthermore, if $p_k = (x_k, y_k, t_k)$ is adjacent to p_j and p_j is adjacent to p_i then p_k is adjacent to p_i. Each set of pixels that are 'adjacent' are said to form a possible blinker. The 3D array *uni* contains the unique value of the pixels for each possible blinker and zeros elsewhere. The input keyword, *minsz*, specifies the minimum number of pixels in a blinker group. Any pixels belonging to groups with less than this number of pixels are set to zero. An array of all the unique group numbers in *uni* are also returned as *un* - the size of this array gives the number of

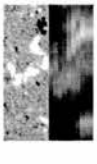

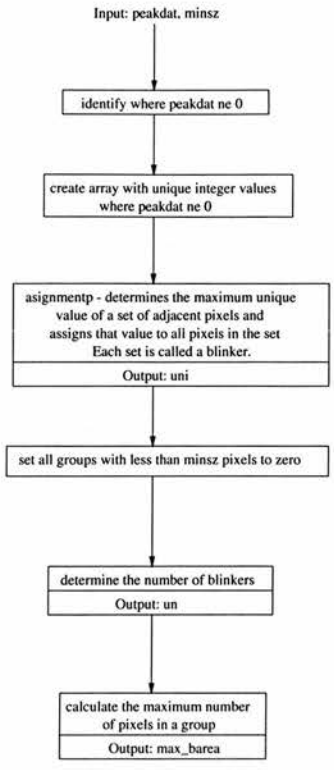

Figure A.6: A flow diagram to illustrate the structure of the *group* program

blinkers identified. The maximum blinker area, *max_barea*, is also identified from the maximum number of pixels with a given value of *un*.

A.6 Blink_check

The *blink_check* function checks that the blinkers have been correctly identified and finds the correct troughs for the peaks. The structure of the function is illustrated in Figure A.7.

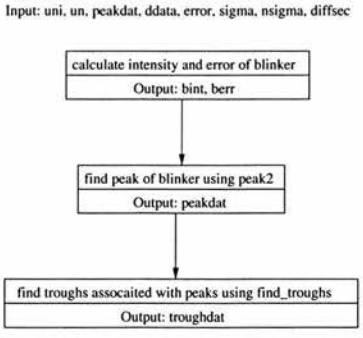

Figure A.7: A flow diagram to illustrate the structure of the *blink_check* program

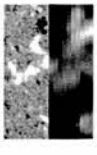

The intensity of the whole blinker, *bint* (units: photons/pixel/second) is calculated and the data array is fed into the *peak2* function again to determine the peak of the blinker. Once the intensity over the whole blinker has been summed, there may be occasions when a peak no longer occurs at the same time at which it was identified, hence the additional check. A new *peakdat* array is returned that contains the *ddata* values where there are peaks and zeros elsewhere.

A further function, *find_troughs* find the troughs associated with the peaks given in *peakdat*. We differentiate the blinker intensity curves with respect to time. This identifies the positions of the peaks and troughs by the change in sign of the derivative. For each blinker, we identify the nearest minimum (NM) troughs on both sides of the peak and decide whether they are in the correct position. We look at all the other troughs between the NM trough and the peak and calculate the increase in intensity from the troughs to the small peaks in between. If the change in intensity between the troughs and the small peaks is less than 2*sigma*, then the NM trough is correct. If the change in intensity is greater than 2*sigma*, then the nearer trough to the peak is correct. Finally, the intensity difference between the peak and the correct trough is checked to ensure that they meet the criteria for a blinker, i.e. that the intensity increase is still greater than *sigmadat*. An array, *troughdat*, containing *ddata* values where there is a trough and zeros elsewhere, is returned.

A.7 Binfo

The *binfo* function accumulates all the information you could possibly want to know about the blinkers and writes it to a structure array. The structure of the function is illustrated in Figure A.8.

Binfo creates a structure called *blinker* for each blinker identified by the *group* function which contains the following properties:-

- Area of the blinker, *area*
- Position of the centre of the blinker in arc sec from Sun centre, *xmid, ymid*
- Image number of the blinker peak, start and end, *time_of_peak, start_time, end_time*
- Array containing intensity curve of the blinker, *b_int*

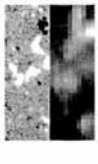

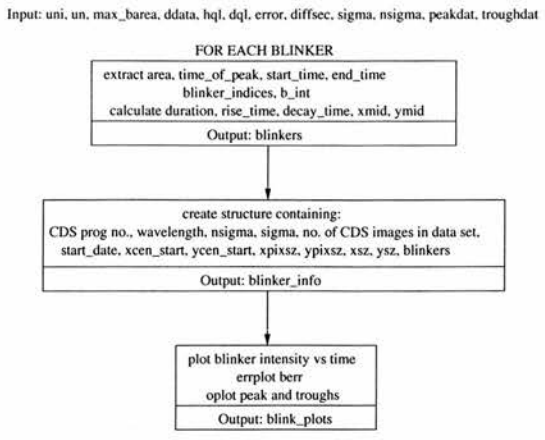

Figure A.8: A flow diagram to illustrate the structure of the *binfo* program

- Indices of the blinker pixels, *blinker_indices*
- Duration, rise and decay time of the blinker, *duration, rise_time, decay_time*

All of the *blinker* structures are then accumulated into another structure, *blinker_info* with the following global information:

- CDS Program Number, *cds_dir*
- Wavelength of data analysed, *wavelength*
- Value of sigma and nsigma, *sigma, nsigma*
- Start time and date of the data set, *start_date*
- Number of images in the data set, *cds_image*
- Position of the first image from Sun centre in arc sec, *xcen_start, ycen_start*
- x and y pixel sizes, *xpixsz, ypixsz*
- x and y image sizes *xsz, ysz*

Finally, the function plots intensity (photons/arc sec^2/second) vs time (seconds) graphs for each of the blinkers and overplots the error bars. The peak of the blinker is denoted by $*$ and the troughs indicating the start and end of the blinker are denoted by $\diamond$'s.

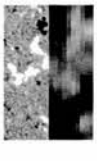

Appendix B

Determination of Velocities using SOHO/CDS

The spectral capabilities of SOHO/CDS (Harrison et al., 1995) enable us to determine the Doppler and non-thermal velocities of chromospheric and transition region plasma. We discuss the methods of calculating those velocities here.

B.1 Doppler velocity

The Doppler velocity, v, of an observed region of plasma is a velocity associated with mass motions and can only be observed along the line of sight. The Doppler formula determines the line-of-sight velocity, v, from the change in observed wavelength, with the convention that a velocity away from the observer is positive,

$$\frac{\delta\lambda}{\lambda_0} = \frac{\lambda_c - \lambda_0}{\lambda_0} = \frac{v}{c}\,, \tag{B.1}$$

where, λ_0 is the reference wavelength, $\delta\lambda$ is the change in wavelength and c is the speed of light. The observed wavelength, λ_c, is calculated by fitting a (Gaussian) distribution profile to the observed spectra (see Section B.3) and the reference wavelength determination is given in Section B.4

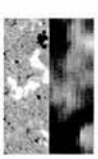

B.2 Non-thermal velocity

A non-thermal broadening is caused by turbulence or unresolved bulk velocity motions along the line of sight. The non-thermal velocity is determined from the width of the observed Gaussian line profile in comparison to the natural width of the line. All spectra have a natural width that is caused by instrumental, thermal and non-thermal broadening. Natural thermal Doppler broadening is caused by the motion of the observed atoms in different directions with different velocities with the resulting Doppler shifts producing a spread in the frequency of the observed line. The natural non-thermal Doppler broadening occurs due to motions that are unresolved spatially and/or temporally, for example, turbulence and Alfvén waves (Kitchin, 1995). The natural width of the line due to these affects can be calculated, and any additional non-thermal velocity of the plasma can be detected by an additional broadening of the line.

First, we will determine the natural expected width of the line. The full width half maximum, the wavelength separation between the points where the profile drops to half its maximum height on both sides of the line centre, is given by,

$$\text{Natural FWHM} = \sqrt{4ln(2)\delta\lambda_n^2 + \delta\lambda_i^2}\,, \tag{B.2}$$

where, $\delta\lambda_i$ is the instrumental width and $\delta\lambda_n$ is the natural width. As already mentioned, this natural width consists of thermal and non-thermal components, which are given by,

$$\delta\lambda_n = \sqrt{\delta\lambda_T^2 + \frac{\lambda^2}{c^2}\xi^2}\,, \tag{B.3}$$

where, $\frac{\lambda}{c}\xi$ is the non-thermal component and $\delta\lambda_T$ is the thermal component. The thermal component is equal to

$$\delta\lambda_T = \frac{\lambda}{c}\sqrt{\frac{2kT_i}{M_i}}\,, \tag{B.4}$$

where, k is Boltzmann's constant, T_i is the temperature of the ion and M_i is the mass of the ion.

It is assumed that the non-thermal width is of the same order of magnitude as the thermal width, and here we assume that they are equal. The instrumental part of the line width, however, usually

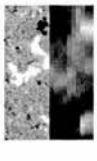

dominates both the thermal and non-thermal components of the natural width. The instrumental width (the width of the image on the detector) of the line is given by

$$\delta\lambda_i = d \times w \ , \tag{B.5}$$

where, d is the dispersion of the light with in CDS and w is the width of the Gaussian profile on the detector. The observed non-thermal velocity, v_{nt}, is therefore given by,

$$\frac{\sigma - \text{Natural HWE}}{\lambda_0} = \frac{v_{nt}}{c} \ , \tag{B.6}$$

where, σ is the thermal Doppler half width, which is the observed half width of the spectra derived from the fitted Gaussian parameters and the Natural HWE is given by

$$\text{Natural HWE} = \frac{\text{Natural FWHM}}{2\sqrt{2ln(2)}} \ . \tag{B.7}$$

B.3 Fitting spectra

Data taken with CDS before the loss of SOHO on the 25th June 1998 have spectral lines that can be described by a Gaussian profile,

$$G(\lambda) = A_0 \exp\left[-\frac{1}{2}\left(\frac{\lambda - \lambda_c}{\sigma}\right)^2\right] + background \ , \tag{B.8}$$

where, A_0 is the amplitude of the line, λ is the observed wavelength, λ_c is the line centre, σ is the Gaussian line width and $background$ is the constant background.

Figure B.1 shows an example of a pre-recovery O V line profile and the fit to it. The data points are plotted with $*$'s, the fit to the line with a *solid* line, the thermal Doppler half width, σ is plotted with a *dotted* line and the position of the line centre, λ_c, and the reference wavelength, λ_0, are plotted with a *dashed black* and a *dashed grey* line, respectively. The Doppler velocity of the plasma in this pixel is -10.5 km s^{-1} and the non-thermal velocity of the pixel is 5.1 km s^{-1}.

After the loss of SOHO, and due to the extreme temperatures that CDS encountered during that time, the line profiles have changed shape and acquired wings on both the red and the blue side

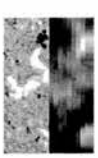

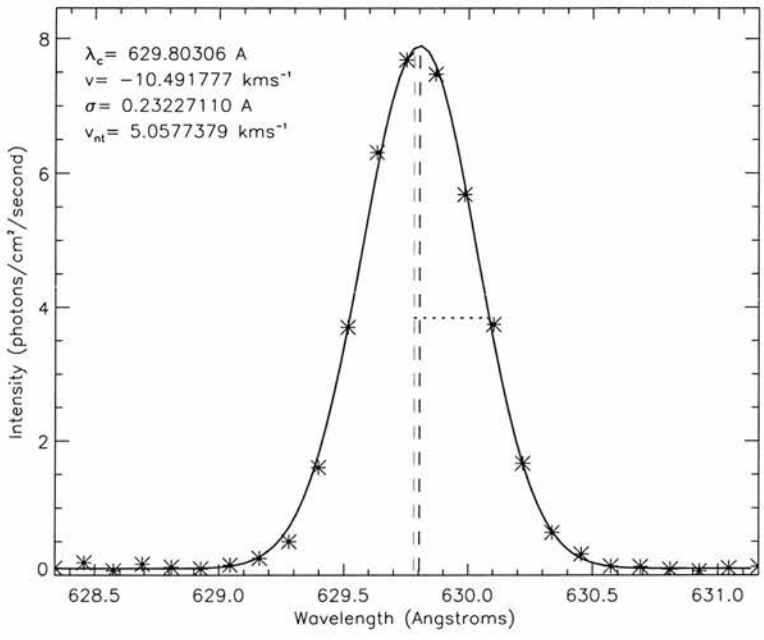

Figure B.1: Fitting Pre-Recovery Data

of the line profile. We do not use post-recovery data for velocity analysis in this thesis, since we found it was easier and more reliable to use pre-recovery data. We will describe the post-recovery data and our method for fitting these, however, for completeness. The new line profile has since been modelled as a combination of a Gaussian term plus a term describing the wings.

The Gaussian term is defined as in Equation B.8 and the wings are defined as,

$$W(\lambda) = \frac{\sigma'^2}{(\lambda - \lambda_c)^2 + \sigma'^2} , \tag{B.9}$$

where

$$\sigma' = 2\sigma\sqrt{2}\ln 2 . \tag{B.10}$$

The combined line profile is then described by,

$$B(\lambda) = A_0 \left[(1-\alpha)\, G(\lambda) + \alpha W(\lambda)\right] , \tag{B.11}$$

where

$$\alpha = \begin{cases} \alpha_r & \lambda \leq \lambda_c \\ \alpha_l/\alpha_r & \lambda > \lambda_c \end{cases} , \tag{B.12}$$

where, α_r is the relative amplitude of the right wing compared to the amplitude of the whole profile and α_l/α_r is the ratio of the amplitude of the left wing to the right wing.

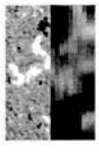

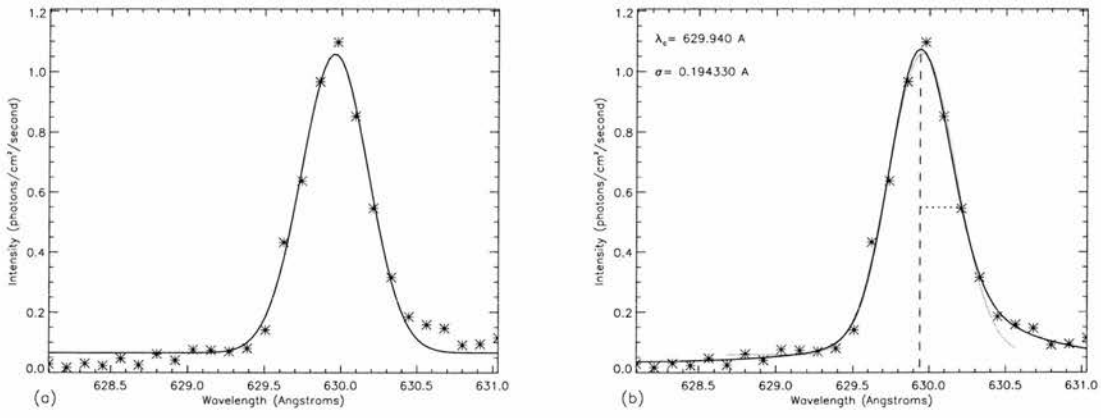

Figure B.2: Fitting Skewed Gaussian Spectra

Figure B.2a shows an example of a post-recovery O V line profile. The $*$'s mark the data points and the *solid* line shows the Gaussian fit to the data. As can be seen clearly in Figure B.2a, the Gaussian function does not fit the line profile well everywhere. Figure B.2b shows the same line profile but with a skewed Gaussian fit (*solid*), which clearly fits the profile better than the Gaussian function. To fit the post-recovery lines, we fit the middle of the line with a Gaussian function, fix the amplitude, A_0, line centre, λ_c and the line width, σ, and then fit the skewed Gaussian function. The Gaussian fit to the central part of the line is shown with a *grey* line in Figure B.2b. The width of the line is marked with a *dotted* line and the line centre is marked with a *grey dashed* line, respectively. This produced the best results for achieving good fits to the lines.

B.4 Calculation of the reference wavelength and width

We calculate histograms of the line centre position and the line width for each raster. The variation of the modal value of the histograms for each raster is then investigated. Figure B.3 shows the variation of (a) and (c) the Gaussian line centre position and (b) and (d) the line width parameters for the O V QS and AR data sets, respectively. Each graph shows the value of the line parameter of each raster, $*$'s and the fit to the points (*solid* line). The *dashed* lines show the 1σ confidence interval on the line parameters. The fit to the line centre position parameter is used as the reference wavelength to calculate the Doppler shift of plasma and not the laboratory wavelengths given in Kelly (1987). It has been found that the expected width of the line profile

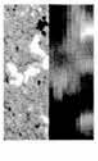

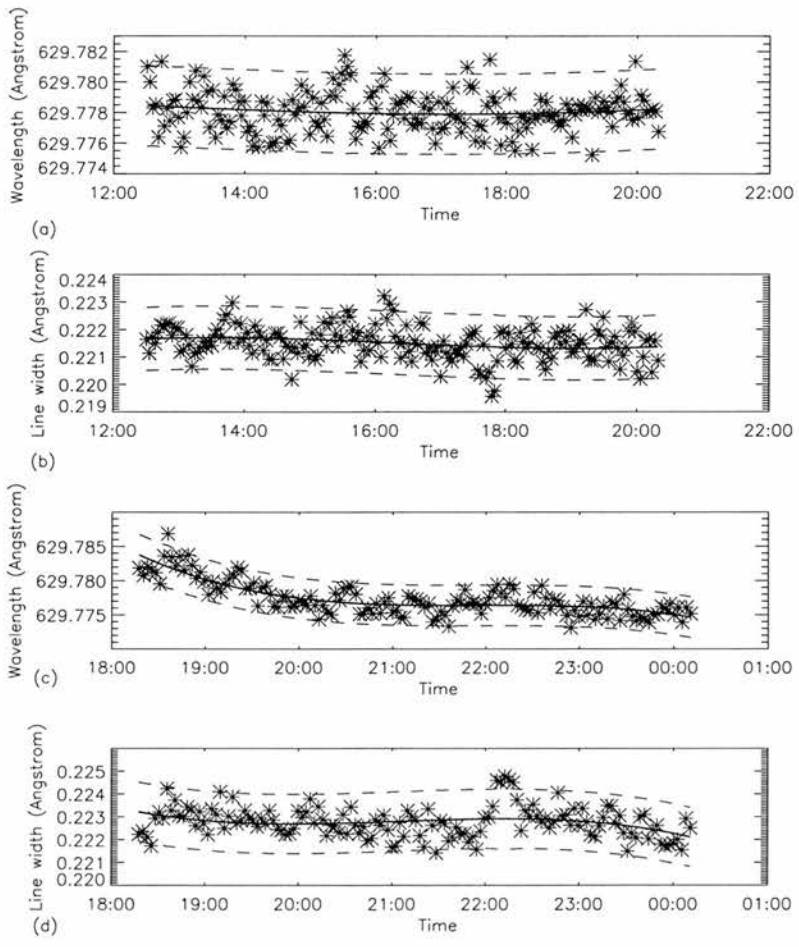

Figure B.3: Variation of O V line parameters with time; (a) quiet-Sun line-centre position, (b) quiet-Sun line width, (c) active-region line-centre position and (d) active-region line width. The $*$ mark the values for each raster and the *solid* line is the fit which is used for calculating the relative velocities.

is significantly smaller than the actual width of the line. For this reason, we use the fit to the line width as shown above as the expected width of the line profile when calculating the non thermal velocity.

B.5 Variation of NIS tilt

It is known that the dispersion axes of the NIS spectra are slanted relative to the CCD detector (x,y) axes. The track of constant solar Y is therefore not at a constant Y value in the data array, hence, causing a N-S bias along the NIS slit. This so-called 'tilt' can be accounted for and taken

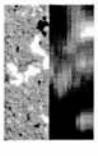

out using the *NIS_rotate* procedure from solarsoft. This procedure uses a constant value of the tilt as its calibration.

When preparing the data used in this thesis, the *NIS_rotate* command was used to correct the data for this effect, and the velocity maps created were analysed. It was apparent that *NIS_rotate*'s correction of the bias was not good enough to calculate velocities. The tilt correction was then investigated in greater detail.

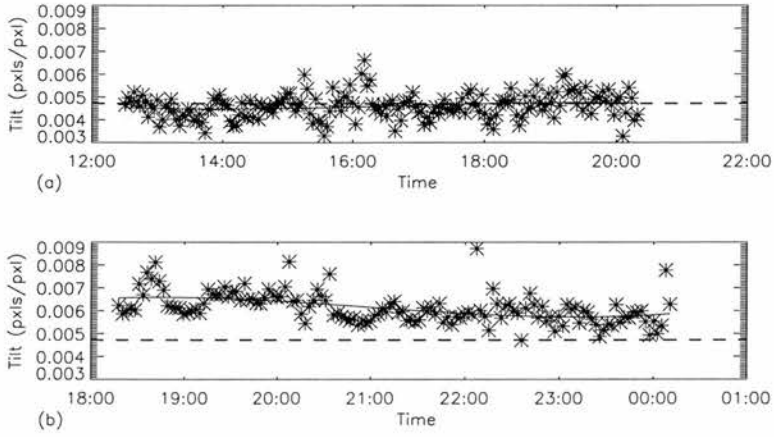

Figure B.4: Variation of NIS tilt with time during (a) the quiet-Sun data set and (b) the active-region data set. The $*$'s mark the data points, the *solid* line shows the new correction and the *dashed* line shows the constant value used by the *NIS_rotate* procedure.

From this analysis, it was found that the tilt was not constant, but varied both between data sets and during a data set. Figure B.4 shows the variation of tilt in time for the two data sets analysed in Chapter 4; (a) the quiet-Sun data set taken on 19th June 1998 and (b) the active-region data set taken on 18th June 1998. The $*$'s show the tilt value of each raster in the data set and the solid line shows the polynomial fit which is used as the new correction. On both graphs the constant value of the tilt used by the *NIS_rotate* procedure is plotted with a *dashed* line.

In the quiet-Sun data set this correction makes little difference (< 1 km s^{-1}) whilst in the active-region data set there is clearly a large difference between the standard and fitted tilt values. The variation of the tilt during the data set is equivalent to a maximum velocity of 8 km s^{-1} and, therefore, should not be ignored. The variation in the tilt is likely to be due to a number of factors including temperature, pointing and mirror position.

Figure B.5 shows the variation of NIS2 tilt with wavelength. The *dashed* and *solid* lines show

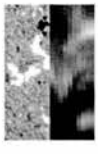

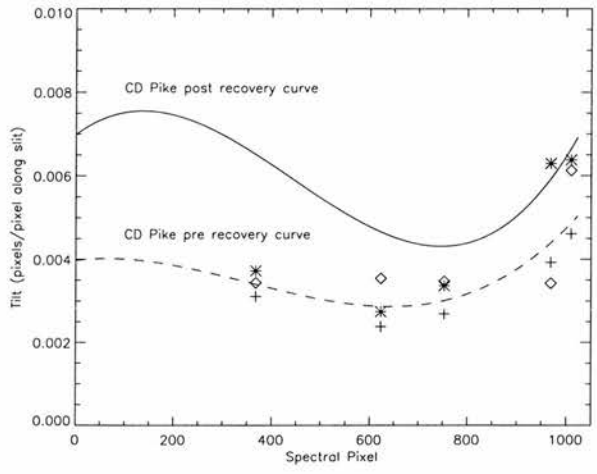

Figure B.5: Variation of NIS tilt with wavelength

the tilt correction values used by the *NIS_rotate* procedure for pre and post-recovery data, respectively. The symbols show the tilt correction values that have been calculated as part of the further investigation discussed above. The $*$'s, $\diamond$'s and $+$'s show the tilt correction for the quiet-Sun data set used in the Chapter 2 (post-recovery), the active-region data set used in Chapter 3 and 4 (pre-recovery) and the quiet-Sun data set used in Chapter 4 (pre-recovery), respectively.

B.6 Variation of NIS tilt with mirror position

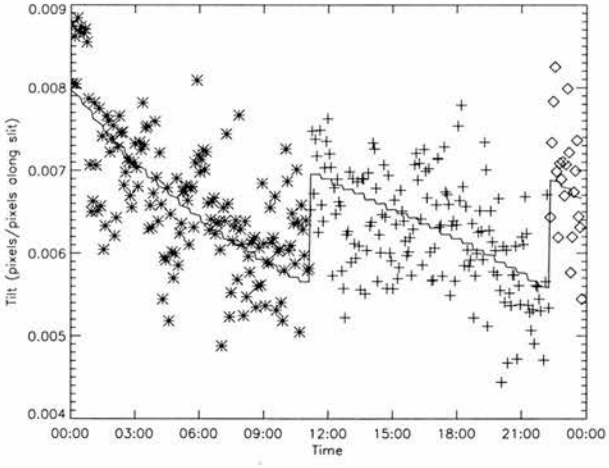

Figure B.6: Variation of NIS tilt with wavelength

The NIS variation also varies with the position of the mirror within the CDS instrument. The

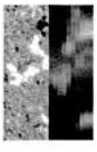

mirror is one way of tracking the same feature over a data sequence. If the sequence has a long duration, however, the 'legs' of the instrument are used when the mirror has reached its full extent, and the mirror is then reset. This resetting of the mirror has been shown to cause a variation of the NIS tilt. During our investigation of the NIS tilt, we investigated 2 long duration data sets that were designed to observe blinkers. We found that the tilt jumped when the mirror was reset. Figure B.6 shows the variation of O V tilt over the entire data sequence. The different symbols mark the data points that occur during a single passage of the mirror. The jump in the tilt can be seen and our fit to this is plotted with a *solid* line.

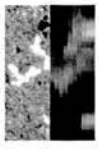

Appendix C

Contents of CD rom

The CD rom contains movies that illustrate both the data used and the analysis undertaken in this thesis. There is a web based interface that can be used to view the movies. The title page of this interface, index.html, contains links to all the movies.

C.1 Quiet-Sun CDS movies (Chapter 2)

The first movie, movie 2.1 shows the quiet-Sun CDS data analysed in Chapter 2. From left to right, the six frames show the He I, O III, O IV, O V, Mg IX and Mg X CDS rasters. The second movie, movie 2.2, is the same as movie 1, except mid-points of $n_\lambda = 5$ and $n_p = 3$ blinkers are over plotted on all the wavelengths with green $\triangle$s. The frames in movie 1 integrated with respect to time can be seen in Figure 2.5. The frames of the movie are taken 151 seconds apart.

C.2 Active-region CDS movies (Chapter 3)

The active-region CDS data analysed in Chapter 3 are shown in movie 3.1. As in the Chapter 2 movies, from left to right the six frames show the He I, O III, O IV, O V, Mg IX and Mg X CDS rasters, and movie 3.2 is the same but with the mid-points of the O V $n_\lambda = 5$ and $n_p = 3$ blinkers over plotted on all the wavelengths with green $\triangle$s. In Figure 3.4 the time integrated images of each wavelength from movie 1 can be seen. The frames of the movie are taken 151 seconds apart.

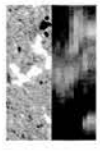

C.3 Quiet-Sun CDS movie (Chapter 4)

Movie 4.1 shows the quiet-Sun CDS data analysed in Chapter 4. From left to right, the six frames are the He I, O III, O IV, O V, Mg IX and Mg X data. This quiet-Sun data set is used in Chapter 4 since it is pre-recovery (data taken before the loss of SOHO on 25th June 1998) and is more reliable and easier to use for velocity analysis as the line profiles are basically Gaussian. The active region data set analysed in Chapter 4 is the same as that analysed in Chapter 3 (movie 1). The frames of the movie are taken 151 seconds apart.

C.4 Magnetic field movies (Chapter 5)

Movie 5.1 shows the quiet-Sun MDI magnetogram data analysed in Section 5.2 and the CDS O V data seen in Chapter 2, movie 1. Movie 5.2 is the same as movie 1, but has the O V $n\lambda = 5$ and $n_p = 3$ blinkers over plotted with red $\triangle$s. Stills from the MDI magnetogram movie with blinkers over plotted can be seen in Figure 5.1. The frames of the movie are taken 151 seconds apart. The maximum colour intensity limit is set for absolute fields of 40 Mx cm^2.

Similarly, movie 5.3 and movie 5.4 show the active region MDI magnetogram and white light data analysed in Section 5.3 and the CDS O V data seen in Chapter 3, with the O V $n\lambda = 5$ and $n_p = 3$ blinkers over plotted with red $\triangle$s, in movie 4. Again, stills from the MDI magnetogram and white light movie with blinkers over plotted can be seen in Figure 5.6. The frames of the movie are taken 151 seconds apart. The maximum colour intensity limit is set for absolute fields of 400 Mx cm^2.

C.5 Blinker and explosive event movie (Chapter 6)

Movie 6.1 shows the SUMER Si IV data, CDS O V data and simulated TRACE C IV data which are analysed in Chapter 6. The movie is courtesy of Davina Innes. The position of the mid-points of the blinkers and the SUMER slit can be seen over plotted on the CDS and TRACE data with $\diamond$s and *dashed* lines, respectively. The frames of the movie are taken approximately 150 seconds apart.

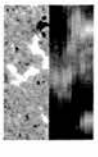

Bibliography

Achour, H., Brekke, P., Kjeldseth-Moe, O., and Maltby, P. (1995). Observed redshifts in the solar transition region above active and quiet regions. *Astrophysical Journal*, 453:945–952.

Aschwanden, M., Nightingale, R., Tarbell, T., and Wolfson, C. (2000a). Time variability of the "quiet" Sun observed with TRACE. I. Instrumental effects, event detection, and discrimination of extreme-ultraviolet microflares. *Astrophysical Journal*, 535:1027–1046.

Aschwanden, M., Tarbell, T., Nightingale, R., Schrijver, C., Title, A., Kankelborg, C., Martens, P., and Warren, H. (2000b). Time variability of the "quiet" Sun observed with TRACE. II. Physical parameters, temperature evolution, and energetics of extreme-ultraviolet nanoflares. *Astrophysical Journal*, 535:1047–1065.

Athay, R. (1976). *The solar chromosphere and corona: Quiet Sun*. Dordrecht, Holland.

Athay, R. (1984). Are EUV bursts members of the flare family? *Solar Physics*, 93:123–131.

Athay, R., White, O., Lites, B., and Bruner, E.C., J. (1980). Impulsive EUV bursts observed in C IV with OSO-8. *Solar Physics*, 66:357–370.

Berghmans, D. and Clette, F. (1999). Active region EUV transient brightenings - first results by EIT of SOHO JOP80. *Solar Physics*, 186:207–229.

Berghmans, D., Clette, F., and Moses, D. (1998). Quiet Sun EUV transient brightenings and turbulence. A panoramic view by EIT on board SOHO. *Astronomy and Astrophysics*, 336:1039–1055.

Berghmans, D., McKenzie, D., and Clette, F. (2001). Active region transient brightenings. A simultaneous view by SXT, EIT and TRACE. *Astronomy and Astrophysics*, 369:291–304.

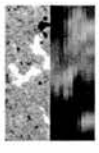

Brković, A., Solanki, S., and Rüedi, I. (2001). Analysis of blinkers and EUV brightenings in the quiet Sun observed with CDS. *Astronomy and Astrophysics*, 373:1056–1072.

Brueckner, G. and Bartoe, J.-D. (1983). Observations of high-energy jets in the corona above the quiet Sun, the heating of the corona, and the acceleration of the solar wind. *Astrophysical Journal*, 272:329–348.

Bruner, E.G., J. and Lites, B. (1979). Mass motions in impulsive flarelike brightenings as observed by OSO 8. *Astrophysical Journal*, 228:322–329.

Brynildsen, N., Brekke, P., Fredvik, T., Haugan, S., Kjeldseth-Moe, O., Maltby, P., Harrison, R., Pike, C., Rimmele, T., Thompson, W., and Wilhelm, K. (1998). EUV spectroscopy of the sunspot region NOAA 7981 using SOHO. II. Velocities and line profiles. *Solar Physics*, 179:279–312.

Chae, J., Schühle, U., and Lemaire, P. (1998a). SUMER measurements of nonthermal motions: Constraints on coronal heating mechanisms. *Astrophysical Journal*, 505:957–973.

Chae, J., Wang, H., Goode, P., Fludra, A., and Schühle, U. (2000). Comparison of transient network brightenings and explosive events in the solar transition region. *Astrophysical Journal*, 528:L119–L122.

Chae, J., Yun, H., and Poland, A. (1998b). Temperature dependence of ultraviolet line average doppler shifts in the quiet Sun. *Astrophysical Journal Supplement*, 114:151–164.

D'Agostino, R. and Stephens, M., editors (1986). *Goodness-of-fit techniques*, volume 68 of *Statistics: Textbooks and Monographs*. Marcel Dekker, Inc.

Dammasch, I., Wilhelm, K., Curdt, W., and Hassler, D. (1999). The Ne VII (λ770) resonance line: Solar wavelengths determined by SUMER on SOHO. *Astronomy and Astrophysics*, 346:285–294.

Dere, K. (1982). Extreme ultraviolet spectra of solar active regions and their analysis. *Solar Physics*, 77:77–93.

Dere, K. (1994). Explosive events, magnetic reconnection, and coronal heating. *Advanced Space Research*, 14(4):(4)13–(4)22.

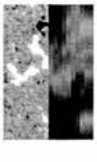

Dere, K., Bartoe, J., Brueckner, G., Dykton, M., and van Hoosier, M. (1981). Transient plasmas in the solar transition zone. *Astrophysical Journal*, 249:333–339.

Dere, K., Bartoe, J.-D., and Brueckner, G. (1989). Explosive events in the solar transition zone. *Solar Physics*, 123:41–68.

Dere, K., Bartoe, J.-D., Brueckner, G., Ewing, J., and Lund, P. (1991). Explosive events and magnetic reconnection in the solar atmosphere. *Journal of Geophysical Research*, 96:9399–9407.

Dere, K. and Mason, H. (1993). Nonthermal velocities in the solar transition zone observed with the High-Resolution Telescope and Spectrograph. *Solar Physics*, 144:217–241.

Domingo, V., Fleck, B., and Poland, A. (1995). The SOHO mission: an overview. *Solar Physics*, 162:1–37.

Doschek, G., Feldman, U., and Bohlin, J. (1976). Doppler wavelength shifts of transition zone lines measured in Skylab solar spectra. *Astrophysical Journal*, 205:L177–L180.

Feldman, U., Cohen, L., and Doschek, G. (1982). Doppler wavelength shifts of ultraviolet spectral lines in solar active regions. *Astrophysical Journal*, 255:325–328.

Fludra, A., Brekke, P., Harrison, R., Mason, H., Pike, C., Thompson, W., and Young, P. (1997). Active regions observed in extreme ultraviolet light by the Coronal Diagnostic Spectrometer on SOHO. *Solar Physics*, 175,:487–509.

Gabriel, A. (1976). A magnetic model of the solar transition region. *Philosophical Transactions of the Royal Society London, Series A*, 281:339–352.

Gallagher, P., Phillips, K., Harra-Murnion, L., Baudin, F., and Keenan, F. (1999). Transient events in the EUV transition region and chromosphere. *Astronomy and Astrophysics*, 348:251–260.

Habbal, S., Withbroe, G., and Ronan, R. (1985). Spatial and temporal variations of solar coronal loops. *Solar Physics*, 98:323–340.

Hagenaar, H. (2001). Ephemeral regions on a sequence of full-disk Michelson Doppler Imager magnetograms. *Astrophysical Journal*, 555:448–461.

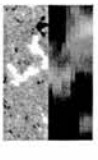

Hansteen, V., Betta, R., and Carlsson, M. (2000). Rapid intensity and velocity variations in solar transition region lines. *Astronomy and Astrophysics*, 360:742–760.

Harra, L., Gallagher, P., and Phillips, K. (2000). Characteristics of quiet Sun cell and network brightenings. *Astronomy and Astrophysics*, 362:371–378.

Harrison, R. (1997). EUV blinkers: The significance of variations in the extreme ultraviolet quiet Sun. *Solar Physics*, 175:467–485.

Harrison, R., Fludra, A., Pike, C., Payne, J., Thompson, W., Poland, A., Breeveld, A., Culhane, J., Kjeldseth-Moe, O., Huber, M., and Aschenbach, A. (1995). The Coronal Diagnostic Spectrometer for the Solar and Heliospheric Observatory. *Solar Physics*, 162:223–290.

Harrison, R., Lang, J., Brooks, D., and Innes, D. (1999). A study of extreme ultraviolet blinker activity. *Astronomy and Astrophysics*, 351:1115–1132.

Harvey, K. (1993). *Magnetic Bipoles on the Sun*. PhD thesis, Utrecht University.

Harvey, K., Jones, H., Schrijver, C., and Penn, M. (1999). Does magnetic flux submerge at flux cancelation sites? *Solar Physics*, 190:35–44.

Innes, D. (2001). Coordinated observations of the quiet Sun transition region using SUMER spectra, TRACE images and MDI magnetograms. *Astronomy and Astrophysics*, 378:1067–1077.

Innes, D., Inhester, B., Axford, W., and Wilhelm, K. (1997). Bi-directional plasma jets produced by magnetic reconnection on the Sun. *Science*, 386:811–813.

Kelly, R. (1987). Atomic and ionic spectrum lines of hydrogen through krypton. *Journal of Physical Chemistry Reference Data*, 16(1).

Kitchin, C. (1995). *Optical Astronomical Spectroscopy*. Institute of Physics.

Krucker, S. and Benz, A. (1998). Energy distribution of heating processes in the quiet solar corona. *Astrophysical Journal*, 501:L213.

Krucker, S., Benz, A., Bastian, T., and Acton, L. (1997). X-ray network flares of the quiet Sun. *Astrophysical Journal*, 488:499–505.

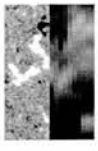

Lites, B. and Hansen, E. (1977). Ultraviolet brightenings in active regions as observed from OSO-8. *Solar Physics*, 55:347–358.

Madjarska, M. and Doyle, J. (2002). Temporal evolution of different temperature plasma during explosive events. *Astronomy and Astrophysics*, 382:319–327.

Mariska, J. and Dowdy, J. (1992). Solar Doppler-shift measurements in the Ne VII 465Å emission line. *Astrophysical Journal*, 401:754–758.

Mariska, J., Feldman, U., and Doschek, G. (1978). Measurements of extreme-ultraviolet emission-line profiles near the solar limb. *Astrophysical Journal*, 226:698–705.

Mason, H., Young, P., Pike, C., Harrison, R., Fludra, A., Bromage, B., and Del Zanna, G. (1997). Application of spectroscopic diagnostics to early observations with the SOHO Coronal Diagnostic Spectrometer. *Solar Physics*, 170:143–161.

Parker, E. (1988). Nanoflares in the solar x-ray corona. *Astrophysical Journal*, 330:474–479.

Parnell, C. (2001). A model of the solar magnetic carpet. *Solar Physics*, 200:23–45.

Parnell, C. and Jupp, P. (2000). Statistical analysis of the energy distribution of nanoflares in the quiet Sun. *Astrophysical Journal*, 529:554–569.

Peter, H. and Judge, P. (1999). On the Doppler shifts of solar ultraviolet emission lines. *Astrophysical Journal*, 522:1148–1166.

Phillips, K. (1992). *Guide to the Sun*. Cambridge University Press.

Porter, J. and Dere, K. (1991). The magnetic network location of explosive events observed in the solar transition region. *Astrophysical Journal*, 370:775–778.

Porter, J., Moore, R., Reichmann, E., Engvold, O., and Harvey, K. (1987). Microflares in the solar magnetic network. *Astrophysical Journal*, 323:380–390.

Porter, J., Toomre, J., and Gebbie, K. (1984). Frequent ultraviolet brightenings observed in a solar active region with Solar Maximum Mission. *Astrophysical Journal*, 283:879–886.

Priest, E. (1982). *Solar Magnetohydrodynamics*. Kluwer Academic Publishers.

Priest, E., Hood, A., and Bewsher, D. (2002). The nature of blinkers and the solar transition region. *Solar Physics*, 205:249–264.

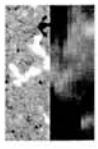

Scherrer, P., Bogart, R., Bush, R., Hoeksema, J., Kosovichev, A., Schou, J., Rosenberg, W., Springer, L., Tarbell, T., Title, A., Wolfson, C., Zayer, I., and MDI Engineering Team. (1995). The Solar Oscillations Investigation - Michelson Doppler Imager. *Solar Physics*, 162:129–188.

Shimizu, T. (1995). Energetics and occurrence rate of active-region transient brightenings and implications for the heating of the active-region corona. *Publication of the Astronomical Society of Japan*, 47:251–263.

Shimizu, T., Tsuneta, S., Acton, L., Lemen, J., and Uchida, Y. (1994). Transient brightenings in active regions observed by the Soft X-ray Telescope on Yohkoh. *Publication of the Astronomical Society of Japan*, 44:L147–L153.

Teriaca, L., Banerjee, D., and Doyle, J. (1999). SUMER observations of Doppler shift in the quiet Sun and in an active region. *Astronomy and Astrophysics*, 349:636–648.

Teriaca, L., Madjarska, M., and Doyle, J. (2001). Electron density variations during ultraviolet transient events. *Solar Physics*, 200:91–114.

Thompson, W. (1998). Deriving statistics from NIS data. Technical Report 49, CDS Software Note.

Walsh, R., Ireland, J., Harrison, R., and Priest, E. (1997). Active region blinkers: Transient events in the solar atmosphere. In Wilson, A., editor, *Fifth SOHO Workshop: The Corona and Solar Wind Near Minimum Activity*, volume ESA SP-404, page 717. European Space Agency.

Wang, H. (1989). On the relationship between magnetic fields and supergranule velocity fields. *Solar Physics*, 117:343–358.

Wilhelm, K. (2000). Solar spicules and macrospicules observed by SUMER. *Astronomy and Astrophysics*, 360:351–362.

Wilhelm, K., Curdt, W., Marsch, E., Schühle, U., Lemaire, P., Gabriel, A., Vial, J., Grewing, M., Huber, M., Jordan, S., Poland, A., Thomas, R., Kühne, M., Timothy, J., Hassler, D., and Siegmund, O. (1995). Solar Ultraviolet Measurements of Emitted Radiation. *Solar Physics*, 162:189–231.

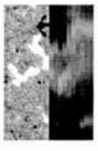

Withbroe, G., Habbal, S., and Ronan, R. (1985). Impulsive phenomena in a small active region. *Solar Physics*, 95:297–310.